

UC Berkeley

UC Berkeley Electronic Theses and Dissertations

Title

Atomistic Insights into Materials Transformations Using Liquid Cell Transmission Electron Microscop

Permalink

<https://escholarship.org/uc/item/5x81h1s7>

Author

Shangguan, Junyi

Publication Date

2022

Peer reviewed|Thesis/dissertation

Atomistic Insights into Materials Transformations Using Liquid Cell Transmission
Electron Microscopy

By

Junyi Shangguan

A dissertation submitted in partial satisfaction of the

requirements for the degree of

Doctor of Philosophy

in

Engineering – Materials Science and Engineering

in the

Graduate Division

of the

University of California, Berkeley

Committee in charge:

Professor Haimei Zheng, Co-Chair

Professor Mark Asta, Co-Chair

Professor Mary C. Scott

Professor Bryan D. McCloskey

Spring 2022

Atomistic Insights into Materials Transformations Using Liquid Cell Transmission
Electron Microscopy

© Copyright 2022
Junyi Shangguan
All rights reserved

Abstract

Atomistic Insights into Materials Transformations Using Liquid Cell Transmission Electron Microscopy

by

Junyi Shangguan

Doctor of Philosophy in Materials Science

University of California, Berkeley

Professor Haimei Zheng and Mark Asta, Co-Chairs

Nanoscale material transformations, including nucleation, growth, dissolution, and phase transitions, correlated with heterogeneity, fluctuations, and structural ordering, are essential to many physical and chemical processes of materials. There has been significant interest in studying nanoscale material transformations in real-time. Understanding and further controlling them allow the opportunity to tailor materials' physical and chemical properties and facilitate the discovery of novel materials. In-situ transmission electron microscopy (TEM) is the most suitable technique for direct observation of material dynamics and nanoscale materials transformations with the necessary spatial and temporal resolution. However, imaging nanoscale materials transformations through liquids with transmission electron microscopy has been a significant challenge due to the fast dynamics and the difficulties in maintaining sufficient resolution while imaging. With our development of ultrathin-thin liquid cells, we are able to reveal materials' growth, dissolution, and phase transition with atomic resolution at various temperatures. My research contains three components centered on the development and applications of different types of liquid cells. Specifically, I apply these methods of development to the following three projects.

(1) Investigating the stacking order and phase transition is significant for the property and application of van der Waals layered nanocrystals. However, direct observation and microscopic understanding are still challenging. Here we have observed a temperature-dependent phase transition in the layered InCl_3 nanocrystal with atomic resolution, which is enabled by our modified in-situ liquid cell TEM techniques applied at varying temperature. Under cryogenic temperature, InCl_3 exhibits multiple stacking orders. Compared to the InCl_3 crystal maintaining the phases during the process at 0°C , the InCl_3 crystal shows a distinct pathway during phase transition at room temperature. Layer-by-layer growth is also observed at the reaction front. This study provides microscopic insights into the transformation process of InCl_3 and thus sheds light on the controllable synthesis and property tuning of layered materials for advanced applications.

(2) As a catalyst for CO₂ reduction and other applications, Cu metal nanostructures have attracted extensive research interest because it is the only metal capable of converting CO₂ into multi carbon-based compounds. Controlling the structure and morphology of copper nanostructures during the preparation process is crucial for enabling the functional design of materials. Here, we have investigated the effect of different temperatures on the morphology of Cu nanoparticles during electrochemical deposition. We find that reducing the temperature can significantly affect the size, nucleation density, and crystallinity of Cu nanoparticles. Electrodeposition at low temperature (-20 °C) produced clusters of small copper nanoparticles, which are distinct from the large highly crystalline copper nanoparticles (~16 nm) obtained from the room temperature process. After analysis, we find that the differences in the morphology and crystallinity of the Cu nanoparticles are caused by changes in the reduction reaction rate and surface diffusion. The limitation of the reaction rate promotes the formation of multi nuclei, and the slow surface diffusion leads to the poor crystallinity of the particles. This work contributes to our understanding of low-temperature electrochemical processes and facilitates the design of catalytic materials with hierarchical structures.

(3) Designing corrosion-resistant materials requires a complementary understanding of corrosion mechanisms at multiple scales. Atomic insights into the corrosion behavior of metals are thus critical. Here, we have studied the pitting corrosion of a Sn nanocrystal with a nanoscale protection layer and the uniform corrosion of Sn metal in real-time using liquid cell TEM. Our observation shows that pitting corrosion starts from defective areas and pitting in different regions merges as the etching area becomes larger. The isotropic etching occurs first, followed by anisotropic etching during the pitting corrosion process. For uniform corrosion, surface diffusion layer and “creeping-like” etching behavior are observed in the thin liquid region. Understanding these corrosion behaviors and dynamics provides important fundamental insight connecting nanocrystal crystalline structure to the development of kinetically stabilized surface features and demonstrates the importance of developing new materials with corrosion resistance.

Dedicated to all my teachers and my family members

Table of contents

Table of contents	ii
List of figures	iv
List of tables	vii
Acknowledgments	viii
1 Introduction to liquid cell transmission electron microscopy	1
1.1 Overview of liquid cell electron microscopy	1
1.2 Investigation of materials transformations using transmission liquid cell electron microscopy	3
2 Liquid Cell Fabrication	10
2.1 Introduction to liquid cell.....	10
2.2 Silicon nitride regular liquid cell	10
2.3 Electrochemical liquid cell	12
2.4 X-ray liquid cell	13
2.5 Carbon film liquid cell	15
2.6 Polymer liquid cell.....	15
3 In-Situ Study of Layered Nanostructure Growth at Various Temperatures	19
3.1 Introduction to layered materials	19
3.2 Experimental setup and the layered structure of the InCl ₃ crystal.....	19
3.3 Lateral translation of layered InCl ₃ in solution at room temperature	29
3.4 The layer-by-layer growth of the vertical InCl ₃ crystal at room temperature.....	31
3.5 Behavior of layered InCl ₃ in solution at low temperature of 0 °C.....	33
4 The effect of temperature on nucleation and growth of copper nanoparticles during electrochemical reactions	35
4.1 Introduction to copper nanoparticles synthesis.....	35
4.2 Experimental setup and structural characterization of the as-prepared Cu nanowires	36
4.3 Structural diversity of copper particles affected by temperature	39
4.4 Growth mechanism of particle growth at various temperatures	42
5 Atomistic insights into pitting and uniform corrosion of Sn nanocrystals	45
5.1 Introduction to pitting and uniform corrosion	45

5.2	Experimental setup and structure characterization of Sn nanocrystals with nanocoating	46
5.3	Investigation of facet selective corrosion process and kinetics of Sn@Ni ₃ Sn ₄ nanocrystals	49
5.4	Atomistic observation of the oxidative pitting corrosion of Sn@Ni ₃ Sn ₄ nanocrystal	51
5.5	High-resolution real-time observation of the oxidative uniform corrosion of Sn nanocrystal	54
5.6	Discussion on the mechanism of pitting and uniform corrosion	58
6	Future Perspectives	60
	References	62

List of figures

Figure 1.1 The development of liquid cells for imaging liquid samples within electron microscopy.....	2
Figure 1.2 Plots of publications and citations of liquid cell in different fields.....	3
Figure 1.3 Possible changes of a nanoparticle during various processes within LCTEM.	4
Figure 1.4 Pathways of nucleation and growth by particle attachment.	4
Figure 1.5 Multistep pathways for the nucleation of Au and Ag nanocrystals in solution.....	5
Figure 1.6 Atomic growth pathways of Pt-based nanoparticles.	6
Figure 1.7 Defect and strain-induced corrosion process of nanocrystals.	7
Figure 1.8 Galvanic replacement etching process.	8
Figure 1.9 Electrochemical deposition of Na and Li.	9
Figure 1.10 In-situ observation of the formation of SEI.....	9
Figure 2.1 Fabrication process flow of SiN _x regular liquid cell.	11
Figure 2.2 Fabrication process flow of SiN _x electrochemical liquid cell.	12
Figure 2.3 Illustration of the fabricated electrochemical liquid cell.	13
Figure 2.4 Design of the x-ray liquid cell.	14
Figure 2.5 Application of the x-ray liquid cell in STXM.	14
Figure 2.6 Illustration of making carbon film liquid cell by sandwiching sample solution between two commercial TEM grids with carbon film.	15
Figure 2.7 Fabrication process flow of fabricating electrochemistry liquid cell with polymer membrane.	16
Figure 2.8 Fabrication and transfer of polyimide membrane.....	16
Figure 2.9 Polyimide membrane transferred onto TEM grid.....	17
Figure 2.10 TEM image and EDS of 40 nm Pt electrode on 10% w/v polyimide membrane.....	18
Figure 3.1 Schematic of setup for low temperature liquid cell experiment.	20
Figure 3.2 Structure model of monoclinic InCl ₃ crystal.	21
Figure 3.3 InCl ₃ crystal structure observation using cryogenic TEM.....	22
Figure 3.4 Illustration of the energetically favored and unfavored structure.....	23

Figure 3.5 Lateral translation of layered InCl_3 in solution at room temperature.	29
Figure 3.6 Reversible phase transition of layered InCl_3 in solution at room temperature.	30
Figure 3.7 The layer-by-layer growth and evolution of the vertical InCl_3 crystal in solution at room temperature.	32
Figure 3.8 Sequential TEM images showing the amorphous to crystal transition during growth process.	32
Figure 3.9 Behavior of layered InCl_3 in solution at the low temperature of $0\text{ }^\circ\text{C}$	33
Figure 3.10 Sequential TEM images showing the removal of dislocation in InCl_3 crystal with dislocation climbing and gliding.....	34
Figure 4.1 Illustration of experimental setup and characterization of 1.0 M LiPF_6 in $\text{EC/DEC} = 50/50$ (v/v) electrolyte at room temperature ($20\text{ }^\circ\text{C}$) and sub-zero temperature ($-20\text{ }^\circ\text{C}$), respectively.	36
Figure 4.2 TEM characterization for the structure of the as-prepared Cu nanowires.....	37
Figure 4.3 Low magnification TEM image of the Cu nanowires showing the diameter to be about 30 nm	38
Figure 4.4 TEM and FFT pattern of the as-prepared Cu nanowire.....	38
Figure 4.5 Structure characterization of the hierarchical Cu nanoparticle/nanowire nanostructure formed at room temperature ($20\text{ }^\circ\text{C}$).....	39
Figure 4.6 Low-resolution TEM image of the hierarchical Cu nanoparticle-nanowire nanostructure.	40
Figure 4.7 EDS spectrum of Cu nanostructures formed at room temperature ($20\text{ }^\circ\text{C}$) with large crystalline Cu nanoparticles attached to the Cu nanowires.	40
Figure 4.8 Structure characterization of the hierarchical Cu nanocluster/nanowire nanostructure formed at $-20\text{ }^\circ\text{C}$	41
Figure 4.9 Nuclei size and nucleation density of Cu nanoparticles formed at $20\text{ }^\circ\text{C}$ and $-$ $20\text{ }^\circ\text{C}$, respectively.	42
Figure 4.10 TEM image and FFT pattern of the Cu nanoclusters formed at $-20\text{ }^\circ\text{C}$	42
Figure 4.11 Schematic illustrations of two kinds of electrochemical growth mechanisms of Cu metal.....	44
Figure 5.1 Chemical and structural characterization of $\text{Sn@Ni}_3\text{Sn}_4$ nanocrystal before and after corrosion in aqueous solution using a cryo-holder.	46
Figure 5.2 Surface classification based on contact angles.	47

Figure 5.3 Schematic representation of the setup for the liquid cell experiment.....	47
Figure 5.4 Morphology and composition characterization of Sn nanocrystals with nanocoating before and after corrosion.....	48
Figure 5.5 Electron tomography of Sn nanocrystals.....	49
Figure 5.6 Real-time observation of the etching process of Sn@Ni ₃ Sn ₄ nanocrystal in aqueous solution.....	50
Figure 5.7 Facet determination according to the etched morphology.....	51
Figure 5.8 High-resolution real-time observation of the oxidative pitting corrosion process of Sn@Ni ₃ Sn ₄ nanocrystal in aqueous solution.....	52
Figure 5.9 Original TEM image sequence showing pitting oxidative etching process of Sn@Ni ₃ Sn ₄ nanocrystal in solution.	53
Figure 5.10 Sequential TEM images showing no corrosion reaction occurs where the protective layer is intact.	53
Figure 5.11 Sequential TEM images showing a galvanic corrosion process of Sn@Ni ₃ Sn ₄ nanocrystal in aqueous solution.	54
Figure 5.12 Structure characterization of Cu nanocrystals.	55
Figure 5.13 Structure characterization of Sn nanocrystal within liquid cell by cryo-EM.	56
Figure 5.14 Structure characterization of Sn nanocrystal synthesized ex-situ.	57
Figure 5.15 High-resolution real-time observation of the oxidative etching process of Sn nanocrystal in solution.	58
Figure 6.1 Design of novel electrochemical liquid cell setup allowing to study electrochemical processes with liquid electrolyte in-situ at various temperatures. ..	60

List of tables

Table 3.1 Possible structural models of bilayer InCl_3 with lateral translation.	24
Table 3.2 Possible structural models of triple layer InCl_3 with lateral translation.	26
Table 3.3 Summary for possible structural model of mono-, bi-, triple-layers InCl_3 with lateral translation.	28

Acknowledgments

Time flies quickly. It feels like only a few months ago that I arrived in Berkeley and started my study for a Ph.D. in 2017. As I look back, scenes of the past years are still vivid in my mind. I am filled with appreciation and gratitude for the people and things that made my experience in Berkeley so remarkable and magnificent.

First and foremost, I want to thank my primary supervisor Professor Haimei Zheng, who provided me with a priceless opportunity and unwavering support during my Ph.D. period. It was your invaluable guidance and mentoring that let me go through the confusion to where I am now. Thank you for inspiring me to be my best and for being there to guide me at every stage of the research project. You did more than preparing me academically; and you also prepared me for life. Thank you for all the insightful comments and suggestions you have given me.

Similar gratitude belongs to all the members and staff scientists in National Center for Electron Microscopy and Molecular Foundry that I have had the honor to work with. Karen Bustillo, Chengyu Song, Rohan Dhall, Stefano Cabrini, Michael Elowson, Selven Virasawmy, Scott Dhuey, Arian Gashi taught me the skills and techniques in the lab. You ensured the lab ran safely and smoothly and all supplies were accessible, making it possible for me to conduct experiments and work on my projects. And thank you for your additional support through technical and scientific discussion.

All members in Haimei group were not only amazing coworkers but also incredible mentors and lovely friends. I feel so blessed to be working with you. Sophia Betzler, Zhanxi Fan, Jiwoong Yang, Lei Yu, Seungyong Lee, Yu Wang, Yujun Xie, Xinxing Peng, Qiubo Zhang, Zuwei Yin, Haobo Yu, Tai-Feng Huang, Sang Hoon Joo, Wenjing Zheng, Jiawei Sun, Chi Zhang, Wen Wang, Qi Zheng, Daewon Lee, Jiawei Wan, Haochen Li, Matthew Hauwiller, you were an invaluable part of the group. With all of you, the laboratory equipment was maintained so well and all chemicals were placed in order. And thank you for pushing me professionally and for your wonderful patience, continuous support and great mentorship through scientific discussion and collaborations. Xubo Liu, Xiangming Li, Honghao Hou, Yunhui Tang and Qin Hu also added additional warm humor and made the lab a fun place to work. I honestly couldn't ask for better labmates.

Finally, I want to thank my family for their immense kindness, thorough understanding, and loving guidance in all past years. Without you, my father, mother and sister, I wouldn't have made it this far.

What's past is prologue. I will keep moving forward, opening new doors and doing new things, with gratitude to everyone I have met along the way.

1 Introduction to liquid cell transmission electron microscopy

1.1 Overview of liquid cell electron microscopy

Transmission electron microscopy (TEM) is one of the most powerful tools for studying the microscopic structure of materials with high spatial resolution.¹⁻³ It can help researchers obtain information on the local structure and chemical composition of materials down to the atomic level to reveal the relationship between performance and structure.⁴⁻⁶ After decades of the development of TEM techniques and electromagnetic optics, the spatial resolution has been advanced from the initial 50 nm to the sub-50-pm level because of the development of aberration-corrector optics in the imaging system.⁷⁻¹⁰ By combining with the new design of electron microscopy pixel array detector, a 0.39 Å Abbe resolution was achieved in 2018.¹¹ The latest pixel array detector has made it possible to image thicker samples with <0.20 Å Abbe resolution.¹²

Compared with the accomplishments achieved in high-resolution imaging of solid samples, in-situ observations of liquid samples still face many challenges.¹³⁻¹⁶ One of the main issues is that the electron beam works under a high vacuum environment,¹⁷ which requires the observed samples to be free of water and other volatile solvents. However, many materials are synthesized in liquids or function in a liquid medium. Their structure may change during the sample preparation that involves drying the sample for TEM imaging. Thus, the structures observed in the electron microscope may drastically be different from their original structure in solution. On the other hand, although optical microscopy is used to image liquid samples, the resolution is insufficient to obtain detailed information on the fine structure of materials. Therefore, it is significant to develop high-resolution liquid cell transmission electron microscopy (LCTEM) techniques to resolve materials pristine structures in liquids and their dynamic processes in solution in-situ and in-operando.¹⁸

Since the invention of the electron microscope, direct observation of liquid samples has been explored by many researchers. Here are some milestones in LCTEM development, as shown in Figure 1.1. As early as in the 1930s and 1940s, the earliest liquid cell for electron microscopy was achieved using Pt as the supporting frame and nitrocellulose film from cotton as membrane and a sandwich structure was made with solvent inside.^{19, 20} In recent years, with the development of nanofabrication, microfluidic technology, and electron microscopy technique, the LCTEM technology using silicon nitride (SiN_x) as membrane windows has made great progress.^{21, 22} In 2003, F. M. Ross et al. revealed the early-stage growth of Cu clusters through electroreception using a SiN_x electrochemical liquid cell, which pushes the spatial resolution to 5 nm.²¹ In 2009, H. Zheng et al. introduced ultrathin SiN_x liquid cells to study the growth of Pt nanoparticles with sub-nanometer resolution.²² More importantly, a thin Si wafer of only 100-micrometer in thickness instead of standard wafer of 500-micrometer was used for these thin liquid cells, which allows chemical analysis in-situ using energy-dispersive X-ray spectroscopy (EDS). It was the first time the direct high-resolution imaging and chemical analysis through liquids were achieved. With the thin liquid cell TEM setup, two different growth modes of Pt nanocrystals are found,

namely monomer-by-monomer attachment and coalescence. In the same year, N. de Jonge et al. developed the setup of the microfluidic flow cell, pushing the spatial resolution to 4 nm.²³ In 2010, an open-cell setup with ionic liquid electrolyte was designed to study battery materials.²⁴ The lithiation of the SnO₂ nanowire during electrochemical charging was observed in real-time. The open-cell design is limited to special liquid samples with low vapor pressure and low volatility. In 2012, graphene was used to encapsulate solution and atomic resolution was achieved.²⁵ In the same year, the atomic resolution imaging was also achieved using liquid cells with SiN_x membranes.²⁶ Following these works, more and more liquid systems have been investigated with liquid TEM. Also, with the development of nanofabrication technology, various designs of liquid cells have been reported.

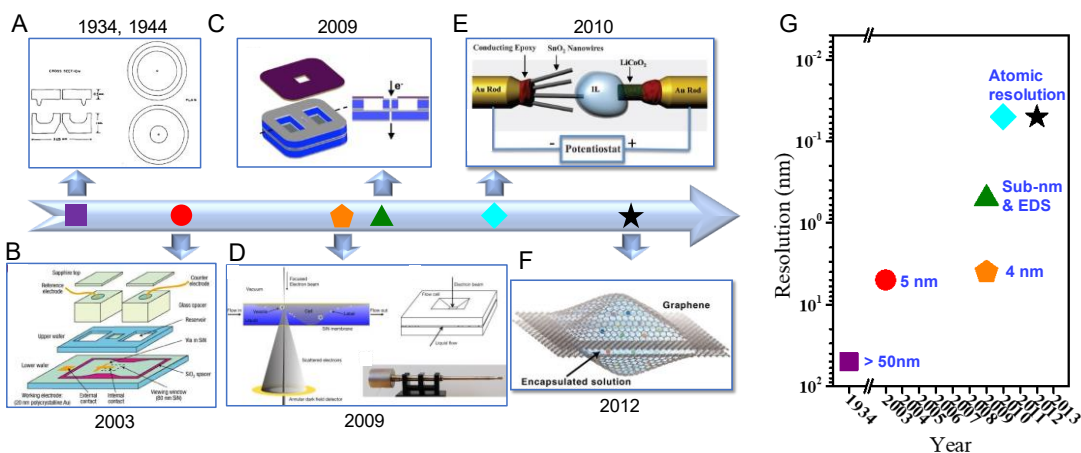


Figure 1.1 The development of liquid cells for imaging liquid samples within electron microscopy. Schematic of (A) the liquid cell with sandwich structure,^{19, 20} (B) SiN_x electrochemical liquid cell,²¹ (C) ultrathin regular liquid cell,²² (D) flow cell,²³ (E) open cell using an ionic liquid,²⁴ and (F) graphene liquid cell.²⁵ (G) Spatial resolution versus year achieved by the corresponding liquid cells in LCTEM.

The advantages of in-situ LCTEM are highlighted as follows. It allows for directly observing the changes of various materials in liquids during reactions in real-time, including growth, dissolution, self-assembly, and phase transition, with high resolution down to the atomic level.^{21, 22, 25-35} Using in-situ LCTEM, previously unknown details of the reaction can be discovered in real-time, and the understanding of the reaction can reach an unprecedented level, which can greatly promote basic research and applications. The key technology of LCTEM is to design and prepare an in-situ liquid cell. Since liquid cells can confine liquid specimens for in-situ TEM observations, some rules and disciplines must be followed in the design of liquid cell and the fabrication process. First, the liquid cell setup should be compatible with TEM. This requires the support film to be an ultra-thin membrane with low atomic number elements to decrease electron scattering and increase sample contrast. Second, the liquid cell material must be physically and chemically stable so that it would not interact with the samples loaded inside. Based on the above requirements, currently available sample chamber observation windows include SiN_x, carbon film, graphene, and MoS₂.^{22, 36-39}

LCTEM has become a cutting-edge scientific research technique after several years of development, and it has been widely used throughout the research fields of materials science, physics, chemistry, and biology.^{27, 30, 40-42} Researchers have been developing this technique to observe changes in material structure at the atomic scale in real-time.^{25, 27, 42-45} The LCTEM technique allows to investigate the chemical reaction process in the solution,⁴⁶ which is of great significance for studying the reaction mechanism and controlling the reaction process. The worldwide application of the in-situ LCTEM and related liquid chip techniques have made breakthrough achievements, and it is attracting more and more attention.¹⁴ Figure 1.2 shows the fast growth of the field of study. In 2020, a Gordon Research Conference (GRC) with focused topic on Liquid Phase Electron Microscopy was established. The future growth of the LCTEM techniques and extensive scientific discoveries using this technique are expected.

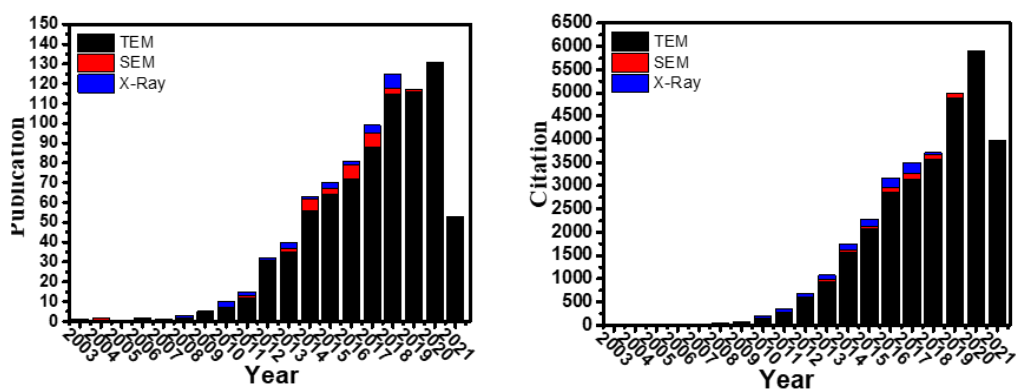


Figure 1.2 Plots of publications and citations of liquid cell in different fields. (A) Plots of the number of publications and (B) citations from 2003 to July 2021.

1.2 Investigation of materials transformations using transmission liquid cell electron microscopy

LCTEM has been extensively used for in-situ studies of nanoparticle dynamical phenomena, including nucleation, growth, dissolution, and self-assembly.^{21, 22, 30, 35, 47-49} With the technical advances of LCTEM, in-situ investigation of nanocrystal formation and transformations using LCTEM has become a hot topic of study. Various fascinating discoveries have been made on imaging the changes of a nanocrystal during nucleation, growth and dissolution (Figure 1.3). Today, with the advances of LCTEM techniques, this topic continues to attract a lot of attention. A set of works reported in this thesis are centered on in-situ study of nanoscale materials transformations by developing and applying advanced LCTEM.

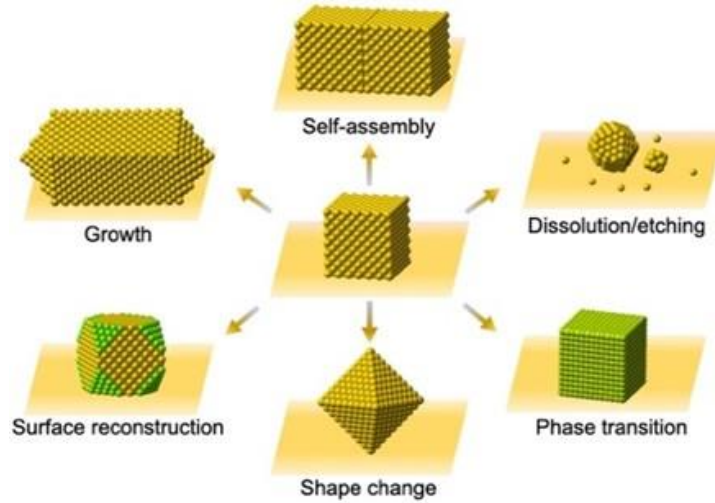


Figure 1.3 Possible changes of a nanoparticle during various processes within LCTEM.

Nucleation and growth in solution-phase syntheses have been described by the classical theory of competing surface energy and volume energy in colloidal chemistry.⁵⁰⁻⁵³ However, there have been reports on nonclassical multistep crystallization, which involves various prenucleation intermediate species,^{26-28, 54} as shown in Figure 1.4.⁵⁵

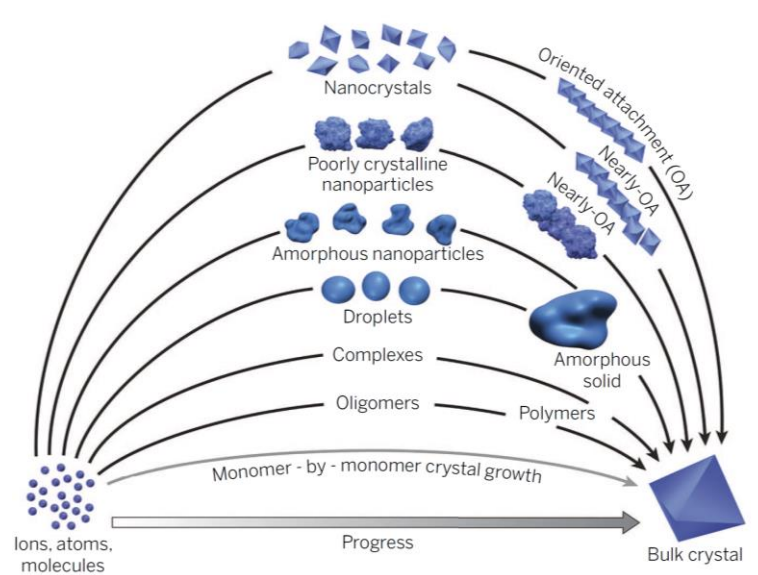


Figure 1.4 Pathways of nucleation and growth by particle attachment. The crystallization through particle attachment is considered as non-classical growth pathway.⁵⁵

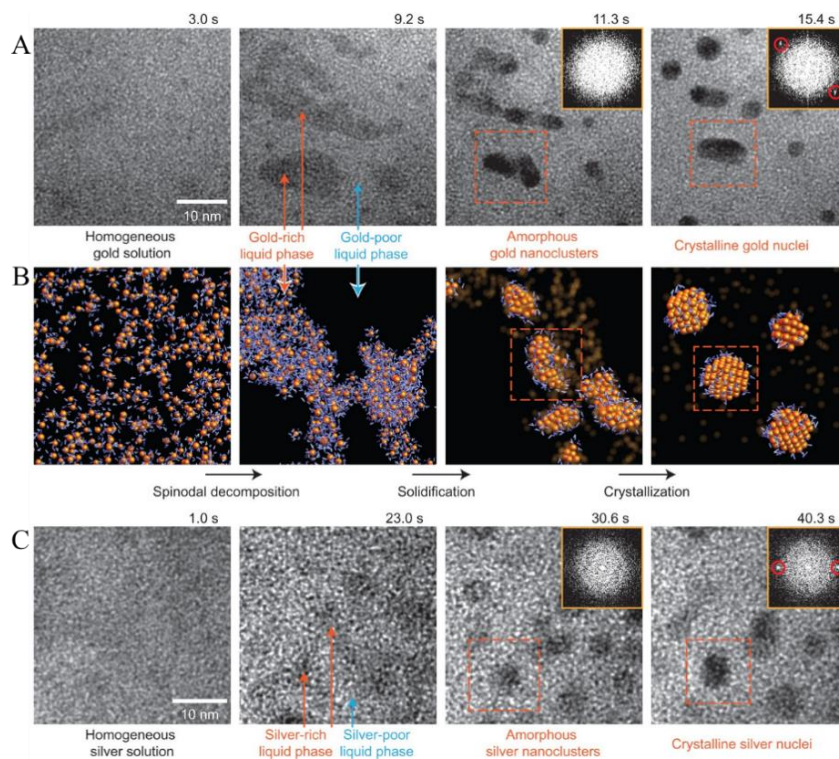


Figure 1.5 Multistep pathways for the nucleation of Au and Ag nanocrystals in solution. (A) Sequential TEM images show the three-step nucleation pathway of Au nanocrystals. (B) The atomic model illustrates the nucleation pathway. (C) The nucleation pathway of Ag nanocrystals is similar to the nucleation pathway of Au nanocrystals in (A).⁵⁴

Nucleation of solids from a liquid solution is often correlated with local fluctuations in the concentration and short-range structural ordering or formation of prenucleation clusters. The prenucleation intermediates are metastable, and they often exist only transiently before growing into stable nanocrystals. There have been some studies on the early stage of growth.^{45, 54, 56} Nonclassical multistep crystallization of nanocrystals from nanocluster intermediates was investigated using LCTEM. A multistep growth of Au and Ag nanocrystals was revealed using LCTEM. A metal-rich phase intermediate was found at the early-stage growth of Ag and Au nanocrystals (Figure 1.5).⁵⁴

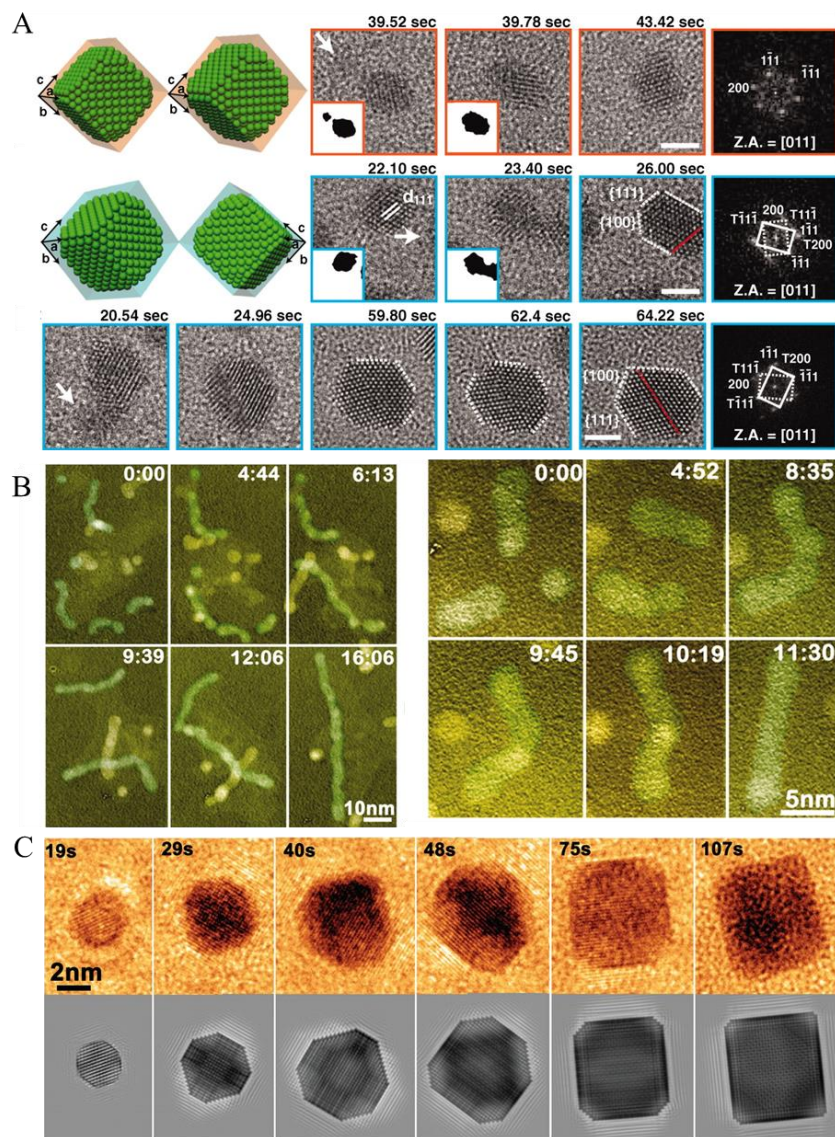


Figure 1.6 Atomic growth pathways of Pt-based nanoparticles. In-situ observation of the growth of (A) Pt nanoparticles,²⁵ (B) Pt₃Fe nanorods²⁶ and (C) Pt nanocubes.⁴²

The growth of nanoparticles has been well studied and it can be considered as the most representative topic of research using LCTEM. The precursor solution is used as the starting material for in-situ observations of nanocrystal growth. Pt nanocrystal growth via coalescence and crystal-structure evolution was observed with atomic resolution using graphene liquid cell (Figure 1.6A).²⁵ Pt₃Fe nanorod growth from nanoparticle building blocks was revealed using ultrathin SiN_x liquid cell (Figure 1.6B).²⁶ Moreover, the atomic pathway of the facet development during the Pt nanocube growth was also observed (Figure 1.6C).⁴² Besides Pt particles, the growth of nanocrystals, including metallic nanocrystals, metal-oxide and metal-organic frameworks, has been reported.^{33, 54, 57, 58}

Besides revealing the nucleation and growth processes, LCTEM also plays an important role in the study of dissolution/etching/corrosion.^{59, 60} Structure evolution, including

specific shape and morphology changes occurring locally on individual nanocrystals, is revealed using in-situ techniques.⁶¹⁻⁶⁴ LCTEM provides capabilities for the direct observation of dissolution/etching/corrosion behaviors in liquid environment. A variety of dynamic dissolution/etching/corrosion phenomena have been visualized with high-spatial-resolution using LCTEM. For example, the in-situ study of defect-induced asymmetrical corrosion behavior and strain-induced corrosion process was reported at the nanoscale using LCTEM.^{61, 65} Corners were the preferential corrosion site (Figure 1.7A). The corrosion process was much faster in regions with tensile strain and high local curvature (Figure 1.7B).

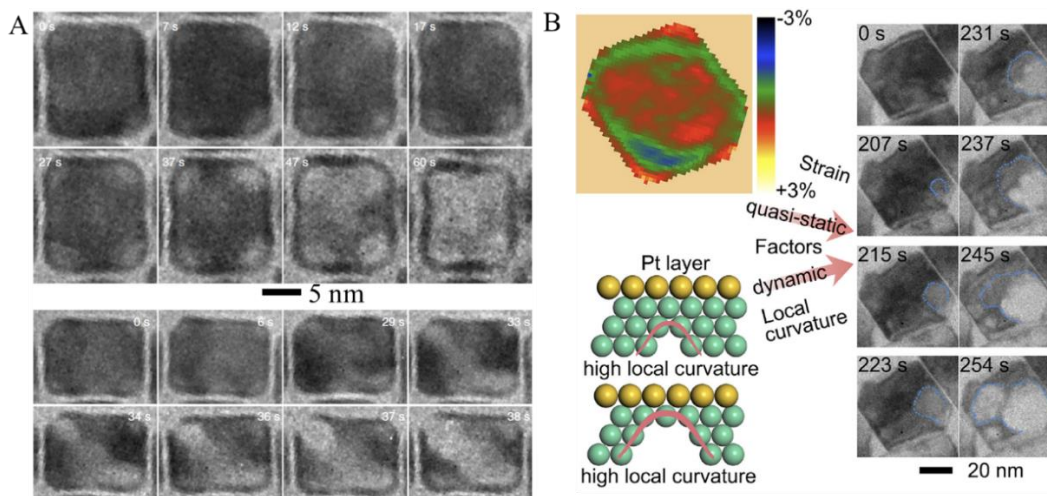


Figure 1.7 Defect and strain-induced corrosion process of nanocrystals. (A) Asymmetrical corrosion of corner defected Pd@Pt core-shell nanocubes. (B) Pd@Pt octahedron corrosion process starting from a terrace defect.

In-situ observations by LCTEM can provide insight into mechanisms, rates, and possible modifications of dissolution/etching/corrosion reactions in the solution environment. Nanoscale Kirkendall effect was observed during the galvanic replacement reaction between Ag nanoparticles and HAuCl_4 (Figure 1.8A) and PdCl_2 (Figure 1.8B) solution.^{65, 66} These results enhance our understanding of these dissolution/etching/corrosion behaviors and dynamics, which helps to provide crucial fundamental insight connecting nanocrystal crystalline structure to the development of kinetically stabilized surface features and demonstrates the importance of developing new materials with corrosion resistance.

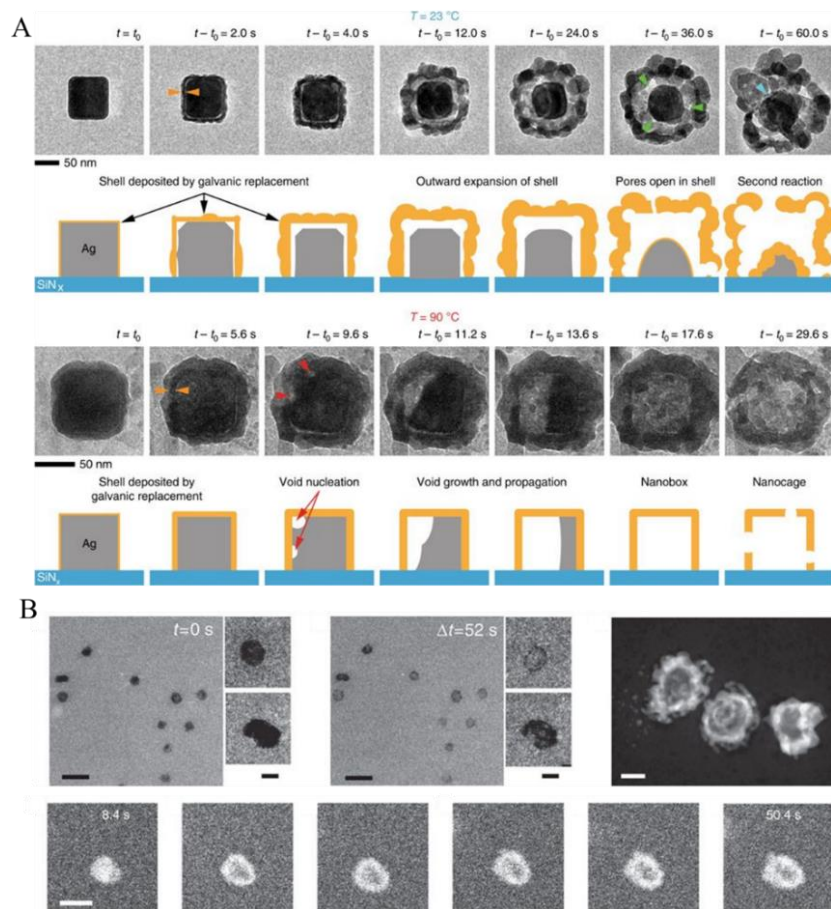


Figure 1.8 Galvanic replacement etching process. (A) Evolution of Ag nanocubes in HAuCl₄ solution at different temperatures.⁶⁵ (B) Change of Ag particles in aqueous PdCl₂ solution.⁶⁶

With the development of electrochemical liquid cells, it has been possible to image through liquid electrolytes and observe the deposition and dissolution of an alkali metal (e.g., Li^{67, 68} and Na⁶⁹) and other metals.^{21, 70, 71} Electrochemical liquid cells with the electrodes being patterned in certain configurations were developed (Figure 1.9A, C).^{29, 69} Such electrochemical liquid cells have been used for in-situ study of alkali metal electrochemical deposition with a focus on the impact of the electrode morphology on the initial deposition. In-situ LCTEM study of the initial precipitation sites and local ion distribution near the electrode provides invaluable information.⁷² The Na deposition showed granular growth mode (Figure 1.9B). The newly formed Na grains preferentially deposited at the base of existing grains close to the electrode.⁶⁹ The electrochemical deposition of Li was also investigated using LCTEM. The charge and discharge process of the Li-battery showed that the nanoscale "dead Li" detached from the working electrode after cycling, thereby confirming the irreversible transformation between Li metal and Li-ions (active material loss).⁶⁷

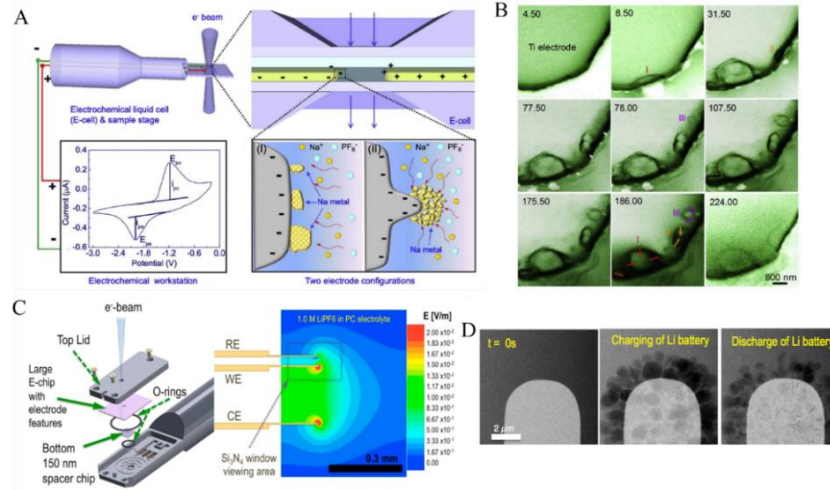


Figure 1.9 Electrochemical deposition of Na and Li. (A) A schematic of the in-situ TEM setup for electrochemical deposition. (B) In-situ imaging of the electrochemical deposition of Na. (C) An electrochemical TEM sample holder for metal deposition. (D) In-situ observation of the electrochemical deposition of Li.

Besides the morphology evolution of metal deposition, real-time observation reveals unprecedented detail of the solid electrolyte interphase (SEI) effects on electrochemical deposition. Different compositions of SEI are determined (e.g., LiF) using electron diffraction and EDS.^{68, 73-75} Variations in the SEI thickness on a Na nanograin introduce differences in the local growth rate and morphology disparities among the nanograins. Additionally, the formation of the SEI and structural modifications of cathode materials during charge cycles have also been captured successfully. Additives can drastically change the charge distribution on electrodes by selectively passivating certain features of the electrode.⁷⁵ These studies open future opportunities to address many more important questions in electrochemical deposition/dissolution of alkali metal and the roles of SEI.

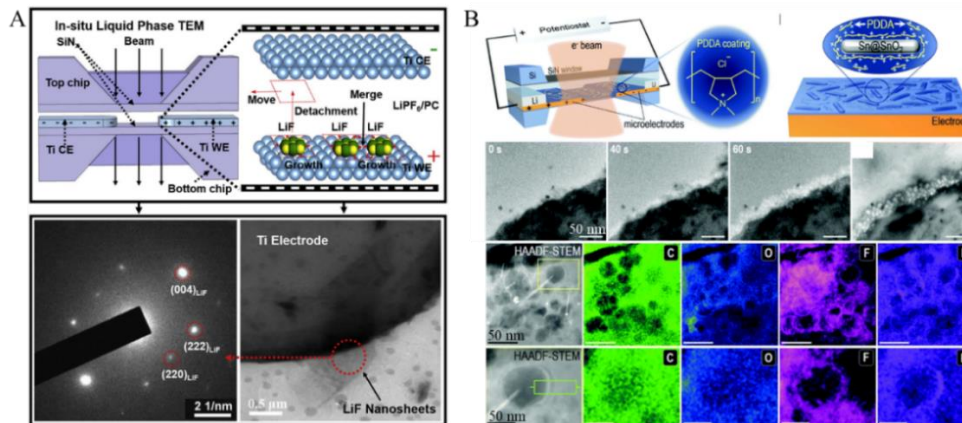


Figure 1.10 In-situ observation of the formation of SEI. (A) Experimental setup for the in-situ LCTEM study of LiF formation within the SEI. (B) In-situ imaging of Li growth and the characterization of the SEI on Li.

2 Liquid Cell Fabrication

2.1 Introduction to liquid cell

TEM has been a strong technique to study nanomaterials' behavior and dynamics due to its ability to directly observe nanocrystals down to the atomic scale and characterize the structural and elemental distribution. With the development of nanofabrication techniques, SiN_x based liquid cells are fabricated and introduced to in-situ LCTEM studies, making it possible to observe solution-based processes directly. Visualizing nanomaterials behaviors in liquid phase at the nanoscale and in real-time could offer opportunities to verify existing theories and to understand fundamental processes in materials science, lithium-ion batteries, life science and other research fields.

Liquid cell can sandwich a thin layer of liquid between two ultrathin membranes so that the liquid specimen is isolated from the ultra-high vacuum environment and can be maintained inside the liquid cell. The advancement in liquid cell fabrication fostered scientific breakthroughs and achievements. Besides SiN_x liquid cell allowing for sub-nanometer resolution,^{22, 26} electrodes are added to realize electrochemical investigations.²¹ Then microfluidic flow cell was introduced to allow liquid flow during reactions in TEM.²³ With a deeper understanding of two-dimensional materials, graphene of only several layers was used to encapsulate the solution and reached atomic-level resolution in TEM.²⁵ Later, the hybrid liquid cell architectures with graphene-sealed SiN_x cavities were fabricated to confine sample nanomaterials and solutions in defined dimensions while reaping the benefit of using graphene as viewing window material.^{76, 77} MoS₂ liquid cells with a layer of graphene and a layer of MoS₂ as the encapsulating membrane as well as the functional substrate was also achieved.³⁷ Recently, carbon film liquid cell was introduced by simply using commercial TEM ultrathin carbon film grids.³⁹

Liquid cell prepared by nanofabrication encapsulates liquids in nano-reactors to form a thin layer of liquid (~10-300 nm). The liquid cell needs to meet several requirements: (1) The electron microscope is operated under a high vacuum, and the liquid sample cell is required to have good sealing, and strong mechanical properties. (2) The observation window of the liquid sample chamber should be thin and chemically stable; (3) Non-conductive membrane is essential for the electrochemical liquid cell to prevent short circuit.

2.2 Silicon nitride regular liquid cell

Regular liquid cell with SiN_x supporting film is powerful for in-situ LCTEM studies. The fabrication process flow is in Figure 2.1. The traditional SiN_x liquid cell bottom is fabricated from a commercial 4-inch p-doped silicon wafer of 100 μm thick. Initially, the ultra-thin starting silicon wafer is coated with 15 nm low-stress SiN_x through low pressure chemical vapor deposition (LPCVD). The sample wafer is then cleaned with acetone and isopropyl alcohol (IPA) and baked at 180 °C for 10 minutes to remove the moisture and organic solvent residue.

For the photolithography process, a dummy wafer with standard thickness of 500 μm is spin-coated with photoresist and immediately bonded with the ultra-thin sample wafer by the photoresist before baking at 100 °C for 2 minutes. Without the dummy wafer, the ultra-

thin sample wafer is fragile and tends to break during spin coating process. Then about 7 drops of hexamethyldisilazane (HMDS) are dripped and spin-coated onto the sample wafer to increase surface uniformity and to increase its adhesion of photoresist. It will be baked at 100 °C for 2 minutes to solidify the HMDS. This is followed by the spin coating of MAP-1215 photoresist and baking at 100 °C for 2 minutes. After being exposed to ultraviolet (UV) light under a mask, MAD-331 solution is used to develop the photoresist and remove the photoresist in UV light-exposed area. In this way, the photoresist is patterned, and some SiN_x is uncovered. Then the isotropic Reactive Ion Etching (RIE) is used to etch the exposed SiN_x using the mixture gas of oxygen and CHF_3 , exposing the silicon in the patterned area. The wafer is immersed in acetone for two days to remove all photoresist and the ultra-thin sample wafer would detach from the handling dummy wafer.

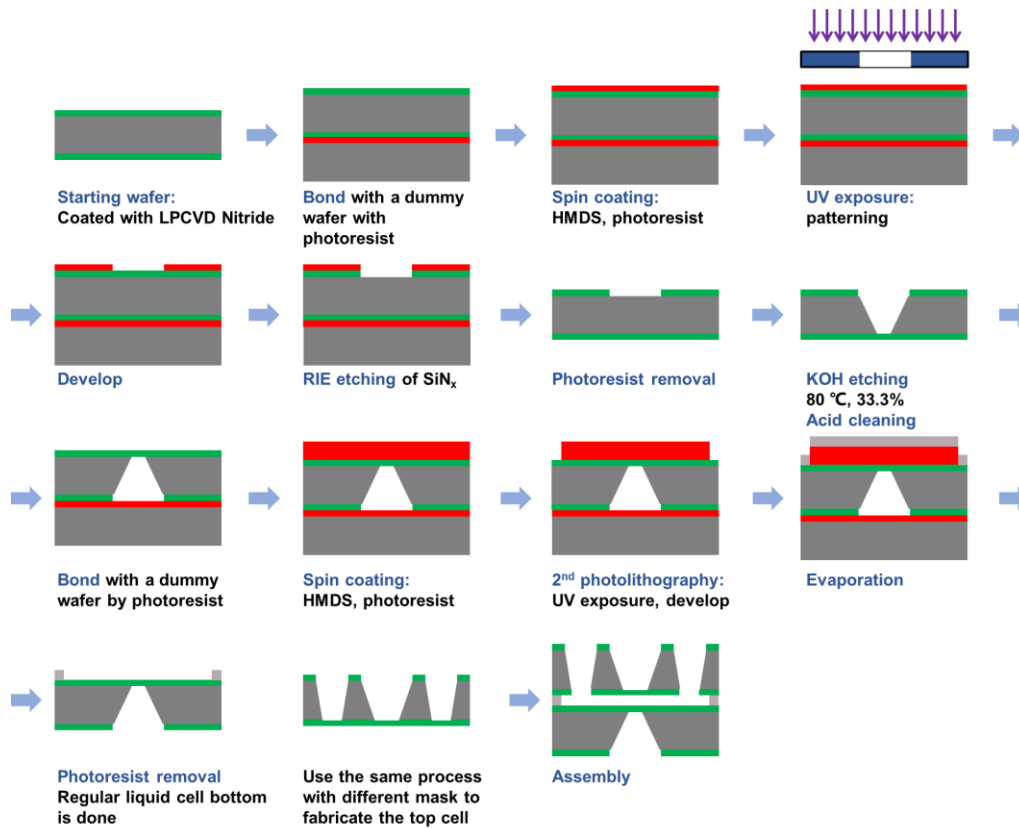


Figure 2.1 Fabrication process flow of SiN_x regular liquid cell.

Then the exposed silicon is etched by 33.3% potassium hydroxide (KOH) in water solution at 80 °C. The low stress SiN_x membrane is chemically stable in KOH solution. The KOH etching rate for the silicon (111) plane is much slower than other crystalline orientations,⁷⁸ so the KOH etching process will leave a cavity of silicon surrounded by the {111} facets of Si while the SiN_x membrane is suspended below. The sidewalls of the cavity form an angle of 54.7° with the wafer surface, which guides the design of liquid cell mask. After this, the piranha solution is used to clean the wafer.

The wafer is flipped and bonded with another clean dummy wafer for the second photolithography. Following a similar process of spin coating, UV exposure and

development, the wafer is evaporated with a thin layer of 150 nm indium by thermal evaporation and then lift-off. The indium plays the role of spacer and sealing material of liquid cell. After cleaning, the bottom chip of the regular SiN_x liquid cell has been finished.

Using different masks, similar process can be used to fabricate the top chip of regular SiN_x liquid cells. The top chip and bottom chip can be carefully aligned and bonded by indium spacer after baking at 120 °C for one hour. Alternatively, Gel-Pak and UV glue can also be used to align and bond regular liquid cell, respectively.

2.3 Electrochemical liquid cell

To conduct in-situ electrochemistry studies with LCTEM, the electrochemical liquid cell is designed and fabricated with the ability of biasing. The fabrication process of electrochemical liquid cell is similar to that of SiN_x regular liquid cell with some changes, as shown in Figure 2.2.

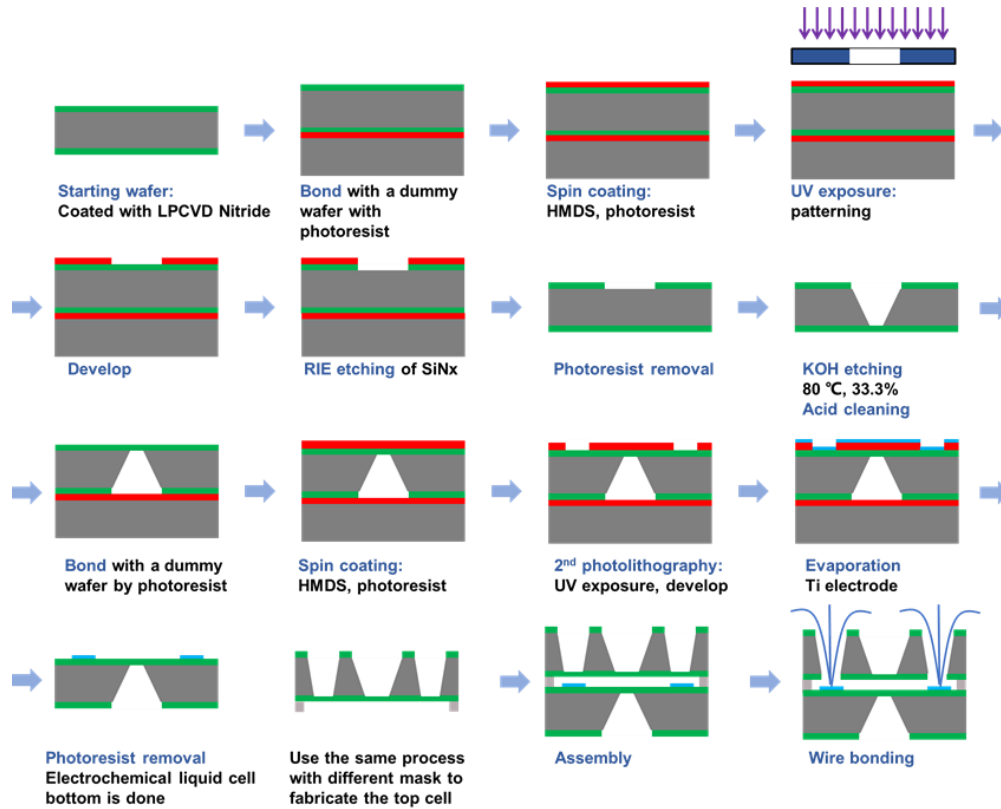


Figure 2.2 Fabrication process flow of SiN_x electrochemical liquid cell.

First, the silicon wafer used for the electrochemical liquid cell is 200 nm thick and coated with 30 nm SiN_x so that it is strong enough to withstand the fabrication process operations. Second, 90 nm titanium electrode is evaporated on the bottom chip in the second photolithography process. Then after cell assembly, these electrodes are bonded with aluminum wires (Figure 2.3). In this way, the liquid cell can be connected to an electrochemistry working station through the build-in conductive wires inside the electrochemistry TEM holder, so the current or voltage can be applied to the sample. Third, the indium spacer is patterned on the top chip rather than the bottom chip in order to

simplify the fabrication process of bottom chip and to keep the cleanness of bottom chip.

After assembling the top chip and bottom chip, epoxy is used to seal the surroundings to prevent sample solution leakage and tighten the bonding of the top and bottom chips (Figure 2.3A). As shown in Figure 2.3B, the SiN_x membrane of the top chip reservoir can be broken by a clean tweezer tip and then aluminum wires are bonded to the electrode through the reservoir. After loading the sample solution from the reservoir, epoxy is used to carefully seal the reservoir area. UV glue can also be used to replace the epoxy since it can be solidified within seconds under UV exposure, and it is chemically stable when touching the electrolyte.

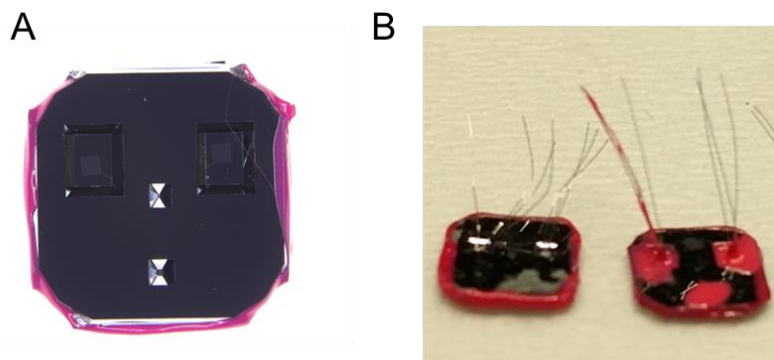


Figure 2.3 Illustration of the fabricated electrochemical liquid cell. (A) Electrochemical liquid cell after assembling the top chip and the bottom chip. Epoxy is used to seal the surroundings to reduce solution leakage. (B) The left electrochemical liquid cell has been bonded with conductive wire. The right electrochemical liquid cell has been loaded with sample solution through the reservoirs by a pipette and the reservoirs have been sealed by the epoxy.

2.4 X-ray liquid cell

The electrochemical liquid cell makes it possible to conduct electrochemistry studies by in-situ LCTEM, inspiring the investigations to be extended to x-ray sources. Though the spatial resolution is lower than TEM, x-ray probes can offer information different from TEM.

A new x-ray liquid cell is designed as in Figure 2.4A. The aspect ratio of the viewing window is large, so it is less likely to break. There are two windows ($30 \times 600 \mu\text{m}$) in parallel so there would be more space for observation. The masks for individual bottom chip and top chip are in Figure 2.4B and C. The fabrication process flow would be the same as the electrochemical liquid cell. Figure 2.4E is the scanning electron microscopy (SEM) image of electrodes on the window, as highlighted by the purple dashed box in Figure 2.4B. The protuberance is designed on the electrode to help differentiate cathode and anode during the experiment.

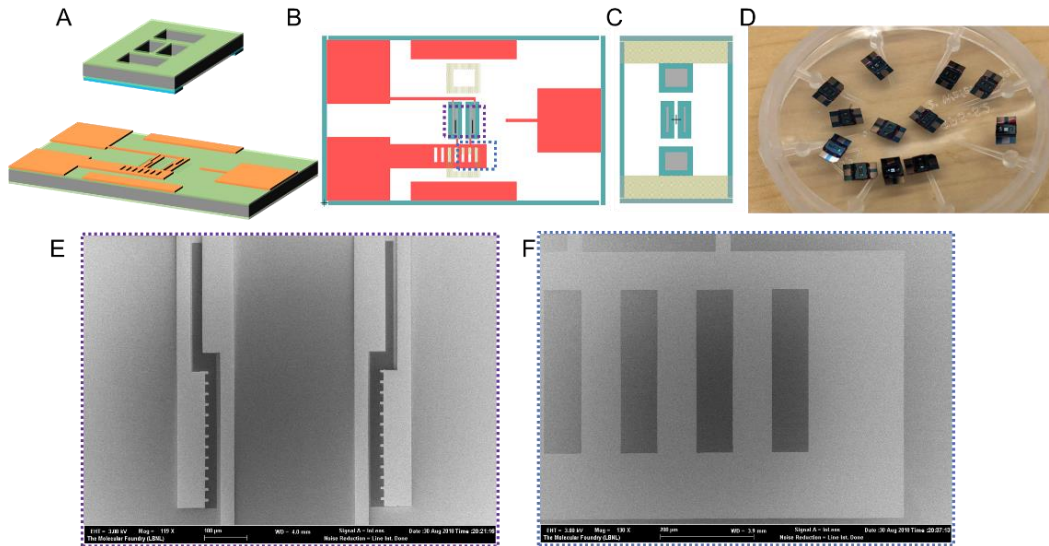


Figure 2.4 Design of the x-ray liquid cell. (A) 3D model of the new x-ray liquid cell. (B) Design of the bottom chip mask. (C) Design of the top chip mask. (D) Fabricated x-ray liquid cell. (E) SEM images of the electrodes above the viewing windows of liquid cell, corresponding to the purple dashed square region in (B). (F) SEM images of the electrodes with holes below viewing windows, corresponding to the blue dashed square region in (B).

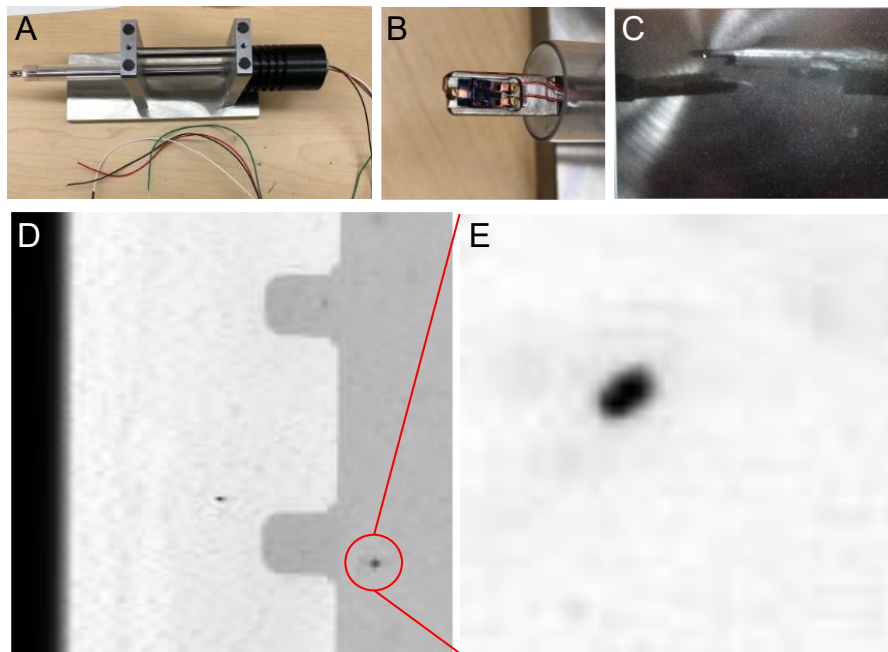


Figure 2.5 Application of the x-ray liquid cell in STXM. (A) A home-made TEM holder with biasing capability. This holder is compatible with STXM chamber. (B) Tip of the holder loaded with an x-ray liquid cell. (C) The holder is inserted into the STXM chamber. (D) STXM image of the lithium-rich material loaded into the x-ray cell. (E) Magnification of the particle in (D).

Instead of fabricating the top chip to be the same size as the bottom chip, as in the

electrochemical liquid cell, this x-ray liquid cell has the top chip smaller than the bottom chip. Thus, the three electrodes on the bottom chip can be in direct contact with the washers on the home-made holder (Figure 2.5B), which are connected to an electrochemistry working station. This home-made holder is compatible with the Scanning Transmission X-ray Microscopy (STXM) in the Advanced Light Source (ALS) at Lawrence Berkeley National Laboratory. Figure 2.5C is the figure of the chamber after inserting this holder. As an example, lithium-rich material in electrolyte is loaded into the x-ray liquid cell and can be studied by STXM (Figure 2.5D and E).

2.5 Carbon film liquid cell

Carbon film liquid cell is introduced with improved spatial resolution and a fast fabrication process. As shown in Figure 2.6, one TEM grid is held by a tweezer with its carbon film facing upwards and the sample solution is drop-cast onto the ultrathin carbon supporting film. Then this TEM grid is carefully covered onto the second TEM grid. The two layers of carbon film would attach and form liquid pockets in between. After waiting about 2 minutes, this liquid cell sample is ready to be loaded onto the TEM holder for further TEM studies.

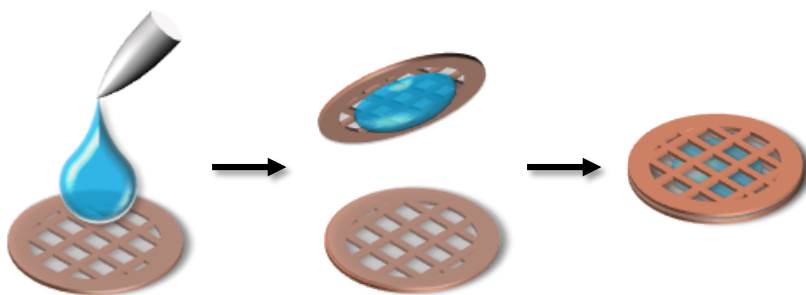


Figure 2.6 Illustration of making carbon film liquid cell by sandwiching sample solution between two commercial TEM grids with carbon film.

2.6 Polymer liquid cell

The carbon film liquid cell has promising properties for TEM studies but cannot be used for electrochemistry research due to the conductivity of carbon. To address this limitation, liquid cell with polymer support film can be used. A new type of electrochemical liquid cell was developed to allow for the studies of electrochemical processes in liquid electrolytes using in-situ LCTEM, and potentially at low temperatures.

Since commercial polymer films such as formvar are not compatible with electrolyte solution, polyimide was selected as the support film on consideration of its high chemical resistance, moderate sensitivity to the electron beam and high mechanical stability. And more importantly, polyimide was used to build up double film cell structure for cryo-TEM imaging in 1979.⁷⁹

The fabrication process flow of polyimide liquid cell is shown in Figure 2.7. The process starts from the commercial hole TEM grid, which is not covered by any supporting film. A layer of Al_2O_3 is sputtered onto the grid so that it would be less likely to cause a short

circuit during the biasing experiment.

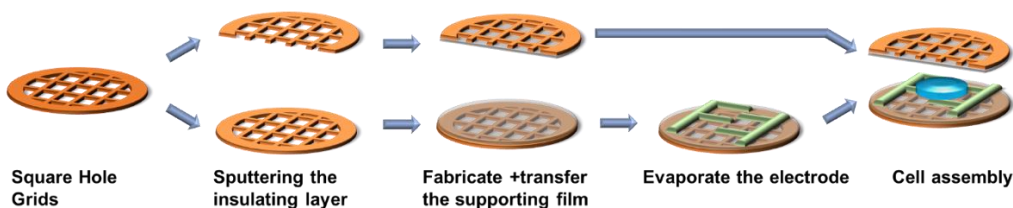


Figure 2.7 Fabrication process flow of fabricating electrochemistry liquid cell with polymer membrane.

Then the polyimide support film is fabricated and transferred onto the TEM grid, as shown in Figure 2.8A. For polyimide film fabrication, the prepolymers are diluted in N-methyl-2-pyrrolidone (NMP) at different concentrations. This solution is spin-coated onto a dummy wafer with 250 nm thermal oxide layer and cured at 200 °C for 30 min (Figure 2.8B). To release the membrane, the wafer is vertically immersed into 10% HF solution for 15 sec to etch the oxide layer on the wafer. Then the wafer is carefully tilted and merged into the water to release the membrane onto the water surface (Figure 2.8C). As indicated in Figure 2.8D, TEM grids are attached to the Gel-Pak, and the membrane is transferred by lifting Gel-Pak gently from water. When dried, the membrane can be seen clear on the Gel-Pak and attached with the TEM grids (Figure 2.8 E). The TEM grid can be removed from Gel-Pak by a tweezer with the membrane covering the grid surface.

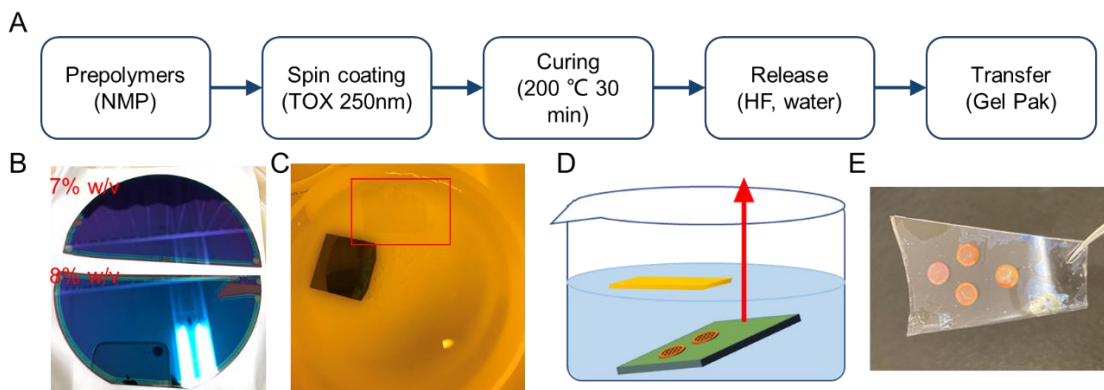


Figure 2.8 Fabrication and transfer of polyimide membrane. (A) Process flow of fabricating and transferring polyimide membrane. (B) Polyimide membrane after spin coating and curing. Different concentrations are used to make membrane of different thickness. (C) The polyimide membrane released onto water is highlighted in red square. (D) Schematic of putting TEM grid onto the Gel-Pak and lifting from the water so the free-standing polyimide membrane would attach onto the Gel-Pak. (E) Polyimide membrane is transferred onto the Gel-Pak and covered TEM grids.

The result of polyimide transfer is in Figure 2.9. Figure 2.9A shows one TEM grid well covered by polyimide membrane and one TEM grid with broken polyimide membrane. Pd nanoparticles are dissolved in solution and drop-casted onto the membrane for TEM observation. As in Figure 2.9B, at low magnification, the membrane is uniform and compatible with TEM imaging. At high magnification, the membrane is locally uniform

(Figure 2.9C). The Pd nanoparticle can be captured by HRTEM (Figure 2.9C). The furthest set of points in its Fast Fourier Transform (FFT) corresponds to 63 pm in real space, indicating the spatial resolution of this membrane can be down to tens of pm scale.

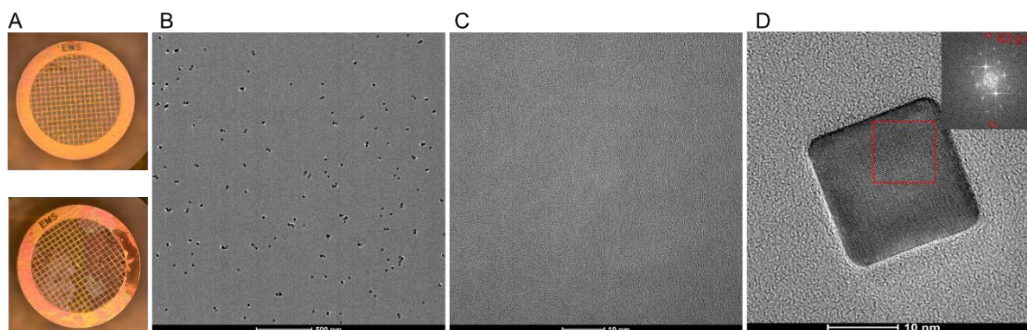


Figure 2.9 Polyimide membrane transferred onto TEM grid. (A) TEM grid after transferring 7% w/v polyimide membrane. The grid on the top has good membrane. The grid on the bottom has broken membrane. (B) TEM image of polyimide membrane loaded with Pd nanoparticles. (C) High magnification TEM image showing the local uniformity of polyimide membrane. (D) HRTEM image of Pd nanoparticle loaded onto the polyimide membrane. Inset is the FFT of red dotted square region. The furthest set of two points in FFT corresponds to distance of 63 pm in real space.

The next step is to pattern electrode onto the support film membrane. The TEM grids are loaded onto a 3D-printed alignment plate and covered by the shadow mask for e-beam evaporation of Pt electrode, as shown in Figure 2.10A. The TEM grid with the electrode on the polyimide membrane can be seen in Figure 2.10B. The left grid is good, while the right grid is misaligned with the shadow mask, so the electrode pattern is not in the right position. The grid is further checked by TEM. Figure 2.10C is the low magnification TEM image of electrodes supported by polyimide membrane. Figure 2.10D is the high-angle annular dark-field scanning transmission electron microscopy (HAADF-STEM) image of the electrode and membrane. EDS mapping of C, O, Pt indicates the distribution of these elements. Figure 2.10E is the EDS spectrum of Figure 2.10D and it shows the existence of only C, O, Cu, Pt elements, indicating the cleanness of the fabricated grid. Figure 2.10F is the EDS line scan of the dashed red box region in Figure 2.10D along the arrow direction. The line profiles of C, O, Pt element intensity indicate the uniformity of the support film and the sharpness of the evaporated electrode.

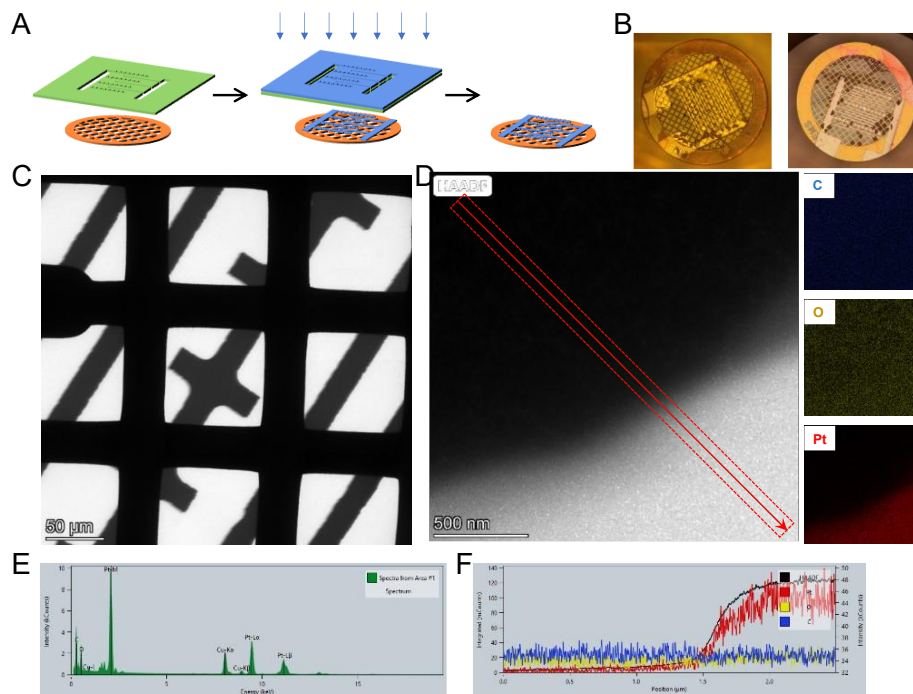


Figure 2.10 TEM image and EDS of 40 nm Pt electrode on 10% w/v polyimide membrane. (A) Schematic of shadow mask used to evaporate Pt electrode onto the polyimide membrane. The shadow mask is utilized to pattern the Pt electrode. (B) Image of the grid after evaporating 40nm Pt electrode. Left: the well-aligned electrode on the membrane. Right: the off-aligned electrode on the membrane. (C) TEM image of Pt electrode on the TEM grid. (D) HAADF-STEM image of the Pt electrode on polyimide membrane. On the right are the corresponding EDS maps of C, O, Pt element respectively. (E) The EDS spectrum of (D) indicates that the C, O, Cu and Pt elements are detected. (F) EDS line scan gives elemental intensity profiling as a function of scan distance in the red box in (D) along the red arrow direction. This demonstrates the uniformity of C and O and the sharpness of the Pt electrode.

3 In-Situ Study of Layered Nanostructure Growth at Various Temperatures

3.1 Introduction to layered materials

Layered materials have attracted significant interest and widespread study since the discovery of graphene. They can form different phases based on the arrangement of atoms and layer stacking. This offers them diverse structures and unique properties that are promising for a wide range of applications from optoelectronics to electronics, catalysis and energy storage.⁸⁰⁻⁸⁴ Recently the family of metal trihalides (MX_3) have attracted increasing attention as magnetic model structures in layered compounds. It was reported that some metal trihalides, such as CrI_3 and CrBr_3 , can be either ferromagnetic or antiferromagnetic depending on the number of layers, interlayer stacking order and external control such as electrostatic gating.⁸⁵⁻⁸⁸ So an understanding of the structural phases and the phase transitions of layered materials including the van der Waals (vdW) structures is of vital importance and will contribute to their controllable preparation.

Recent technical advances, such as TEM have enabled nanocrystal characterization with high spatial and temporal resolution during the transformation process.^{22, 42, 89-92} And valuable work has been conducted to investigate the structural phase transitions in layered materials.^{86, 93-100} Such phase transitions can be triggered by external activation, such as temperature, strain, laser, biasing and electron beam radiation.^{29, 101-105} Experiments and calculations showed the phase transformation process involves bond breaking, atomic displacements and atomic plane gliding.^{103, 106, 107} While new phases propagate and evolve in the crystal, intermediate phases or distorted regions can also form and these intermediate regions can correspond to higher energy states.^{92, 106} Some other phase transitions would introduce changes in interlayer structure, such as the layer stacking arrangement, while there is little change in the intralayer structure.^{101, 108} Understanding and control of such a wide range of atomic processes and nanoscale mechanisms are so far still elusive. For example open questions remain concerning the ways in which the different layers interact with each other and how the stacking configurations change at the atomic scale during dynamic processes, for example, growth and self-assembly.

3.2 Experimental setup and the layered structure of the InCl_3 crystal

Here, we develop novel in-situ liquid cell TEM method allowing to achieve cryogenic temperature, 0 °C and room temperature respectively. We report the structure and transformations of layered materials by using InCl_3 as a model system.

For the experimental setup, the traditional SiN_x liquid cell is replaced by the ultrathin carbon film liquid cell to overcome the fragility of SiN_x at low temperature and to promote spatial resolution. A $\sim 0.5 \mu\text{L}$ 40 mg/ml InCl_3 solution is drop-casted on one TEM grid and the second TEM grid is placed on top of the droplet to form a carbon film liquid cell. The liquid cell is then loaded onto a cryogenic holder to observe nanocrystal growth and transformation, as shown in Figure 3.1A.

Additionally, we use the mixture of ethanol and ice instead of liquid nitrogen as the cooling agent to achieve 0 °C with the cryogenic TEM holder. A schematic of the low temperature

technique is shown in Figure 3.1B. This cooling setup is stable while introducing less drift to the sample. The combination of the novel low temperature technique and carbon film liquid cell can achieve high spatial and temporal resolution in observations of nanomaterials. Most importantly, this liquid cell TEM setup offers the opportunity to reach various low temperatures by simply changing the coolant.

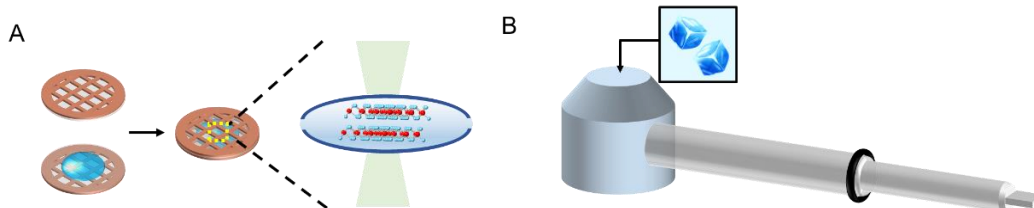


Figure 3.1 Schematic of setup for low temperature liquid cell experiment. (A) The carbon-film liquid cell preparation for in-situ LC-TEM studies. The sample solution is drop casted on the carbon film of a TEM grid and covered by another TEM grid. (B) Illustration for a cooling holder. The liquid cell is placed on the traditional cryogenic TEM holder for in-situ study. Liquid nitrogen or ice/ethanol mixture was added into the Dewar to achieve the in-situ study at cryogenic or sub-zero temperature.

This novel modified liquid cell TEM is used to study the structure and transformations of layered nanostructures, and here InCl_3 is chosen as the model system. The bulk InCl_3 crystal structure has been reported to be monoclinic, and is layered structure of the same structure type observed for the family of chromium trihalides, CrX_3 (where $\text{X} = \text{Cl}$, or I).^{109, 110}

As shown in Figure 3.2A, each In atom coordinates with six Cl atoms to form an octahedral prismatic structure. The single layer atomic structure of InCl_3 is shown in Figure 3.2B. On the left and center of Figure 3.2B are the side view and planar views of the structure respectively. The In atoms are represented by red dots and follow a honeycomb arrangement in the monolayer, as indicated by the red solid hexagons. Within the In honeycomb lattice, the top and bottom surfaces of Cl atoms form single triangles but with opposite orientation, indicated by the yellow dash line and blue solid line, respectively. The simplified illustration of the atomic structure using the different lines is shown in Figure 3.2C, where the blue triangles represent the Cl above the In while the yellow triangles show the Cl below the In. The 3D structure of monoclinic InCl_3 is shown in Figure 3.2D and the side view from Y axis is in Figure 3.2E, showing the alignment of atoms. Figure 3.2F is the simplified schematic of the In network in neighboring layers, indicating the stacking order of the crystal.

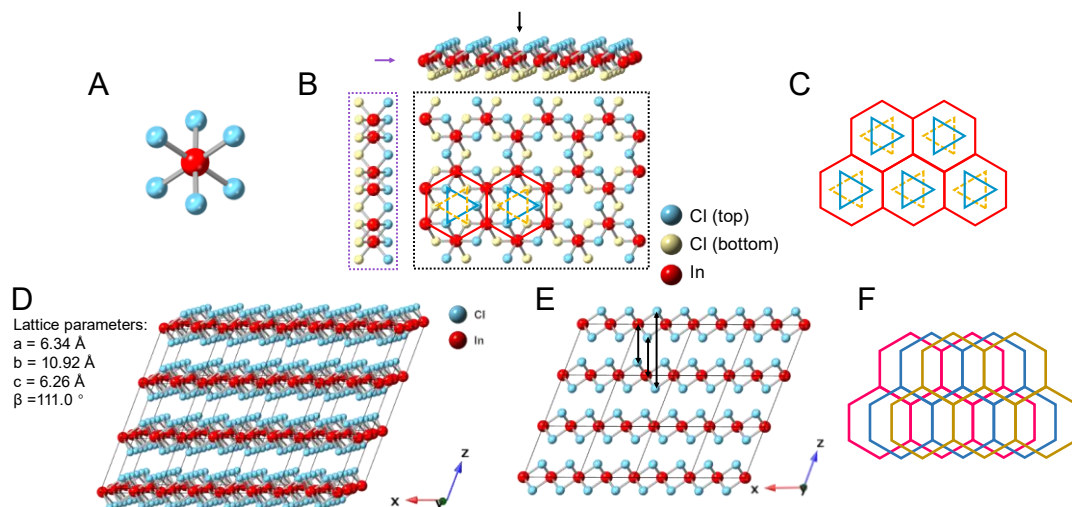


Figure 3.2 Structure model of monoclinic InCl₃ crystal. (A) The octahedral prismatic structure of InCl₃. Each In atom (red ball) is surrounded by six Cl atoms (blue balls) in an octahedral coordination. (B) Atomic model of the side view (purple square) and planar view (black square) of the single layer InCl₃. (C) Simplified atomic structure of the single layer InCl₃. (D) 3D model of the monoclinic InCl₃ crystal structure with lattice parameters on the left. The included angle between X and Z direction is 111°. (E) Side view from Y-axis of the crystal stacked by four layers. The double-sided black arrows indicate the alignment of atoms perpendicular to the monolayer plane. (F) Planar view of the monoclinic crystal indicating the stacking order of three layers. Each layer is simplified as the hexagon, which corresponds to the In atoms in the honeycomb lattice in each monolayer. The In network in each layer stacks in the order of magenta, blue, and yellow.

To observe the InCl₃ crystal structure, we first examine the InCl₃ atomic structure at cryogenic temperature. The InCl₃ solution is sandwiched between the carbon film liquid cell and loaded onto the cryogenic holder to cool down by liquid nitrogen. Figure 3.3A and B display the planar view and side view of InCl₃ crystal respectively. The inset of Figure 3.3A indicates the zone axis to be [001], which is the Z-axis direction indicated in Figure 3.2D. The inset of Figure 3.3B shows the corresponding FFT of the selected blue square region. One pair of dots is clearly observed and the d-spacing of 5.86 Å matches well with the reported interlayer distance of InCl₃ slabs, indicating that the image shows the side view of the layered material. The streaks in the FFT indicate the existence of the stacking faults.

Locally, the layers are stacked with several translations and form local new phases. Figure 3.3C shows the magnification of the selected region in the red square in Figure 3.3B. The layers are arranged in identical stacking, which is of AA stacking. The green box region in Figure 3.3B is magnified in Figure 3.3D. The material has ABC stacking and its twin structure above it. While the yellow box region in Figure 3.3B corresponds to AB stacking, as shown in Figure 3.3E. For the two stackings with translations, we connect the closest dots in neighboring layers and measure the angle with respect to the vertical direction. It is about 17° in the ABC phase and AB phase. These new phases we observed here are likely to be the metastable phases during phase transitions.

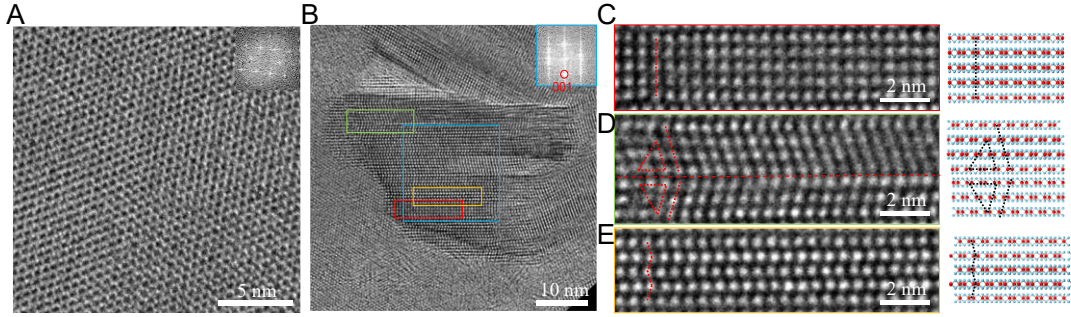


Figure 3.3 InCl₃ crystal structure observation using cryogenic TEM. (A) Cryo-EM image of InCl₃ crystal from planar view. Inset: FFT of the image indicating the zone axis to be [001]. (B) Cryo-EM image of InCl₃ crystal from side view. Inset: FFT of the blue square region. (C), (D), (E) are magnification of the selected red, green and yellow square region in (B) showing different stacking order between layers.

Since the interaction between different InCl₃ layers is weak vdW force, different layers tend to slide under fluctuations. The slide will lead to phase transition to form a new structure. To know the phase transition pathways of InCl₃ during the in-situ LCTEM study, the models for the possible InCl₃ structure are built.

To preserve the 3-fold symmetry of monolayer, the unit vectors for the crystal structure are chosen as the \vec{a} and \vec{b} in Figure 3.4A, which are used to quantify the relative translation between layers. And the vector \vec{c} is perpendicular to the plane.

Considering its symmetry, each layer can undergo translations relative to the layer below while the interlayer distance is fixed. All possible translations can be expressed as:

$$\text{Translation} = \frac{m}{3}\vec{a} + \frac{n}{3}\vec{b} \quad (m, n = 0, 1, 2)$$

Based on the stacking between layers, some structures can be considered energetically favored and some are unfavored.

For example, the bilayer structure with $\text{Layer2} = \text{Layer1} + \text{Translation}(\frac{2}{3}\vec{a} + \frac{1}{3}\vec{b})$ is shown in Figure 3.4B. The Cl in blue dashed plane lie in the cavity of the Cl triangle in magenta solid plane, suggesting that the Cl below In in the second layer (vertices of blue dashed triangle) do not lie above the Cl above the In in the first layer (vertices of magenta solid triangle). So this structure is energetically favored. However, the bilayer structure with $\text{Layer2} = \text{Layer1} + \text{Translation}(\frac{2}{3}\vec{a})$, shown in Figure 3.4C, is different. The Cl in blue dashed plane overlaps with the Cl triangle in magenta solid plane, as highlighted by the black cross. The overlapping of these two neighboring Cl planes indicates that this structure is energetically unfavored.

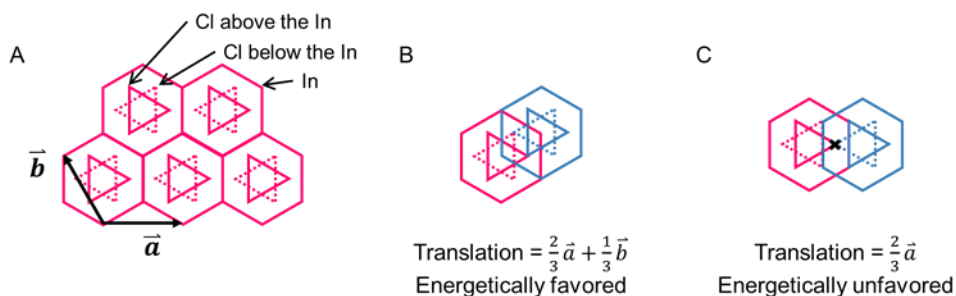


Figure 3.4 Illustration of the energetically favored and unfavored structure. (A) Representation of monolayer InCl₃ structure. The magenta hexagon represents the In honeycomb lattice. The magenta solid triangle and dashed triangle represent the Cl atoms above the In plane and below the In plane, respectively. Unit vectors \vec{a} and \vec{b} are selected to preserve the 3-fold symmetry of monolayer while \vec{c} is perpendicular to the monolayer. (B) Atomic model of the unit cell of bilayer InCl₃ with translation. The atoms in the first (bottom) monolayer sheet are represented in magenta following the style in (A). The atoms in the second (top) monolayer sheet are represented by the same line style but in blue color. The Cl in blue dashed triangle vertices do not lie above the vertices of magenta solid triangle, suggesting that the Cl in blue dashed plane lie in the cavity of the Cl triangle in magenta solid plane. (C) Atomic model of the unit cell of bilayer InCl₃ with unfavored translation. As indicated by the black cross, the Cl in blue dashed triangle vertices overlap the vertices of magenta solid triangle, suggesting that the Cl in blue dashed plane right above the Cl in magenta solid plane. So structural arrangement is relatively unstable.

According to the number of layers contained in the unit cell, we considered the case of 1, 2 and 3 layers.

For possible structures stacked by two layers in the unit cell, all possible translations and structures are listed in Table 3.1. Since monolayer InCl₃ sheet has translation symmetry and 3-fold rotation symmetry, some translations would generate equivalent structures, which is listed in the fourth column of the table. The bilayer structure, described by Layer 2 = Layer1 + Translation($\frac{m}{3}\vec{a} + \frac{n}{3}\vec{b}$), can be represented by parameter (m, n) and this label is listed in the fifth column. Then based on the rule illustrated in Figure 3.4, it is possible to tell if the structure is energetically favored.

Likewise, for possible structures with three layers in the unit cell, possible translations, unit cell label representation and the energetic favorability are analyzed in Table 3.2.



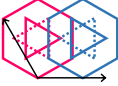





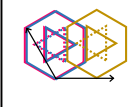
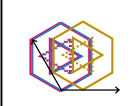
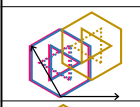
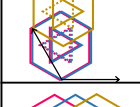
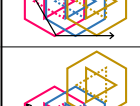
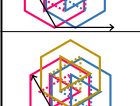

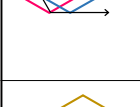
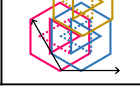
<ul style="list-style-type: none"> The monolayer InCl_3 sheet has translation symmetry, so translation1 and translation2 would generate equivalent structure if: $\text{Translation1} = \text{Translation 2} + i\vec{a} + j\vec{b}, i, j \in \mathbb{Z}$ The monolayer InCl_3 sheet is of 3-fold symmetry, so the crystal with translation $\frac{1}{3}\vec{a}$ is equivalent to the crystal with translation $\frac{1}{3}\vec{b}$ $\text{Translation}\left(\frac{1}{3}\vec{a}\right) = \text{Translation}\left(\frac{1}{3}\vec{b}\right) = \text{Translation}\left(-\frac{1}{3}\vec{a} - \frac{1}{3}\vec{b}\right) = \text{Translation}\left(\frac{2}{3}\vec{a} + \frac{2}{3}\vec{b}\right)$ All bilayer InCl_3 crystal can be represented by parameter (m, n) corresponding to translation as : $\text{Layer2} = \text{Layer1} + \text{Translation}\left(\frac{m}{3}\vec{a} + \frac{n}{3}\vec{b}\right), m, n = 0, 1, 2$ 					
Number of layers in unit cell	Unit cell structure	Translation: between upper layer and bottom layer	Equivalent to the structure with translation	Unit cell structure label	Note: Considering the location of Cl atoms as mentioned in Figure 3.4, if the structure is energetically favored?
 2 nd layer/ top layer in the unit cell  1 st layer/ bottom layer in the unit cell		$\frac{2}{3}\vec{a}$	$\frac{2}{3}\vec{b}$ $\frac{1}{3}\vec{a} + \frac{1}{3}\vec{b}$	(2,0)	No.
		$\frac{1}{3}\vec{a}$	$\frac{1}{3}\vec{b}$ $\frac{2}{3}\vec{a} + \frac{2}{3}\vec{b}$	(1,0)	No. Since the unit cell is repeated in the crystal, $\text{layer3} = \text{layer1}$ $= \text{layer2} + \text{translation}\left(-\frac{1}{3}\vec{a}\right)$ $= \text{layer2} + \text{translation}\left(\frac{2}{3}\vec{a}\right)$ So the stacking of the 3 rd layer and the 2 nd layer makes the structure energetically not favored.
		$\frac{2}{3}\vec{a} + \frac{1}{3}\vec{b}$	$\frac{1}{3}\vec{a} + \frac{2}{3}\vec{b}$	(2,1)	

Table 3.1 Possible structural models of bilayer InCl_3 with lateral translation. Magenta and blue represent the atoms in the first (bottom) monolayer and second (top) monolayer in the unit cell, respectively. Considering the translation symmetry and 3-fold rotation symmetry of monolayer InCl_3 sheet, some translations would produce equivalent structures and they are listed in the table. The location of Cl in neighboring layers would indicate whether each crystal structure is energetically favored, and this is labeled in the last column of the table.

- All triple layer InCl_3 crystal can be represented by parameter (m, n, i, j) corresponding to translation1 and translation2 as :

$$\text{Layer2} = \text{Layer1} + \text{Translation1} \left(\frac{m}{3} \vec{a} + \frac{n}{3} \vec{b} \right), m, n = 0, 1, 2$$

$$\text{Layer3} = \text{Layer2} + \text{Translation2} \left(\frac{i}{3} \vec{a} + \frac{j}{3} \vec{b} \right), m, n = 0, 1, 2$$
- Based on the 3-fold rotation symmetry, only the structures with Translation1 = $0, \frac{1}{3} \vec{a}, \frac{2}{3} \vec{a} + \frac{1}{3} \vec{b}, \frac{2}{3} \vec{a}$ need to be considered.
- The triple-layer case with any translation equals to $\frac{2}{3} \vec{a}, \frac{2}{3} \vec{b}, \frac{1}{3} \vec{a} + \frac{1}{3} \vec{b}$ would be energetically unfavored.
- Considering that the unit cell is repeated in the crystal, the structure with Translation1 = $\left(\frac{m}{3} \vec{a} + \frac{n}{3} \vec{b} \right)$ and Translation2 = $\left(\frac{i}{3} \vec{a} + \frac{j}{3} \vec{b} \right)$ must be equivalent to some structure with Translation1' = $\left(\frac{i}{3} \vec{a} + \frac{j}{3} \vec{b} \right)$. So the latter can be omitted in the exhaustion method.

Number of layers in unit cell	Unit cell structure	Translation1: layer2 = layer1 + translation1	Translation2: layer3 = layer2 + translation 2	Unit cell structure label	Note: considering the location of Cl atoms as mentioned in Figure 3.4, if the structure is energetically favored?	
3  3rd layer/ top layer in the unit cell  2nd layer/ middle layer in the unit cell  1st layer/ bottom layer in the unit cell		$\frac{0}{3} \vec{a} + \frac{0}{3} \vec{b}$	$\frac{2}{3} \vec{a}$ $\frac{2}{3} \vec{b}$ $\frac{1}{3} \vec{a} + \frac{1}{3} \vec{b}$	(0,0,2,0)	No	
				$\frac{1}{3} \vec{a}$ $\frac{1}{3} \vec{b}$	(0,0,1,0)	No
				$\frac{2}{3} \vec{a} + \frac{2}{3} \vec{b}$	(0,0,2,1)	
				$\frac{1}{3} \vec{a} + \frac{2}{3} \vec{b}$	(0,0,1,2)	
			$\frac{1}{3} \vec{a}$	$\frac{1}{3} \vec{a}$	(1,0,1,0)	Monoclinic structure
				$\frac{2}{3} \vec{a} + \frac{2}{3} \vec{b}$	(1,0,2,2)	
				$\frac{1}{3} \vec{b}$	(1,0,0,1)	
				$\frac{2}{3} \vec{a} + \frac{1}{3} \vec{b}$	(1,0,2,1)	No Considering the repeated unit cells in the crystal, layer4 = layer1 = layer3 + translation $\left(-\frac{1}{3} \vec{b} \right)$ = layer3 + translation $\left(\frac{2}{3} \vec{b} \right)$
				$\frac{1}{3} \vec{a} + \frac{2}{3} \vec{b}$	(1,0,1,2)	No layer4 = layer1 = layer3 + translation $\left(\frac{1}{3} \vec{a} + \frac{1}{3} \vec{b} \right)$

Number of layers in unit cell	Unit cell structure	Translation1: <i>layer2</i> = <i>layer1</i> + <i>translation1</i>	Translation2: <i>layer3</i> = <i>layer2</i> + <i>translation 2</i>	Unit cell structure label	Note : considering the location of Cl atoms as mentioned in Figure 3.4, if the structure is energetically favored?	
3		$\frac{1}{3}\vec{a}$	$\frac{2}{3}\vec{a}$	(1,0,2,0)	No. Equivalent structure with (0,0,1,0).	
				$\frac{1}{3}\vec{a} + \frac{1}{3}\vec{b}$	(1,0,1,1)	No. Equivalent structure with (1,0,2,1).
				$\frac{2}{3}\vec{b}$	(1,0,0,2)	No. Equivalent structure with (1,0,1,2).
	3 rd layer/ top layer in the unit cell		$\frac{2}{3}\vec{a} + \frac{1}{3}\vec{b}$	$\frac{2}{3}\vec{a} + \frac{1}{3}\vec{b}$	(2,1,2,1)	
		$\frac{1}{3}\vec{a} + \frac{2}{3}\vec{b}$			(2,1,1,2)	Equivalent structure with (0,0,2,1).
		$\frac{2}{3}\vec{a}$			(2,1,2,0)	No. Equivalent structure with (1,0,2,1).
	2 nd layer/ middle layer in the unit cell		$\frac{1}{3}\vec{a} + \frac{1}{3}\vec{b}$	$\frac{1}{3}\vec{a} + \frac{1}{3}\vec{b}$	(2,1,1,1)	No. Equivalent structure with (1,0,2,1).
		$\frac{2}{3}\vec{b}$			(2,1,0,2)	No. Equivalent structure with (1,0,2,1).
		$\frac{2}{3}\vec{a}$			(2,0,2,0)	No.
	1 st layer/ bottom layer in the unit cell		$\frac{2}{3}\vec{a}$	$\frac{2}{3}\vec{a}$	(2,0,1,1)	No.
		$\frac{1}{3}\vec{a} + \frac{1}{3}\vec{b}$			(2,0,1,1)	No.
		$\frac{2}{3}\vec{b}$			(2,0,0,2)	No.

Table 3.2 Possible structural models of triple layer InCl_3 with lateral translation. Magenta, blue and yellow represent the atoms in the first (bottom), second (middle) and third (top) monolayer in the unit cell, respectively. The representation style follows that in Table 3.1. By exhaustion method, all potential structures are listed and some equivalent structures can be omitted or labeled.

Excluding the equivalent structures and energetically unfavored ones, all the potential and energetically favored structures are listed in Table 3.3. Only In network are drawn to show

the stacking between layers and Cl triangles are omitted to simplify the representation of the structure.

So for the listed possible translations and corresponding structure models in Table 3.3, the possible zone axes that would produce the side view AA or AB, ABC with distance and angles matching that in the side view in Figure 3.3 were summarized. Then for the later in-situ study, we would be able to identify the possible structures and transformations by comparing the side view structures in high-resolution TEM observation and possible models in Table 3.3.



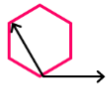

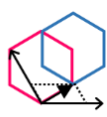
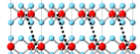
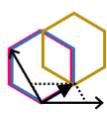
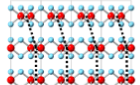


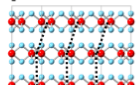


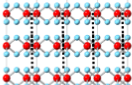
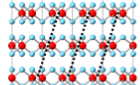

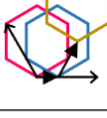
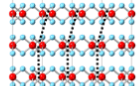

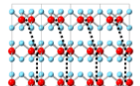

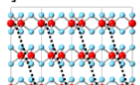
Number of layers in unit cell	Unit cell structure	Unit cell structure label	Simplified unit cell	Side view: identical	Side view: tilted	
				 Cl	 In	
1			1T (1 layer, Trigonal)	[100], A 		
2		(2,1)	2T (2 layers, Trigonal)		[100], [010], [-1-10] AB 	
3		(0,0,2,1)	3T (3 layers, Trigonal)		[100], [010], [-1-10], ABB 	
	 Top layer		(0,0,1,2)	3T (3 layers, Trigonal)		[100], [010], [-1-10], ACC 
	 Middle layer		(1,0,1,0)	1M (1 layer, Monoclinic)	[100], AAA 	[010],[110], ACB 
	 Bottom layer		(1,0,2,2)	3T (3 layers, Trigonal)		[100], [010], [-1-10], ACC 
			(1,0,0,1)	3T (3 layers, Trigonal)		[100], [010], [-1-10], ABB 
			(2,1,2,1)	3H (3 layers, Hexagonal)		[100], [010], [-1-10] ABC 

Table 3.3 Summary for possible structural model of mono-, bi-, triple-layers InCl_3 with lateral translation. As shown in the left panel, each monolayer sheet is represented by a solid hexagon for In atoms. Cl triangles are omitted for simplicity. Magenta, blue and golden represent the bottom, middle and top layer of the triple-layer InCl_3 , respectively. By translating the layer against the layer below, different stacking structures are obtained. All potential energy favorable structural models are listed in the second column of the table. And the side views that match the cryogenic temperature observations are listed with possible zone axes.

3.3 Lateral translation of layered InCl_3 in solution at room temperature

The atomic pathway of phase transition from AA to AB is shown in Figure 3.5A. To quantify the sliding between layers, the clusters are represented by dark dots in Figure 3.5B. The clusters are detected by convolving the image data with Laplacian of Gaussian filter (LoG), which would generate the local maximum signal at the center of each blob. Like Figure 3.3C, D and E, the neighboring clusters in adjacent layers are connected by line and the angles are measured with respect to the vertical direction. The color of the line represents the absolute value of the angle. And the sign of the angle indicates whether it is tilted to the right or the left. The color bar is shown in the bottom right in Figure 3.5.

The angle between the top two layers (the first layer and the second layer) are measured and labeled as the 1st set angle. The angles of other adjacent atomic layers from top to bottom (the second layer to the seventh layer) were also measured and labeled as 2nd, 3rd, 4th, 5th and 6th sets of angles. Since each atomic layer has 10 dots (Figure 3.5B), we can get 10 angles from each set. Figure 3.5C shows the change of the average angle of each set over time. Here the red star corresponds to the average angle between the two layers in the orange box in Figure 3.5A. It changes from around 0° to about -17°, while the average angles of other sets remain relatively stable at either 0° or 17°. 0° is AA stacking while 17° is AB stacking. So, on average, the two layers in the orange box transform from AA to AB stacking.

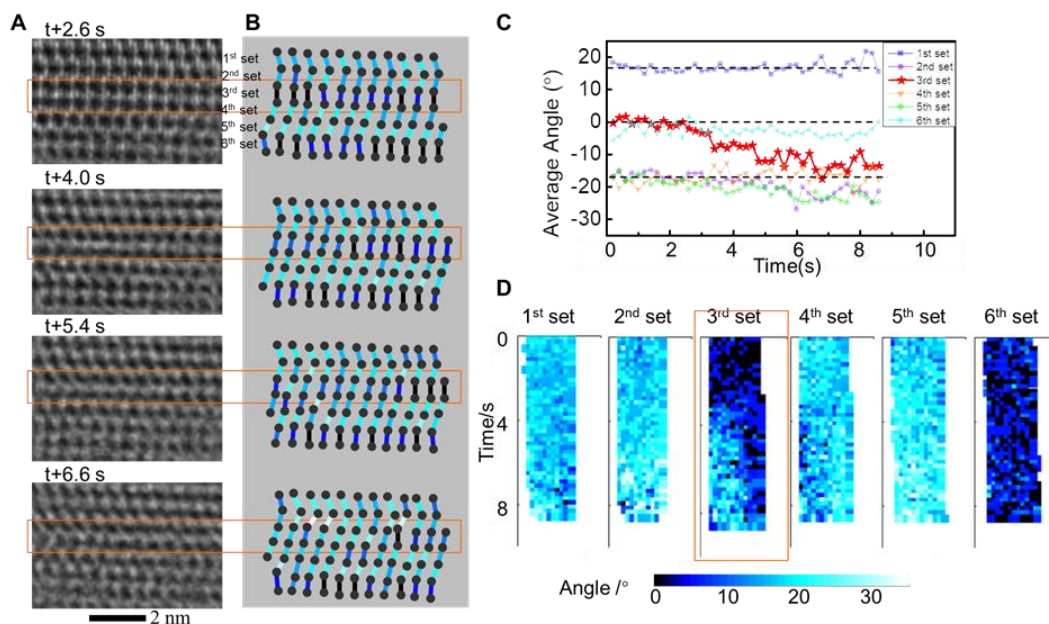


Figure 3.5 Lateral translation of layered InCl_3 in solution at room temperature. (A) Sequential TEM images showing the lateral translation of InCl_3 in solution at room temperature. (B) The corresponding structural model shows the details of lateral translation of In atoms. The color of the line between adjacent In atom clusters represents the absolute value of the angle with the vertical direction. (C) Change of average angle (with the vertical direction) of the seven atomic layers of InCl_3 over time. (D) Color map of the local lateral translation of InCl_3 in each layer.

To further see the local translations, Figure 3.5D demonstrates the sliding angles of all clusters in each neighboring two layers. For example, the 1st figure corresponds to the angle of the lines connecting clusters in the 1st and 2nd layer. The horizontal axis corresponds to lines in the layer from left to right while the vertical axis represents time. We can see that the angle of these layers outside the orange box does not change much. So the stackings are locally stable to be AA or AB. But for the 3rd set angles in the orange box, initially, the angles of all lines are close to 0°, suggesting that it is all well aligned in AA stacking. Then, the angle on the left side increases gradually and extend to the right side. This means that the AA stacking is transformed to AB from left side to right side gradually. The In clusters within the layer move one after another, rather than the clusters within the same layer moving together simultaneously. Therefore, we consider the transformation is consistent with the passage of a partial dislocation that changes the stacking sequence, rather than the whole layer shifting uniformly.

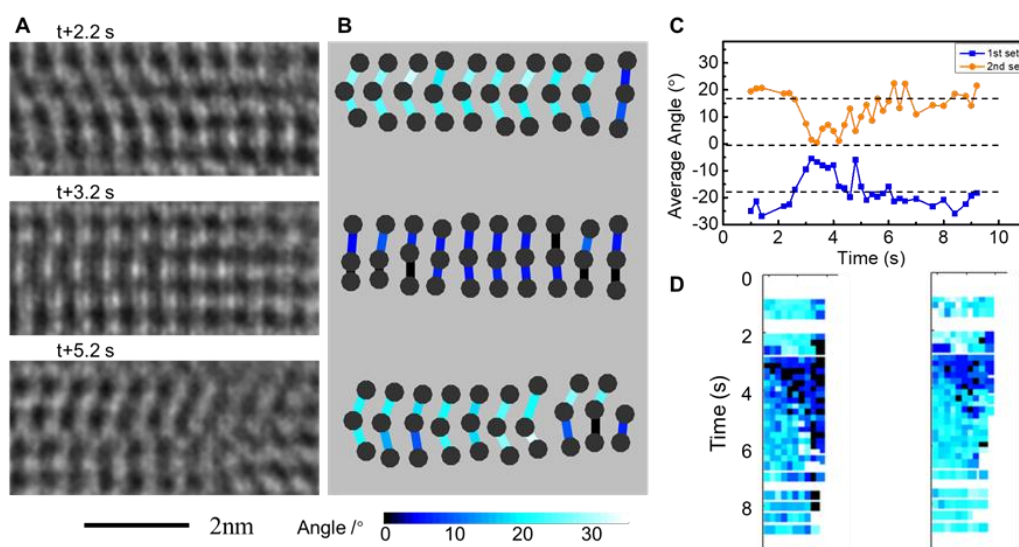


Figure 3.6 Reversible phase transition of layered InCl₃ in solution at room temperature. (A) Sequential TEM images showing the reversible phase transition of InCl₃ in solution at room temperature. (B) The corresponding atomic model shows the details of lateral translation of the stacking from ABA to AAA, and then back to ABA. The color of the line between adjacent In atoms represents the absolute value of the angle with the vertical direction. (C) Change of averaged angle (with the vertical direction) of the three atomic layers of InCl₃ over time. (D) Color map shows the reversible phase translation of InCl₃.

The reversible transformations can also be observed in another region of the crystal. From the time series images (Figure 3.6A) and the corresponding models (Figure 3.6B), we can see that the three layers of InCl₃ are initially in ABA stacking. Then the InCl₃ suddenly gets to AAA stacking and returns into ABA stacking again. The lateral translation can be quantitatively analyzed by the angle between layers. Here the blue and orange curves in Figure 3.6C correspond to the average angle of the 1st set (between the top layer and middle layer) and 2nd set (between middle and bottom layer). As can be seen, the angle of the 1st set changes from around -17° to about 0°, and then back to -17°. The angle of the 2nd set also shows the same characteristics. It first changes from 17° to about 0°, and then back to 17°. Similarly, we selected the key frames and showed the angle changes by color map

(Figure 3.6D). From the key frames and the processed result, we can see that initially the 3 layers are in ABA stacking. Then the right side suddenly gets to AAA stacking and gradually returns into ABA stacking again. And the transition happened as the In clusters moved one by one sequentially.

3.4 The layer-by-layer growth of the vertical InCl_3 crystal at room temperature

The in-situ TEM study demonstrates the dynamics of the vertical growth and evolution of InCl_3 crystal layer at room temperature and the snapshots are presented in Figure 3.7. The time-resolved figures in Figure 3.7A show the successive addition of new layers at the reaction front. Simultaneously, the projection length of existing layers also increases slightly. This is because the new layer formation is energetically more favorable than in-plane growth of existing layers. Figure 3.7B shows the formation detail of an additional layer. The growth of a new monolayer is initiated from the edge of the existing InCl_3 layers at the reaction front and then it subsequently grows into a new slab by the attachment of growth species at the step site. The step sites are more energetically active, so the monomers are more likely to attach to them. This observation is consistent with previous discovery that new monolayer begins to nucleate on to already formed layers from either step edge or from the center in a layer-by-layer mode.⁹⁰ Even more atomic scale details are revealed here in Figure 3.7C. The formation and evolution of two new layers, indicated by yellow arrows and white arrows respectively, is involved with dissolution-reprecipitation process at the reaction front. The dissolution is caused by thermodynamic disturbance from the nearby solution, while the precipitation is accompanied with growth species diffusion in liquid and its attachment onto the surface kink. When the competing dissolution process outweighs the precipitation, removal of monomers at the kinks can be observed.

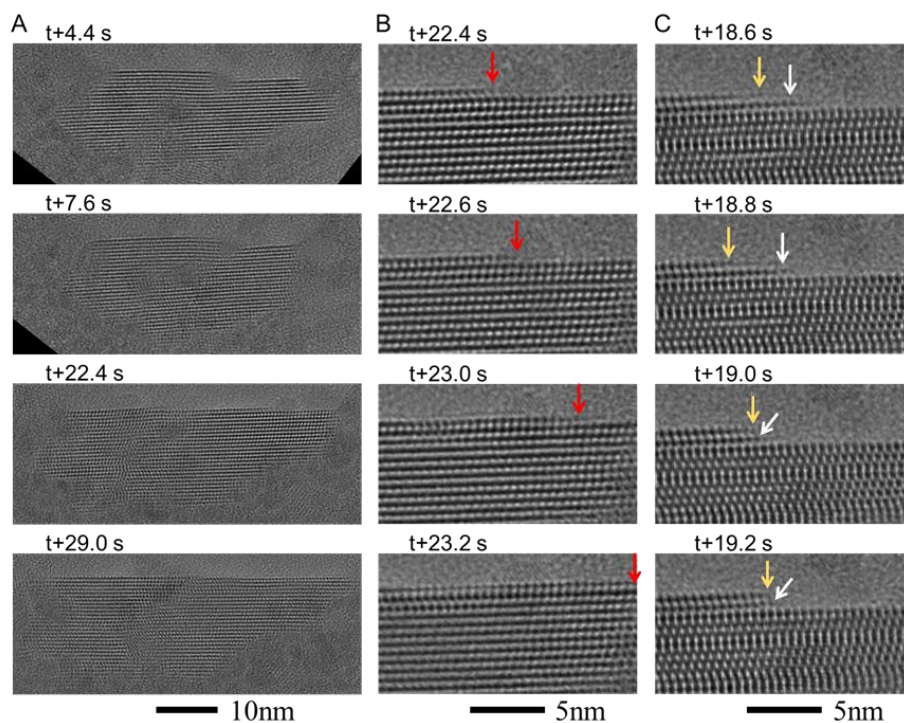


Figure 3.7 The layer-by-layer growth and evolution of the vertical InCl_3 crystal in solution at room temperature. (A) Sequential TEM images showing the layer-by-layer growth process. New layer addition and existing layer growth can be observed. (B) Sequential TEM images showing single layer growth at the reaction front. The red arrows show the atomic layer propagation in the process. (C) Sequential TEM images showing process of dissolution–reprecipitation at the kink site. The yellow arrows show the top layer dissolves and reprecipitates at the kink site. The white arrows indicate the second layer dissolves and reprecipitates at the kink site.

In addition to the phase transition between ordered crystals shown above, we also observe crystallization of local amorphous domains. Figure 3.8 demonstrates the structural amorphous-to-crystalline transition. As highlighted in the orange dashed area, the amorphous region changes in size and evolves into crystalline structure, which is also the result of dissolution–reprecipitation of ions. This structural rearrangement leads to increase in the crystallinity and stability of the crystal. Different from direct transformations in Figure 3.5 and Figure 3.6 that clusters rearrange directly within the crystal, this amorphous-to-crystalline transition involves nucleation in solution.

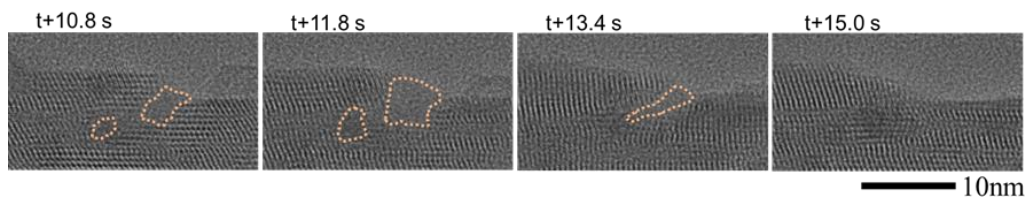


Figure 3.8 Sequential TEM images showing the amorphous to crystal transition during growth process.

3.5 Behavior of layered InCl_3 in solution at low temperature of $0\text{ }^\circ\text{C}$

To understand the temperature effect on translation between layers, we study the InCl_3 structure at low temperatures. The low temperature of $0\text{ }^\circ\text{C}$ is achieved and stabilized by adding the mixture of ice and ethanol into the Dewar of a cryogenic TEM holder.

Figure 3.9A shows the initial structure of the vertical InCl_3 crystal in solution at $0\text{ }^\circ\text{C}$ at 0.2 s. Like the experiment at cryogenic temperature, we can observe AA stacking and ABC stacking in the yellow box and blue box regions. Figure 3.9B shows the magnification of the selected blue square region and the layers are stacked in ABC with an angle of around 17° . This is consistent with the proposed structures and cryo-EM result. Until 23.8 s, this phase ABC is stable during the process and stacking configurations can be maintained. Likewise, the crystal selected in yellow box is magnified in Figure 3.9C and it is of AA phase. The AA phase is also stable. The vdW force between layers is weak and the energy barrier between two phases is small. The lower temperature leads to lower thermal fluctuation energy and slower kinetics. Besides, the lower temperature would cause slower ion diffusion in the liquid. So, in the highlighted areas, the phases at low temperature are well preserved and go through no structural transformations at $0\text{ }^\circ\text{C}$ for more than 20 s.

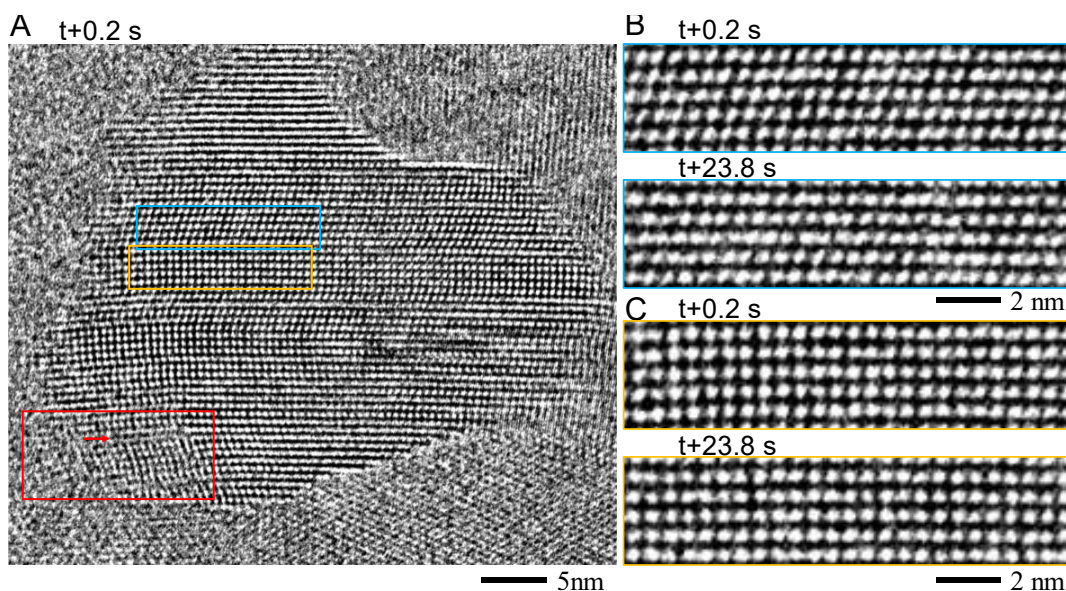


Figure 3.9 Behavior of layered InCl_3 in solution at the low temperature of $0\text{ }^\circ\text{C}$. (A) Initial TEM image of InCl_3 crystal at $0\text{ }^\circ\text{C}$ at 0.2 s. (B) Magnification of the selected blue square region in (A) at 0.2 s and 23.8 s respectively, showing that the crystal could maintain ABC phase at $0\text{ }^\circ\text{C}$. (C) Magnification of the selected yellow region in (A) at 0.2 s and 23.8 s respectively. The AA phase is stable during the observation period.

Figure 3.10A is the magnification of the crystal in the red box region in Figure 3.9A and reveals the removal of dislocation in the InCl_3 crystal in solution at $0\text{ }^\circ\text{C}$. At 7.0 s, there exists a dislocation in the crystal and the extra half layer is highlighted by the cyan arrow. The cyan arrows always point to the same half layer as reference. Figure 3.10B is the corresponding model and the balls represent the clusters in each monolayer. The cyan balls are the clusters in the half layer pointed by the cyan arrow and is labeled as the first layer. The neighboring layers below it are marked as the second, third, fourth, fifth and sixth

layers in order. The clusters of each layer are represented by orange, blue, magenta, green and yellow balls respectively, as indicated in the top figure in Figure 3.10B. From 7.0 s to 19.6 s, the first half layer shrinks by diffusion of ions and vacancies, causing the dislocation to climb. And the dislocation core moves left. Then after 19.6 s, the second layer is broken and its right half reconnects with the first half layer to form a complete new layer. The dislocation glide happens with dislocation core moving downwards. The shear stress may be caused by thermodynamic fluctuations. Then from 21.4 s to 21.6 s, the third layer is broken and reconnects with the second layer. Finally at 22.0 s, a perfect crystal is formed. We hypothesize that at 0 °C, structural phase transitions are suppressed due to the slow kinetics, so that the dislocation removal details can be observed. This evolution process shows dislocation migration through first climbing to the adjacent location and then gliding to the final position, which is accompanied by recovery or crystallization, until a perfect crystal is formed.

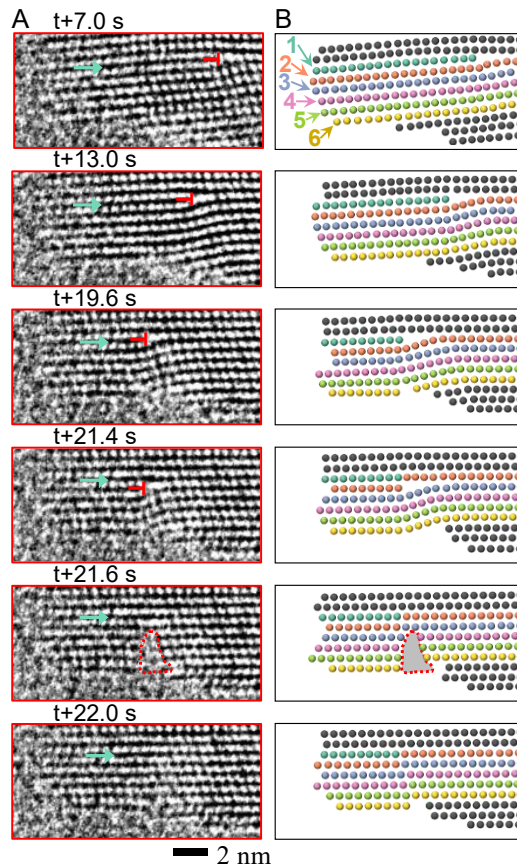


Figure 3.10 Sequential TEM images showing the removal of dislocation in InCl₃ crystal with dislocation climbing and gliding. (A) Magnification of the selected red region in Figure 3.9A with dislocation. Cyan arrows pointing to the same layer as reference. The dislocation core moves left, followed by layer breaking and recombination process at neighboring layers. (B) The corresponding atomic model. The colored balls indicate the clusters within the same layer initially at 7.0 s. The cyan balls indicate the clusters in the initial half layer pointed by cyan arrow in (A).

4 The effect of temperature on nucleation and growth of copper nanoparticles during electrochemical reactions

Reproduced in part with permission from: Qiubo Zhang, Jiawei Wan, Junyi Shangguan, Sophia Betzler and Haimei Zheng, "Influence of sub-zero temperature on nucleation and growth of copper nanoparticles in electrochemical reactions" *Iscience* 24, no. 11 (2021): 103289.

4.1 Introduction to copper nanoparticles synthesis

Copper-based nanomaterials capable of converting carbon dioxide into renewable fuels and feedstocks have received increasing attention as highly active catalysts for electrochemical carbon dioxide reduction (CO₂ RR).¹¹¹⁻¹¹³ During the CO₂ RR process, copper-based catalysts are the only ones that can generate various multi-carbon products such as ethylene, ethanol, and propanol.¹¹⁴ Their catalytic activity and selectivity depend on the microscopic structure and surface morphology, such as nanoparticle shape, size, surface configuration, and chemical state.¹¹⁵⁻¹¹⁹ Therefore, exploring and manipulating the formation of copper nanomaterials during the synthesis process is crucial for the functional design of nanomaterials as well as for optimizing their catalytic performance.

Electrodeposition is considered as one of the ideal methods to prepare catalysts with hierarchical structures because it has the benefit of simple steps and quick operation and it can avoid the complexity of high-temperature synthesis process, which is required by many other synthesis methods.^{120, 121} For electrodeposition, many factors can alter the nucleation and growth of nanocrystals, resulting in final products with different structures and morphologies.¹²² For example, current density has been reported to affect nucleation density, size, and shape of nanocrystals.¹²³ The pH can affect the structure and properties of metal deposits.¹²⁴ Adding additives to the solution can suppress lithium dendrite formation during battery operation.⁷⁵ Despite reports on the effect of temperature on electrodeposition have been reported,^{125, 126} it remains unclear how low temperature affects the nucleation and growth of copper nanoparticles. There are two main reasons. First, it is difficult for general electrolytes to remain in liquid state and maintain good electrical conductivity at low temperatures. Second, characterizing samples is challenging because they may change after removal from the cryogenic environment.

In this study, we prepared two kinds of hierarchical nanostructures with Cu nanoparticles adhered to the Cu nanowires at both sub-zero temperature (-20 °C) and room temperature (20 °C). We characterized the Cu nanostructures by TEM with various techniques. We found that low temperatures influence the size, shape, and crystallinity of the resulted Cu nanoparticles. The reduced reaction rate leads to multiple nucleation sites of metal nanoparticles, which is the main reason for the different growth modes of Cu nanoparticles at low temperatures. At low temperatures, the low surface diffusion rate of adatoms is responsible for the poor crystallinity.

4.2 Experimental setup and structural characterization of the as-prepared Cu nanowires

We performed experiments using well-designed equipment for electrochemical and sub-zero temperature control. Figure 4.1A shows the schematic illustration of the experimental setup. Before the experiments, we pre-synthesized copper nanowires so that they could be loaded onto a carbon film-supported TEM copper grid. In synthesized copper nanowires, we mixed 17 mg of CuCl_2 , 50 mg of D-(+)-glucose and 180 mg of hexadecylamine with 10 mL of deionized water in a glass vial. The final solution was then sonicated for 30 min at room temperature. Afterward, we transferred the vial to an oil bath and heated it at $100\text{ }^\circ\text{C}$ for 6 h with magnetic stirring. Finally, we washed the synthesized copper nanowires five times with hexane/ethanol (1:1 volume) and collected them by centrifugation at 9500 rpm for 5 min.

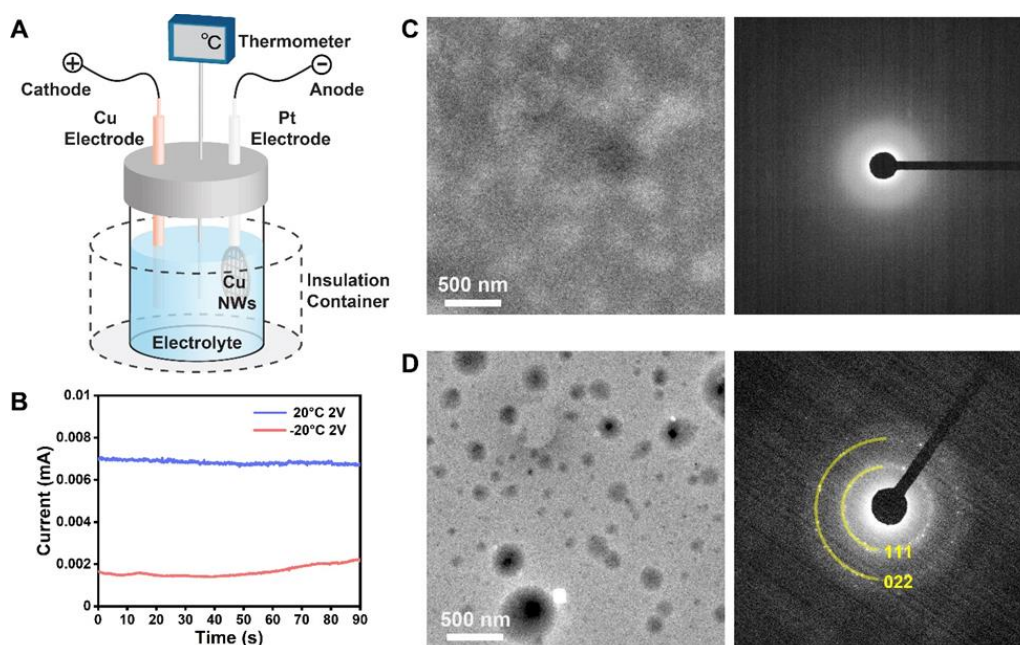


Figure 4.1 Illustration of experimental setup and characterization of 1.0 M LiPF_6 in $\text{EC/DEC} = 50/50$ (v/v) electrolyte at room temperature ($20\text{ }^\circ\text{C}$) and sub-zero temperature ($-20\text{ }^\circ\text{C}$), respectively. (A) A schematic diagram of the experimental setup to apply biasing at different temperatures. (B) Current versus time plot of the electrodeposition processes at $20\text{ }^\circ\text{C}$ and $-20\text{ }^\circ\text{C}$. (C) TEM and electron diffraction images of the electrolyte in a carbon film liquid cell at $20\text{ }^\circ\text{C}$. (D) TEM and electron diffraction images of the electrolyte in a carbon film liquid cell at $-20\text{ }^\circ\text{C}$. Solid precipitations are found in the electrolyte.

After the samples were prepared, we connected the copper grid to the platinum anode and the cathode was made of copper. Both electrodes are attached to the electrochemical workstation and immersed in 5 mL commercial electrolyte of 1.0 M LiPF_6 in ethylene carbonate/diethyl carbonate ($\text{EC/DEC} = 50/50$ (v/v)). The EC/DEC mixed solution was chosen as the electrolyte because of its low freezing point, its capability to remain liquid and good electrical conductivity even at sub-zero temperatures.¹²⁷ We then sealed the electrolyte in a ceramic container, which has an insulation container made of polystyrene

around it to maintain the temperature. We use liquid nitrogen for temperature control, first cooling the insulation device to the desired sub-zero temperature, then waiting until it reaches the desired temperature and starts biasing. Because polystyrene has a low thermal conductivity ($0.033 \text{ W}/(\text{m}\cdot\text{K})$),¹²⁸ the low temperature can be maintained for a few minutes.

In the operations, 2 V of constant voltage operation for 90 s was used in both room temperature ($20 \text{ }^\circ\text{C}$) and sub-zero temperature ($-20 \text{ }^\circ\text{C}$) experiments. The real-time temperature is measured by using a thermoelectric detector. As shown in Figure 4.1B, the current stabilized at 0.007 mA at 20°C and 0.002 mA at -20°C . Since the ion migration in the electrolyte slows down with decreasing temperature, the current density is small at low temperatures.

In order to further find out how the structure of the electrolyte differs at different temperatures, we used LCTEM combined with cryo-EM to image the electrolyte at $20 \text{ }^\circ\text{C}$ and $-20 \text{ }^\circ\text{C}$. Figures 4.1C and 4.1D show the TEM images and selected area electron diffraction (SAED) patterns of the electrolyte at $20 \text{ }^\circ\text{C}$ and $-20 \text{ }^\circ\text{C}$. We pipetted a drop ($1 \mu\text{L}$) of electrolyte (1.0 M LiPF_6 in EC/DEC=50/50 (v/v)) onto one carbon film-coated grid, which was then covered with another carbon film to form a thin liquid cell. At room temperature, no diffraction spots appear in the diffraction pattern, which indicates that the electrolyte exhibits a homogeneous amorphous liquid structure (Figure 4.1C). To achieve cryogenic temperatures while liquid-cell TEM imaging, we used a cryogenic EM stage, which allows the liquid to be cooled and stabilized at -20°C . As shown in the TEM image, at $-20 \text{ }^\circ\text{C}$, the electrolyte consists of liquid and solid phases (Figure 4.1D). The corresponding diffraction spots fit the $\{111\}$ and $\{022\}$ facet spacing of the solid EC. At temperatures below zero, solid EC precipitates out of the liquid electrolyte, reducing the conductivity of the electrolyte.

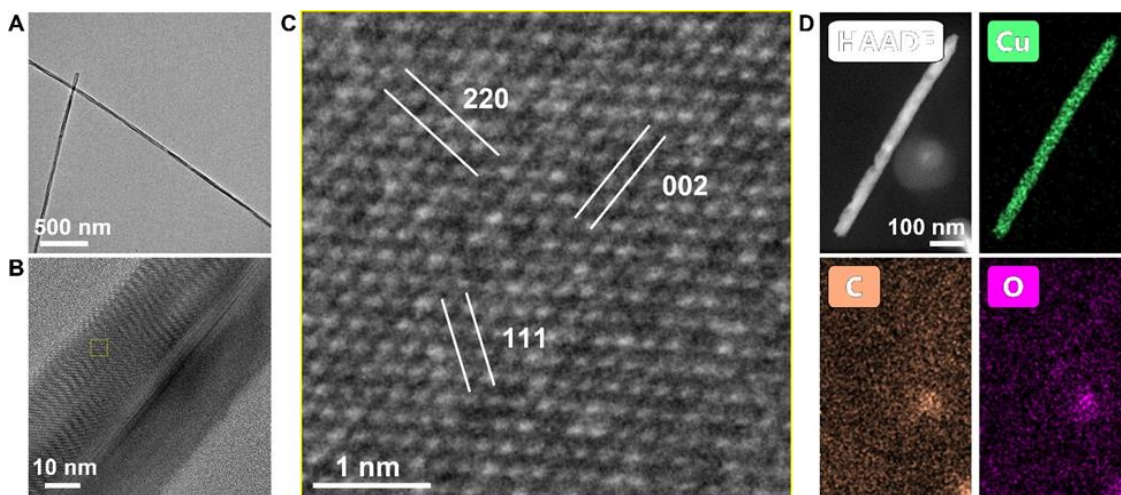


Figure 4.2 TEM characterization for the structure of the as-prepared Cu nanowires. (A) Low magnification TEM image of the Cu nanowires. (B) HRTEM image of one Cu nanowire. (C) The zoom-in image of the yellow box area in (B) shows the crystal orientation of the nanowire. (D) HADDF-STEM image of Cu nanowire and EDS elemental mapping for Cu, C and O.

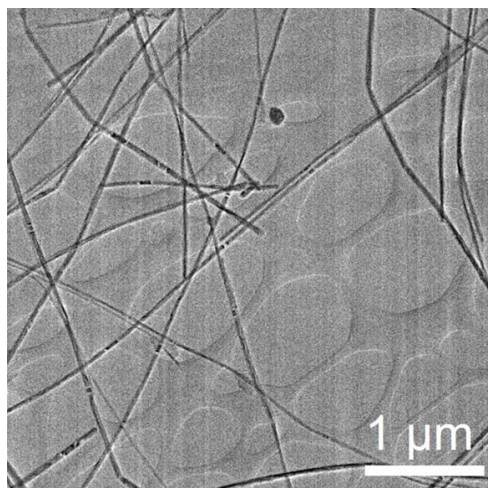


Figure 4.3 Low magnification TEM image of the Cu nanowires showing the diameter to be about 30nm.

We characterized the as-prepared copper nanowires to compare the morphology and structure of the samples before and after electrodeposition (Figure 4.2). The as-synthesized Cu nanowires have a fivefold twinned structure, typically showing $\langle 110 \rangle$ axial and $\{100\}$ radial.^{112, 129} Low-resolution TEM images show it is a one-dimensional wire structure with an average diameter of about 30 nm (Figure 4.2A and Figure 4.3). Their lengths vary from a few hundred nanometers to a few micrometers. Figure 4.2B shows a high-resolution TEM (HRTEM) image of the Cu nanowires, with the inset box magnified to be the atomic-resolution image shown in Figure 4.2C. The lattice spacings of Cu $\{111\}$, $\{002\}$ and $\{200\}$ in the figure are consistent with the case of the $\langle 110 \rangle$ axially grown Cu nanowires. Furthermore, the corresponding FFT pattern shows that Cu has a single crystal structure (Figure 4.4). The successful synthesis of copper nanowires can be confirmed from high-angle annular dark-field (HAADF)-STEM images and EDS mapping (Figure 4.2D). EDX mapping of copper (Cu), carbon (C), and oxygen (O) show the elemental distributions, proving there is no apparent oxidation of pure copper nanowires.

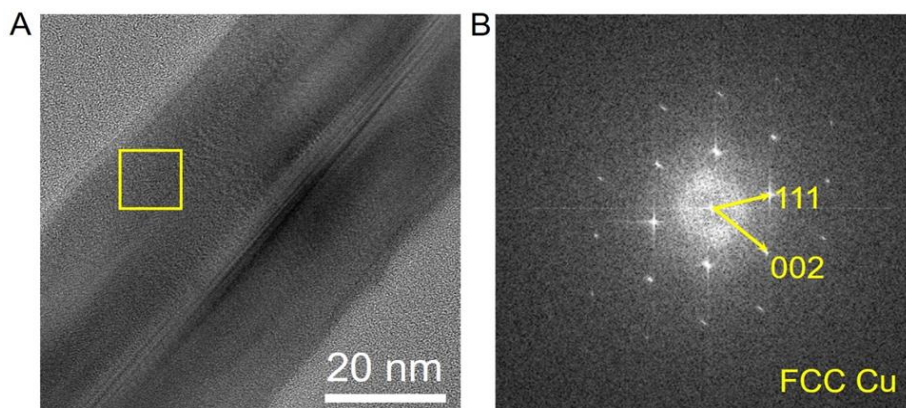


Figure 4.4 TEM and FFT pattern of the as-prepared Cu nanowire. (A) HRTEM image of one nanowire. (B) FFT pattern of as-prepared Cu nanowire in the yellow square region showing a single crystalline structure.

4.3 Structural diversity of copper particles affected by temperature

After electrodeposition, we obtained two different hierarchical nanostructures at different temperatures and named them the Cu nanoparticle/nanowire (NP/NW) hierarchical structure and nanocluster/nanowire (NC/NW) structure. As shown in Figure 4.5A, the NP/NW hierarchical structure produced by electrodeposition at room temperature (20 °C) had some individual nanoparticles attached to the nanowires. Although the average diameter of these nanoparticles is about 16 nm, they are homogeneously distributed between 10nm and 20 nm (Figure 4.6). HRTEM images indicate that these nanoparticles have good crystallinity, and the crystals can be fivefold twins and single crystals (Figure 4.5B, E). The HRTEM image and corresponding FFT pattern of the five-fold twins indicate that the twin boundaries are (111) planes (Figure 4.5C). We zoomed in on the inset box region of Figure 4.5B to better understand the interface structure between nanoparticles and nanowires. The magnified image (Figure 4.5D) shows there is almost no lattice mismatch at the interface. However, we can find a certain degree of strain at the twin boundaries, which may be caused by small changes in the lattice orientation.

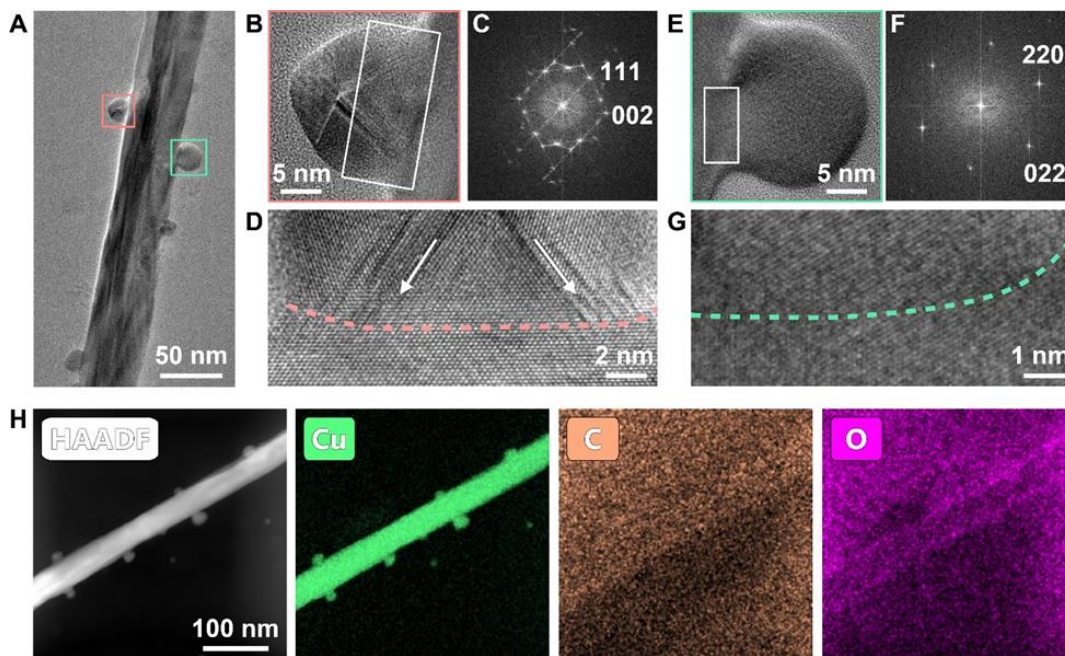


Figure 4.5 Structure characterization of the hierarchical Cu nanoparticle/nanowire nanostructure formed at room temperature (20 °C). (A) Low magnification TEM image of the hierarchical Cu NP/NW nanostructure. (B) The zoom-in image and (C) the corresponding FFT pattern of the pink box region in (A) showing the nanoparticle with a five-fold twin structure. (D) The zoom-in image of the white box area in (B) showing the interface between nanoparticles and nanowires. The pink dotted line marks out the interface. (E) The zoom-in image and (F) the corresponding FFT pattern of the green box region in (A) showing the nanoparticle with a single crystal structure. (G) The zoom-in image of the white box area in (E) showing the interface between a single crystal nanoparticle and nanowire. The green dotted line marks out the interface. (H) HAADF-STEM image of hierarchical Cu NP/NW nanostructure and EDS elemental mapping of Cu, C and O.

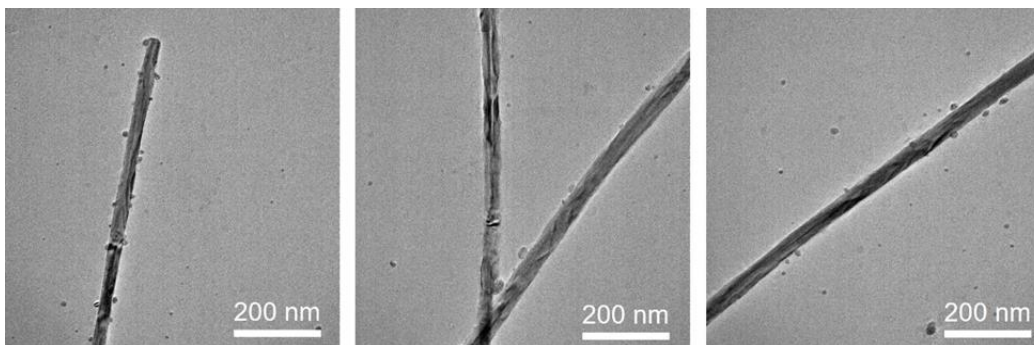


Figure 4.6 Low-resolution TEM image of the hierarchical Cu nanoparticle-nanowire nanostructure.

The shape of the single-crystal particles is close to that of a sphere. Only one set of diffraction points appears in the corresponding FFT pattern, so the crystal structures of the nanoparticle and nanowire substrate are perfectly matched (Figure 4.5F). The enlarged interface image (Figure 4.5G) further confirms a coherent interface between the nanoparticles and nanowires with no detectable differences in the lattice structure. The EDS spectrum confirmed that the particles only contain Cu element, and the C peaks came from the carbon film (Figure 4.7). Figure 4.5H shows that the copper element is uniformly distributed in the particles.

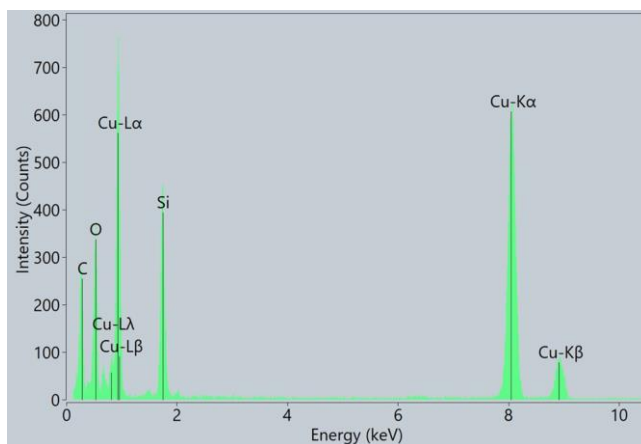


Figure 4.7 EDS spectrum of Cu nanostructures formed at room temperature (20 °C) with large crystalline Cu nanoparticles attached to the Cu nanowires.

In contrast, at -20 °C, we found that the morphology of the Cu deposits was completely different, and Cu clusters were found instead of nanoparticles (Figure 4.8A). Since copper is very active under electron beam irradiation,¹³⁰ we used low-temperature TEM imaging to avoid potential changes caused by electron beam irradiation during the imaging process. These nanoclusters are composed of smaller nanoparticles and adsorbed on nanowires to form hierarchical Cu NC/NW nanostructures.

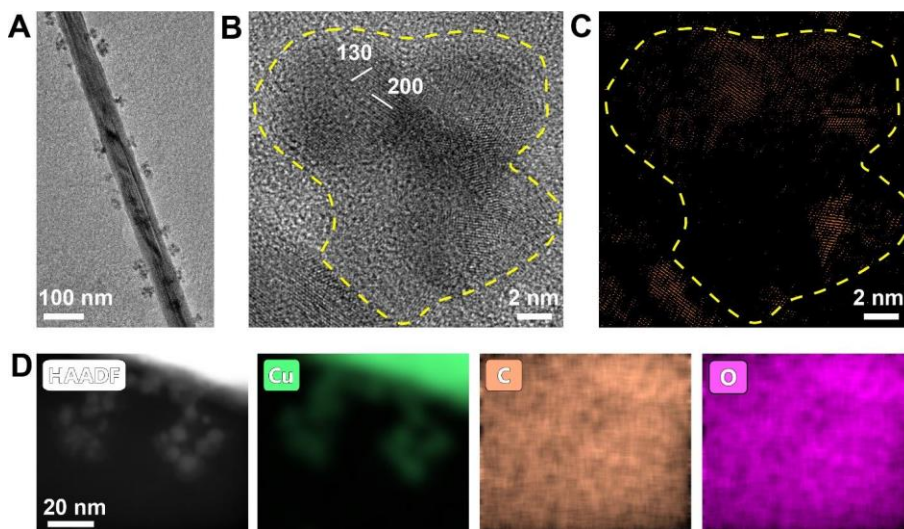


Figure 4.8 Structure characterization of the hierarchical Cu nanocluster/nanowire nanostructure formed at $-20\text{ }^{\circ}\text{C}$. (A) Low magnification TEM image of the hierarchical Cu NC/NW nanostructure. (B) HRTEM image of several gathered Cu nanoclusters showing the crystallinity of the clusters is not perfect. (C) The inverse fast Fourier transformation (IFFT) of the HRTEM image highlights the crystal part. The yellow dotted line marks the edge of the cluster. (D) HAADF-STEM of the hierarchical Cu NC/NW nanostructure and EDS elemental mapping of Cu, C, and O elements.

Compared with nanoparticles formed at room temperature, the nanoclusters have smaller diameters ($\sim 9\text{ nm}$) and greater nucleation density (Figure 4.9). The poor crystallinity of the nanoclusters can be seen from the HRTEM images (Figure 4.8B). From Figure 4.8C, it can be found that the crystalline region and the amorphous region coexist in a cluster. The crystalline parts of the clusters are highlighted by selecting diffraction points in the FFT pattern and then performing an inverse fast Fourier transformation to obtain a real-space image. Then, we stain the crystalline regions with orange. As can be seen in Figure 4.8C, the nanoparticle aggregates within the nanoclusters do not have a preferred orientation. The FFT pattern of the Cu nanoclusters also shows that the orientation of the polycrystalline Cu clusters is random (Figure 4.10). We can also speculate that their interfacial bonding is weaker from the narrow and amorphous necks between the nanoclusters and nanowires. The EDS mapping (Figure 4.8D) demonstrates that only Cu element exists in the nanoclusters. Overall, the Cu NC/NW nanostructures formed at low temperature exhibited different sizes, morphologies, crystallinity, and weaker connections to Cu nanowires compared to the NP/NW structures formed at room temperature.

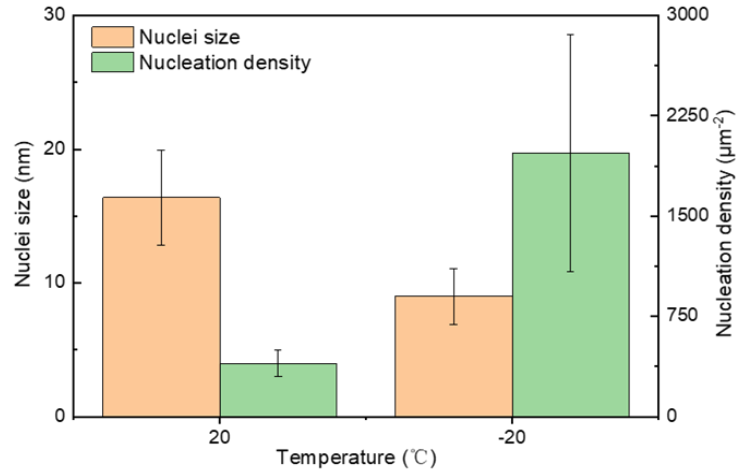


Figure 4.9 Nuclei size and nucleation density of Cu nanoparticles formed at 20 °C and -20 °C, respectively.

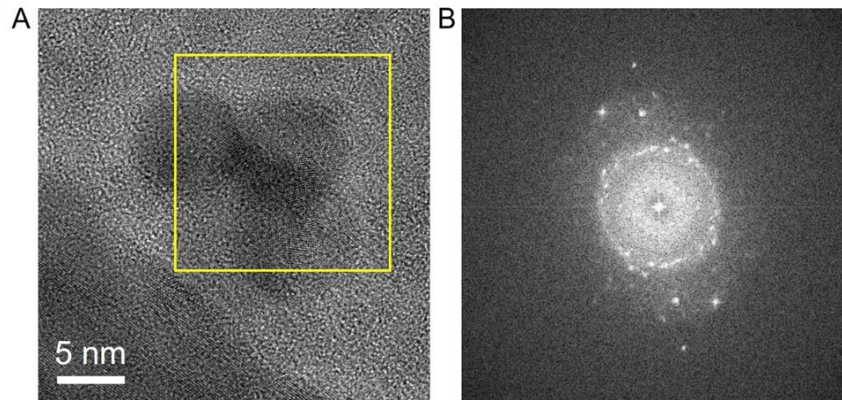


Figure 4.10 TEM image and FFT pattern of the Cu nanoclusters formed at -20 °C. (A) TEM image of the hierarchical Cu NC/NW nanostructure. (B) FFT pattern of Cu nanoclusters obtained from the yellow square area at low temperature (-20 °C). It shows random oriented polycrystalline Cu clusters.

4.4 Growth mechanism of particle growth at various temperatures

Previous studies have reported that both temperature and current density can affect the size and nucleation density of deposited particles during electrodeposition by altering the overpotential.^{123, 131} The dependence of Cu particle size on overpotential can be reflected from the classical nucleation equation. The critical radius (r_{crit}) can be described as follows:^{123, 131}

$$r_{crit} = 2YV_m/F|\eta| \quad (1)$$

Where F is Faraday's constant, Y is the surface energy of the Cu-electrolyte interface, V_m is the molar volume of Cu and η is the electrochemical overpotential. This equation can also be used to estimate the critical nucleus size in heterogeneous nucleation.^{131, 132} It can be seen from the formula that the nucleus size is inversely proportional to the electrochemical overpotential. Previous studies have demonstrated that the nucleation

overpotential increases with decreasing temperature, suggesting that lower temperatures can induce smaller metal nuclei. The current density decreases with decreasing nucleation overpotential, as predicted by the Butler-Volmer electrode kinetic relationship. Therefore, the core size becomes larger as the current density decreases. However, our experiments contradicted the predicted results with smaller nucleation size at low temperatures (Figure 4.9). Thus, we infer that the effect of temperature on the nucleation overpotential is greater than that of the current density.

We analyzed the entire process to understand differences in particle aggregation, interfacial bonding, and crystallinity. The metal electrodeposition process generally consists of three steps.^{133,134} Ions in solution first migrate to the electrode surface in the first step. After they migrate near the electrode surface, the ions undergo a chemical conversion reaction. The ions are then reduced to metal atoms. Finally, the nascent adsorbed metal atoms diffuse along the electrode surface to the growth point, contributing to the growth of the metal lattice, or aggregating with other nascent atoms to form new nuclei. Thereby multi crystals are formed. For the first step, previous studies have demonstrated that low temperatures can reduce the ion diffusion coefficient.¹³⁵ Also, it is more difficult for the electro-reduction reaction to take place at the solid-liquid interface because of the increased nucleation overpotential.¹²⁶ With regard to the third step, according to the surface diffusion theory, the diffusion coefficient D is given by:¹³⁶

$$D = \left(\nu e^{-E_{diff}/K_B T} \right) a^2 / z \quad (2)$$

Where ν is attempted frequency, T is the absolute temperature, K_B is Boltzmann constant, E_{diff} is the potential energy barrier for diffusion, and a is the distance per jump. $z=2$ for one-dimensional diffusion, $z=4$ for two-dimensional diffusion, and $z=6$ for three-dimensional diffusion. At room temperature, the diffusion of Cu ions during electrodeposition is limited by the diffusion rate. As shown in Figure 4.11A, under electrical bias, Cu ions in solution diffuse to the electrolyte/electrode interface, and then react to be reduced to Cu atoms. The nascent metal atoms diffuse along the nanowire surface and aggregate with other nascent atoms to form nanocrystals. Due to the faster surface diffusion of Cu atoms at room temperature, they can find the lowest surface energy sites to epitaxially form freestanding single-crystalline nanoparticles on the nanowires.

Although the rates of all three steps decrease at low temperatures, the decrease in reaction rate is more severe than the decrease in diffusion rate. Therefore, the whole process is reaction limited. After Cu ions diffuse to the liquid/solid interface and are reduced to adatoms, the formed adatoms cannot diffuse rapidly, resulting in a small contact area between nanoclusters and nanowires. Moreover, the subsequent ions cannot carry out the reduction reaction in time. Instead, they will accumulate on the surface of the nanoclusters, and nucleate again to form new clusters as the concentration increases. Due to the limitation of surface diffusion, nascent atoms are randomly fixed at the reaction site, resulting in poor crystallinity. This rationally explains why Cu nanoclusters are generated at sub-zero temperatures (Figure 4.11B).

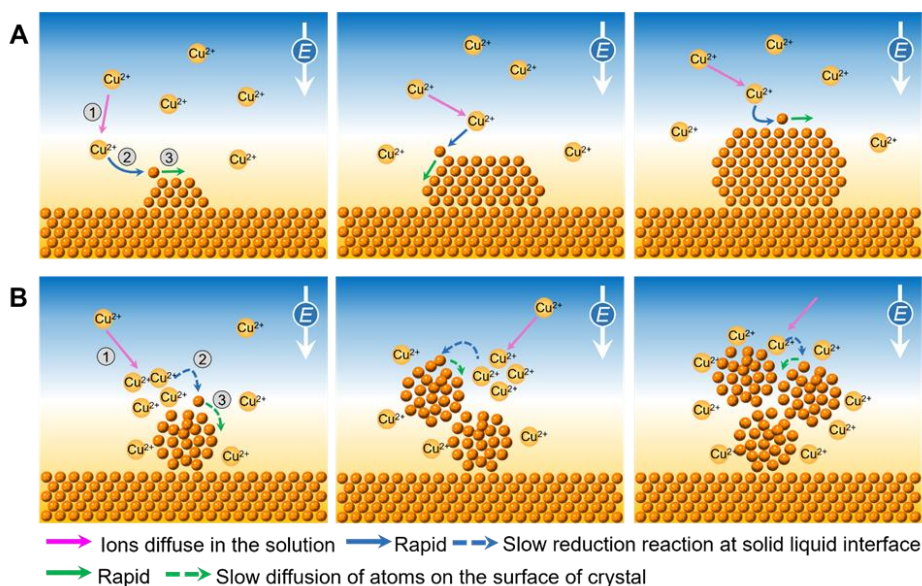


Figure 4.11 Schematic illustrations of two kinds of electrochemical growth mechanisms of Cu metal. (A) The growth of nanocrystals is limited by the diffusion of ions in the solution at room temperature. (B) The growth of nanocrystals is limited by the reduction reaction at the electrolyte/metal interface at $-20\text{ }^{\circ}\text{C}$.

Briefly, we experimentally demonstrate the temperature dependence of electrodeposited copper nanoparticles. Electrodeposition tends to produce copper clusters at subzero temperatures. The particle size, morphology, crystallinity, and connection to the substrate (Cu nanowires) are significantly different from those obtained at room temperature. The rate-limiting of the ionic reaction results in the formation of multiple nuclei and weak binding. The decrease in surface diffusion rate at low temperatures is considered to be the main factor for the generation of amorphous structures. This work deepens our understanding of nanomaterial nucleation and elucidates the factors governing metal nanoparticle electrodeposition and nanoscale dynamic processes.

5 Atomistic insights into pitting and uniform corrosion of Sn nanocrystals

5.1 Introduction to pitting and uniform corrosion

When materials interact with their environment, such as in a corrosive solution, they often experience structural degradation. Corrosion is one of the major concerns with many materials, including the destructive oxidation of metallic materials as well as the degradation of nanometallic materials, all of which lead to loss of function owing to (electro-)chemical interaction with the environment.^{137, 138} For example, electrode degradation in fuel cells,¹³⁹⁻¹⁴¹ etching of silicon in solar cell devices,¹⁴² degradation of electronic packaging,¹⁴³ structural materials breakdown,^{144, 145} have created many serious issues. Materials corrosion directly impacts the economy, and it can also lead to safety issues.^{146, 147} Unlike natural disasters (e.g., earthquake), corrosion can be controlled by improving the corrosion protection efficiency, which requires comprehensive understanding of corrosion mechanisms.¹⁴⁷

There are different types of corrosion, depending on the mechanisms of the corrosion reaction. It includes uniform, cracking, dealloying, erosion, galvanic crevice and pitting corrosion.¹⁴⁸ According to the corrosion morphology, it can be uniform corrosion, or pitting corrosion and the latter is often not easily detected.¹⁴⁹ Restrained by the available experimental methods, related studies have mostly been conducted on systems at the length scales of millimeter and micrometer.¹⁵⁰ Nevertheless, corrosion research benefits from direct observations of corrosion occurring at nano- and even atomic level to gain a clearer and more fundamental picture of corrosion behavior, such as pitting corrosion, which basically starts at an extreme small scale down to nanometers and even to atomic scale.¹⁵¹

One of the biggest challenges in the investigation of corrosion is the difficulty of observing, with atomic insight, how and where materials degrade under certain environmental conditions.¹³⁷ Many traditional electrochemical measurements, including electrochemical impedance spectroscopy, cyclic polarization and potentiodynamic polarization, have been employed to investigate the corrosion reactions. Important information, such as corrosion kinetics and resistance, can be obtained using electrochemical method.¹⁵² However, these measurements are insufficient to elucidate the underlying corrosion mechanism, and they cannot offer the ability to observe the changes of system in real-time during corrosion. In addition, the structural and morphological changes of materials caused by corrosion are typically investigated ex-situ by TEM on samples taken at different stages of reaction, which cannot give us much information about how and where corrosion will happen. Structure evolution, including specific shape and morphology changes occurring locally on individual nanocrystals at atomic scale can only be revealed using in-situ techniques with high spatial resolution.¹⁵¹ In-situ LCTEM provides capabilities for the direct observation of materials transformations in liquid environment. A variety of dynamic phenomena have been visualized with high-spatial resolution using LCTEM, including nucleation, crystallization, and dissolution.^{14, 30, 42} In-situ observations by LCTEM can provide insight into mechanisms, rates, and possible modifications of corrosion reactions in the solution environment.^{59, 60, 137, 153-156} The in-situ study of asymmetrical, strain-

induced and galvanic corrosion have been reported at nanoscale using LCTEM.^{61, 65, 157-159} The application of LCTEM to corrosion studies at the atomic level in the last several years is lacking and is urgently needed to broaden our knowledge about corrosion.

To understand the microscopic corrosion mechanism regarding how corrosion initiates and develops, metallic Sn nanocrystals and Sn nanocrystals with a protection layer, which have been widely used in electronics industry,¹⁶⁰ are employed as model systems to study pitting corrosion and uniform corrosion, respectively. Using in-situ high-resolution LCTEM, we capture the atomic-scale corrosion process of pitting corrosion and uniform corrosion. Combining with a cryo-TEM holder, aberration-corrected TEM (Cs-corrected TEM) and a fast and precise super x-ray energy-dispersive spectrometer, we could simultaneously investigate the structure and content of corrosion products in real space. Our observation reveals a facet selective etching of pitting corrosion and “creeping-like” uniform corrosion behavior. The local environment is proven to have a big impact on the corrosion behavior and kinetics.

5.2 Experimental setup and structure characterization of Sn nanocrystals with nanocoating

We take the etching process of Sn nanocrystals with nanocoating in solution as a representative system to investigate oxidative pitting corrosion. The corrosion experiments were conducted using an effective “carbon-film liquid cell” (Figure 5.1A). The carbon-film supported TEM grid was first treated with oxygen plasma to increase surficial hydrophilic that was determined by the contact angel measurements (Figure 5.2). An “in-situ” method to synthesize Sn nanocrystals with nanocoating through chemical reactions between Be, SnCl₄ and NiCl₂ within the carbon-film liquid cell is developed (Figure 5.3).

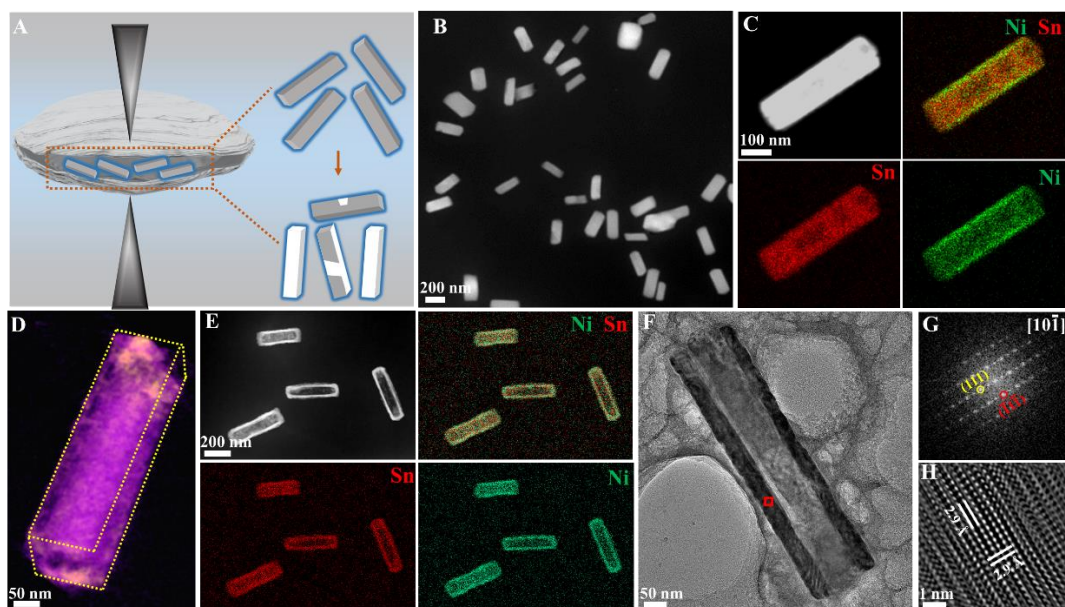


Figure 5.1 Chemical and structural characterization of Sn@Ni₃Sn₄ nanocrystal before and after corrosion in aqueous solution using a cryo-holder. (A) Schematic illustration showing the morphological evolution of a Sn@Ni₃Sn₄ nanocrystal during etching. (B) HAADF-STEM images and (C) EDS elemental mapping of Sn@ Ni₃Sn₄ nanocrystal in solution

before etching. (D) 3D reconstruction of a single nanocrystal from TEM projects, revealing an approximate rectangular prism (the dashed lines mark the rectangular prism spanned by the tips of the Sn@Ni₃Sn₄ nanocrystal). (E) HAADF-STEM image and EDS chemical maps of representative hollow nanocrystals formed after core etched. (F) Low-magnification image of the hollow nanocrystal. (G) FFT and (H) inverse FFT images from the reign enclosed in the red square in (F).

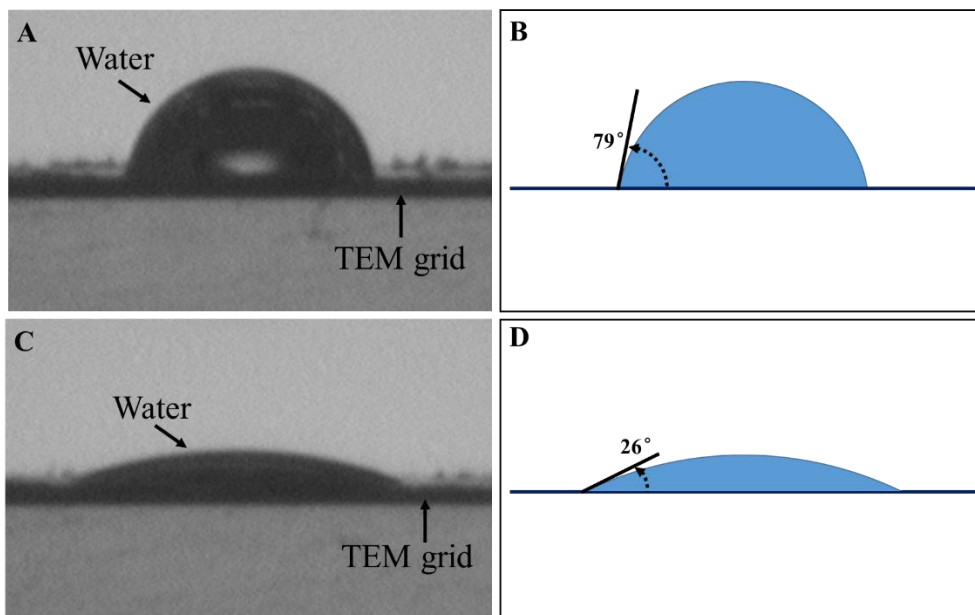


Figure 5.2 Surface classification based on contact angles. (A) Image and (B) contact angle measurement of a water droplet on a commercial TEM grid. (C) Image and (D) contact angle measurement of a water droplet on an oxygen-plasma treated TEM grid. The contact angle changes from 79° to 26° after plasma clean.

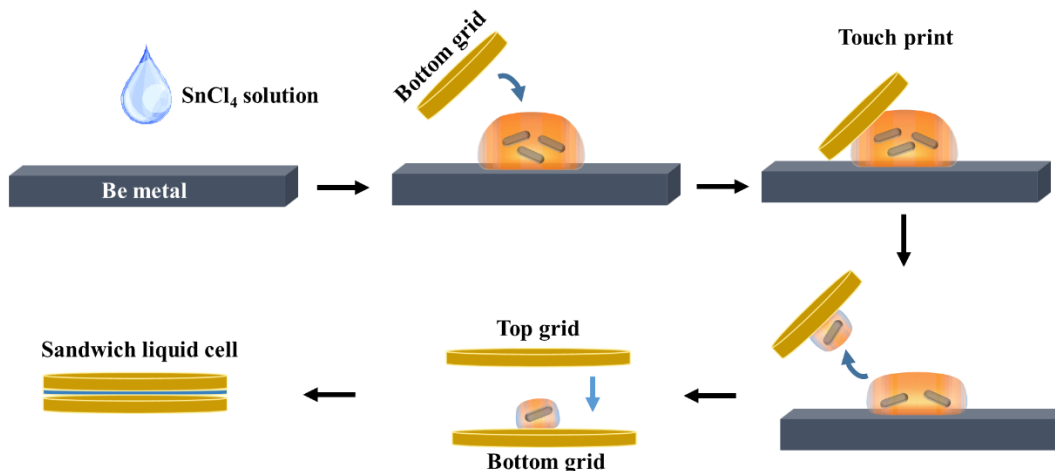


Figure 5.3 Schematic representation of the setup for the liquid cell experiment. The SnCl₄ liquid droplet is dropped on the surface of the Be metal to generate Sn nanocrystal. Touching the liquid drop with a carbon-film supported TEM grid allows transfer of the

nanocrystals in liquid. A top grid is assembled with the bottom grip to fabricate the sandwich liquid cell.

In the in/ex-situ study, an aberration-corrected TEM operated at an acceleration voltage of 300 kV is applied. HAADF-STEM image shows the nanorod morphology of the synthesized particles within the liquid cell, as shown in Figure 5.1B. Figure 5.1C displays the EDS elemental mapping of pristine Sn nanocrystals with nanocoating in solution before corrosion at liquid N₂ temperature. Elemental mapping images confirm the uniform encapsulation of the Sn core by a protective shell; Ni is abundant at the surface and surrounds the dense Sn core. Elemental maps of the chloride (Cl) and oxygen (O) from the bulk solution were also obtained (Figure 5.4). To further characterize the structure of the Sn nanocrystals with nanocoating, electron tomography is conducted, providing a 3D view of this structure. TEM images of particles at different tilting angles are shown in Figure 5.5. The 3D tomography reveals that the obtained nanocrystals are rectangular prisms, as shown in Figure 5.1D. We first investigate the oxidative corrosion of Sn nanocrystals with nanocoating in solution. This occurs because oxidizing species generated under electron-beam irradiation can trigger the oxidative etching process of Sn nanocrystals.^{13, 161}

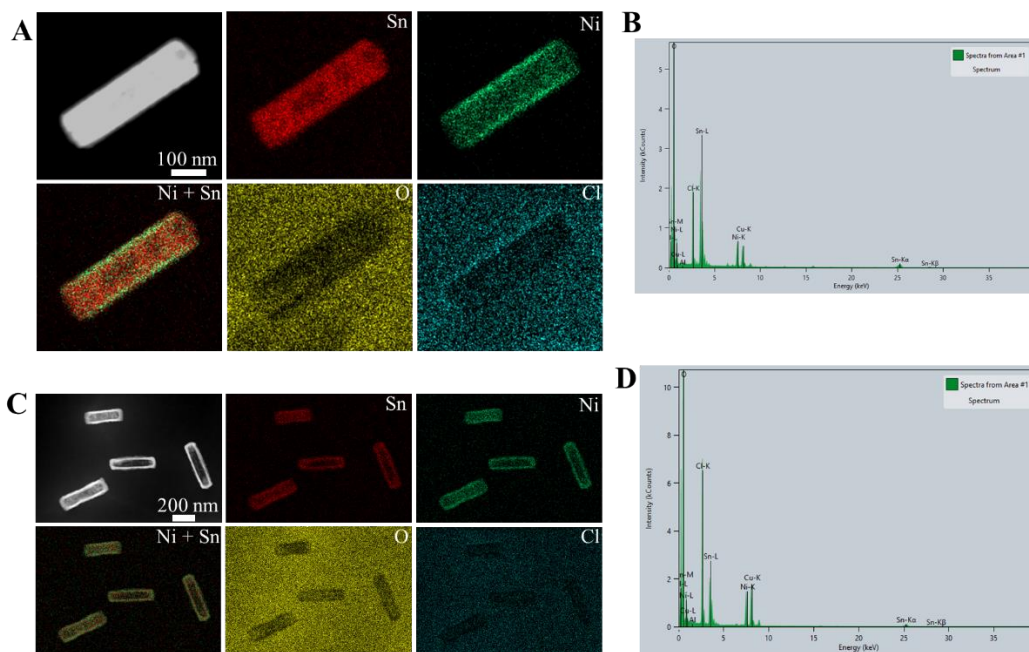


Figure 5.4 Morphology and composition characterization of Sn nanocrystals with nanocoating before and after corrosion. (A) HAADF-STEM image, EDS elements mapping of Sn, Ni, O and Cl, and (B) corresponding EDS spectrum of nanocrystals before corrosion. (C) HAADF-STEM image, EDS elements mapping of Sn, Ni, O and Cl, and (D) corresponding EDS spectrum of nanocrystals after corrosion.

Our in-situ observation reveals the transformation of the Sn with a protective shell nanomaterial into hollow nanostructure. We analyze the composition of the hollow nanocrystal that is formed after corrosion using STEM-EDS at cryo-temperature. Figure 5.1E shows representative HAADF-STEM images and corresponding elemental maps from four hollow nanocrystals in the field of view. The results indicate that the final

nanocrystal consists of Sn and Ni in the shell. We further analyze the crystalline structure of the hollow nanocrystal. Figure 5.1F shows a low-magnification TEM image of a hollow nanocrystal, and Figure 5.1G presents the FFT of the selected area in Figure 5.1F. The d-spacings of the facets measured in Figure 5.1H are consistent with the (111) and (-11-1) lattice planes of Ni_3Sn_4 crystal structure viewing along the [10-1] direction.¹⁶² From the analysis above, it is apparent that the rectangular prism nanocrystals are composed of a metal core and alloy shell. After placing the core-shell nanocrystals in an aggressive environment, the inner core will dissolve in the solution, however, the shell could keep stable for a certain time. Therefore, the $\text{Sn}@\text{Ni}_3\text{Sn}_4$ can be used as a model system for studying pitting corrosion.

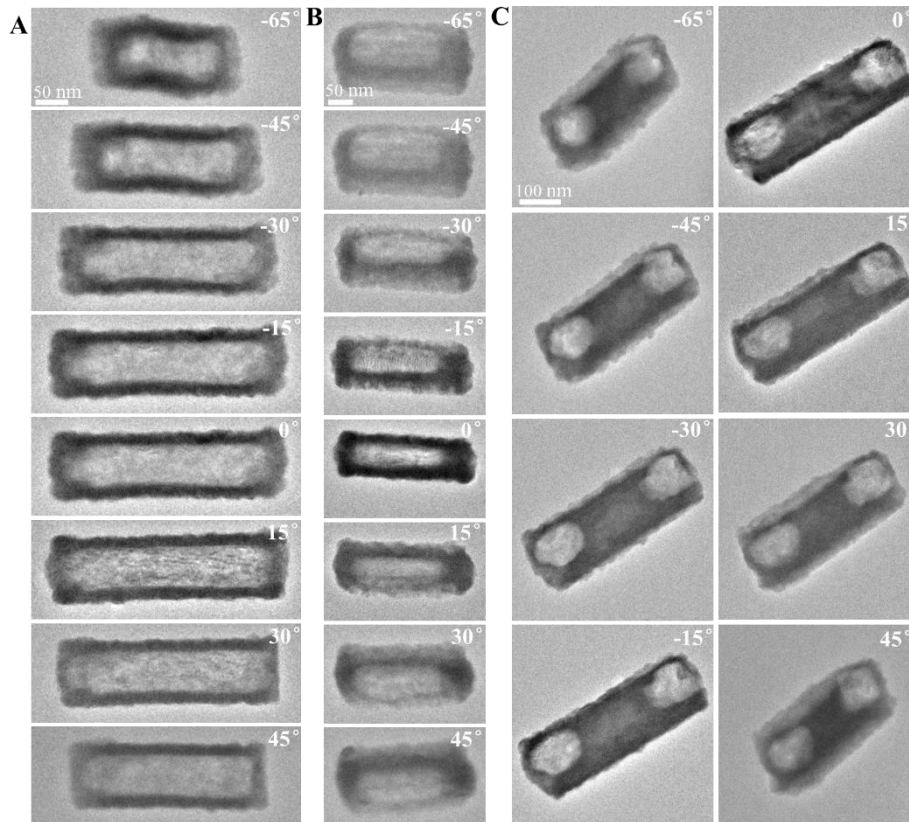


Figure 5.5 Electron tomography of Sn nanocrystals. (A-C) TEM images of different particles at different tilting angles.

5.3 Investigation of facet selective corrosion process and kinetics of $\text{Sn}@\text{Ni}_3\text{Sn}_4$ nanocrystals

Real-time observation of the corrosion process of $\text{Sn}@\text{Ni}_3\text{Sn}_4$ nanocrystals in aqueous solution is performed using LCTEM. Figure 5.6 shows the representative sequential TEM images of the morphological evolution of a regular $\text{Sn}@\text{Ni}_3\text{Sn}_4$ nanocrystal during the oxidative corrosion process. At the beginning, the $\text{Sn}@\text{Ni}_3\text{Sn}_4$ nanocrystals exhibit a well-defined rectangular prism structure. During the etching process, the contrast of the middle part of the Sn core became light, indicating that Sn was etched even with the protective shell. From the pattern of the etched area in Figure 5.6A, we can infer that there is no

selective behavior from 0 s to 32 s. As etching proceeds, an anisotropic etching creates a cavity with a trapezoidal cross-section, as shown in images at 64 s and 84 s of Figure 5.6A. Subsequently, the nanocrystal is etched along a specific facet until all the Sn metal dissolves into the solution.

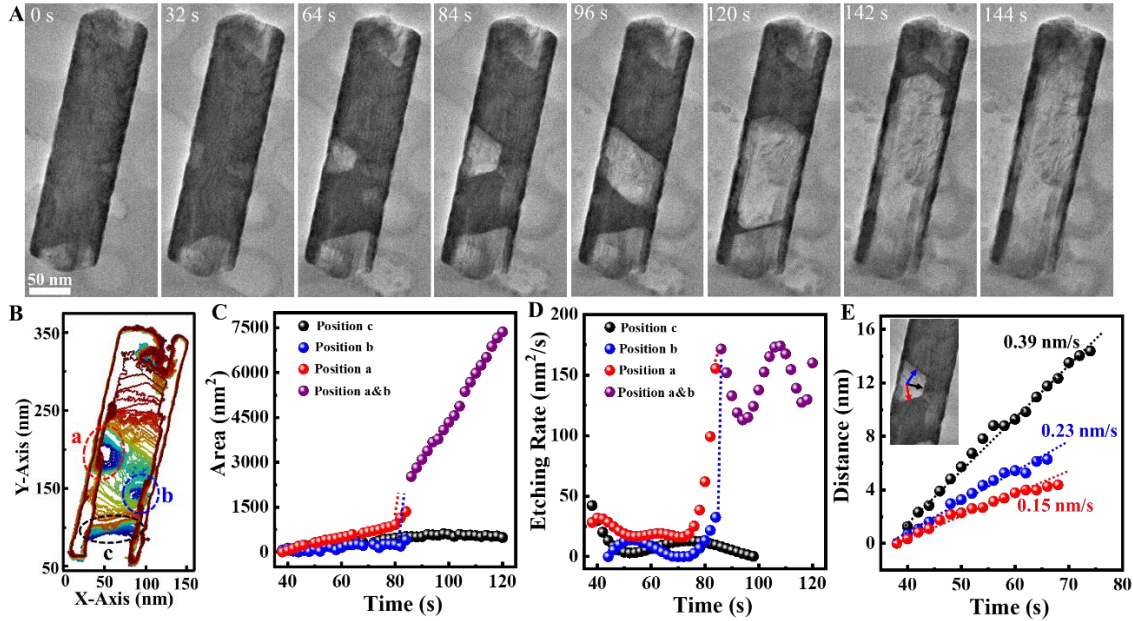


Figure 5.6 Real-time observation of the etching process of Sn@Ni₃Sn₄ nanocrystal in aqueous solution. (A) Sequential TEM images showing the etching process of a Sn@Ni₃Sn₄ nanocrystal in solution. (B) Outlines of the etching process of the Sn@Ni₃Sn₄ from each frame and overlaid to each other (position a and position b represent pitting corrosion reaction sites). The color shows a time sequence with blue as the initial time and red as the later time. (C) Etching area and (D) etching rate trajectories of Sn@Ni₃Sn₄ nanocrystal with different starting positions based on the contours in (B) (red, blue and black scatter curves show the etching area of positions a, b and c, respectively. Purple scattered curve represents the etching area after the overlapping of position a and b). (E) The etching rate of different facets. The red, blue and black curves represent the etching distance versus time along the corresponding arrow direction of the left corner image in (E). The slope rates of 0.15, 0.23 and 0.39 nm/s represent the corresponding etching rates along red, blue and black arrow directions, respectively.

To better understand the spatiotemporal details of the pitting corrosion, we constructed time-domain contour plots: cross-sectional outline of a changing nanocrystal extracted from videos that are equally spaced in time (Figure 5.6B). From Figure 5.6B, we know that there are three main reaction sites, namely positions a, b and c. Positions a and b represent the reaction sites of close structure (surface with protection layer), and position c represents the reaction site of open structure (surface without protection layer). Although the contact area of the Sn metal with the solution is small at positions a and b due to the protection layer, the etched area is very large starting from positions a and b (Figure 5.6C). The etched area is 1353, 405 and 519 nm² at 84 s for positions a, b and c, respectively. After 84 s, the etched regions from points a and b merged (Figure 5.6A). As can be seen in Figure 5.6D,

the etching rate increased sharply after the coalescence of pitting corrosion regions. We calculated that the total etched area is about 7300 nm² from the close structure (positions a and b), which is 13 times higher than the etched region from the open structure (position c). Besides the etching area and etching rate from different reaction sites, the contour of the particle shape also allows doing quantitative analysis for the facet selective etching. We measured one angle of the trapezoidal cross-section at 84 s in Figure 5.6A, which matches very well with the angle between (0-11) and (020) facets (Figure 5.7). So, we infer that the black, blue and red arrows indicate the facets of (020), (011) and (01-1) based on the symmetry structure of Sn metal viewing along [100] direction. As can be seen in Figure 5.6E, the facet etching rate of (020) is faster than the facets of (011) and (01-1). The results of the linear fit show that the etching rates of (020), (011) and (01-1) are 0.39, 0.23 and 0.15 nm/s, respectively. Therefore, the etched area is terminated with facets {011} after 96 s, which have the lowest corrosion rate, as shown in Figure 5.6A.

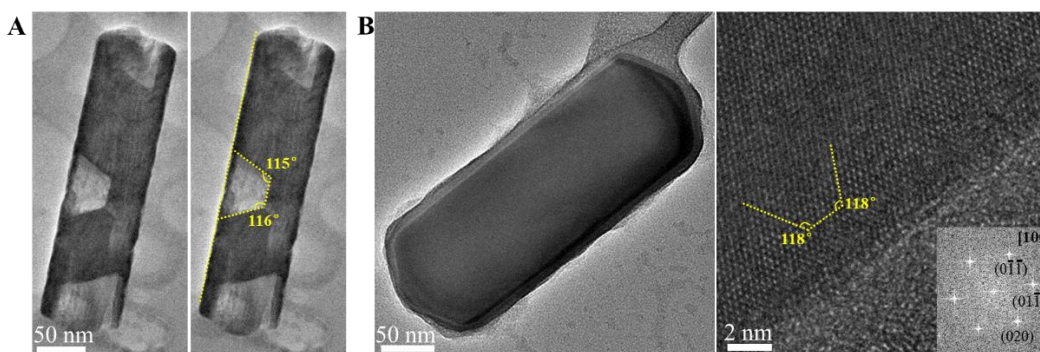


Figure 5.7 Facet determination according to the etched morphology. (A) Representative TEM images of the Sn intermediate during the pitting corrosion process. The angle between different facets is measured. (B) Low- and high-magnification TEM images of Sn nanorod.

5.4 Atomistic observation of the oxidative pitting corrosion of Sn@Ni₃Sn₄ nanocrystal

From the low-magnification real-time observation, we understand that although the initial pitting corrosion area is small, the etched area is very large. Important facet selective etching information is also obtained from the analysis of images and shape contour. However, it is still not clear where the reaction starts and how anisotropic etching occurs. To further understand the pitting etching sites and dynamics, the corrosion process of Sn@Ni₃Sn₄ nanorods was investigated. Sequential band-pass filter TEM images in Figure 5.8A show the high-resolution of pitting corrosion process of Sn@Ni₃Sn₄ nanocrystal in solution (original images are shown in Figure 5.9). There are two reaction sites during the pitting etching process, labeled as a and b at 0.6 s in Figure 5.8A. The etching reaction starts from the defective region, where the protection layer is lacking, as shown at position b in Figure 5.8A. As the corrosion area gets larger, the protective layer will crack due to the loss of support, as indicated by the blue arrow at 29.6 s in Figure 5.8A. The etching reaction from point a in Figure 5.8A shows that the pitting process includes two stages, as shown in Figure 5.8B. Firstly, isotropic etching occurred first to form a semicircular cavity structure. Then, surface atoms of the semicircular cavity structure with high activity are

removed first, resulting in surface structure terminated with low index facets. We also find that regions with a dense protection layer will not be etched under the same environment (Figure 5.10).

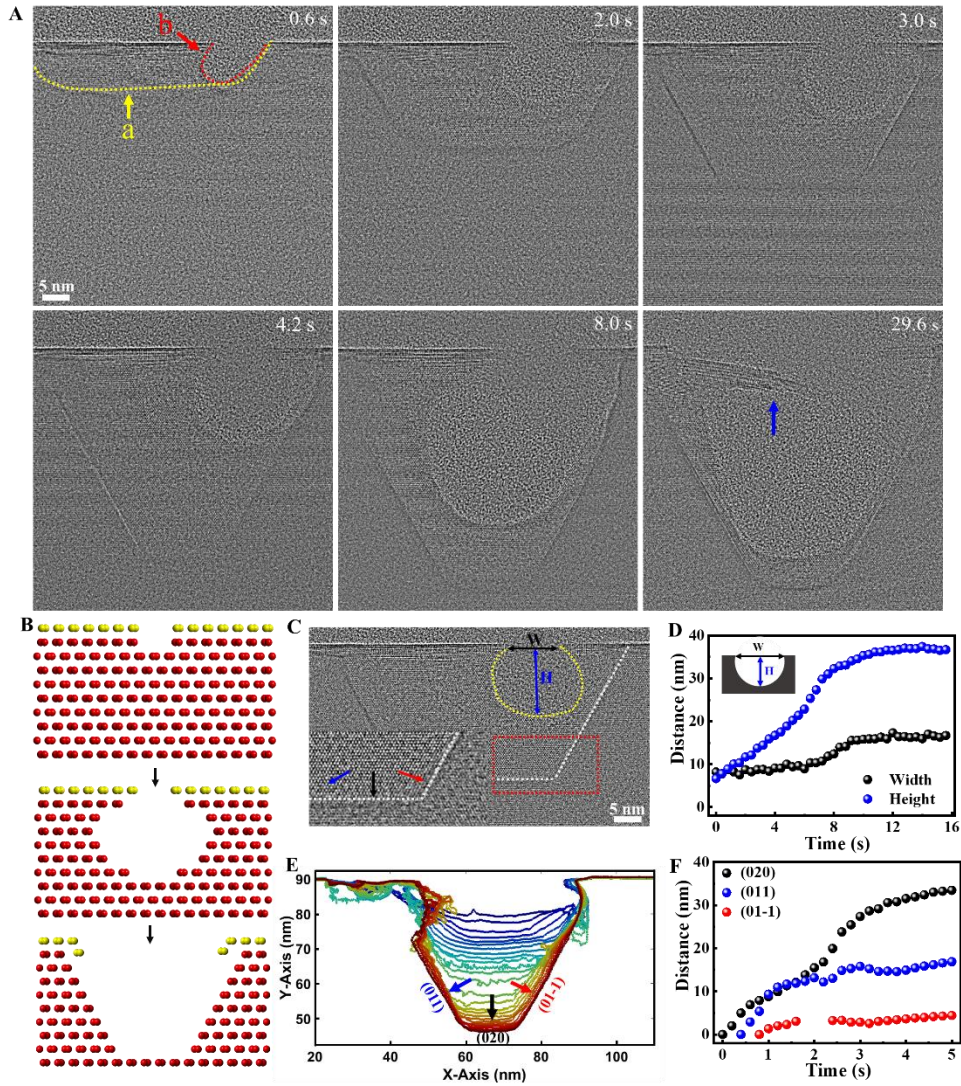


Figure 5.8 High-resolution real-time observation of the oxidative pitting corrosion process of Sn@Ni₃Sn₄ nanocrystal in aqueous solution. (A) Sequential high-resolution TEM imaging after band-pass filter treatment showing pitting oxidative etching process of Sn@Ni₃Sn₄ nanocrystal in solution with atomic-scale resolution. (B) Schematic illustration of the etching process. The golden layer represents the alloy protection layer, and the red models represent Sn metal. (C) Representative high-resolution TEM image to show the selective facet etching behavior. The inset image is the close-up view of the red square region. Black, blue and red arrows show etching directions along (020), (011) and (01-1), respectively. The etching void was indicated by the yellow dash line (W means the opening width of the hole, and H means the height from the surface of the particle to the bottom of the void). (D) Plot of the width and height versus time of the etching area, which is labeled by the yellow dash line in (C). (E) Outlines of the facet selective etching process from each frame and overlaid to each other. The color shows a time sequence with blue as

the initial time and red as the later time. (F) Etching rate of different facets based on the contours in (E).

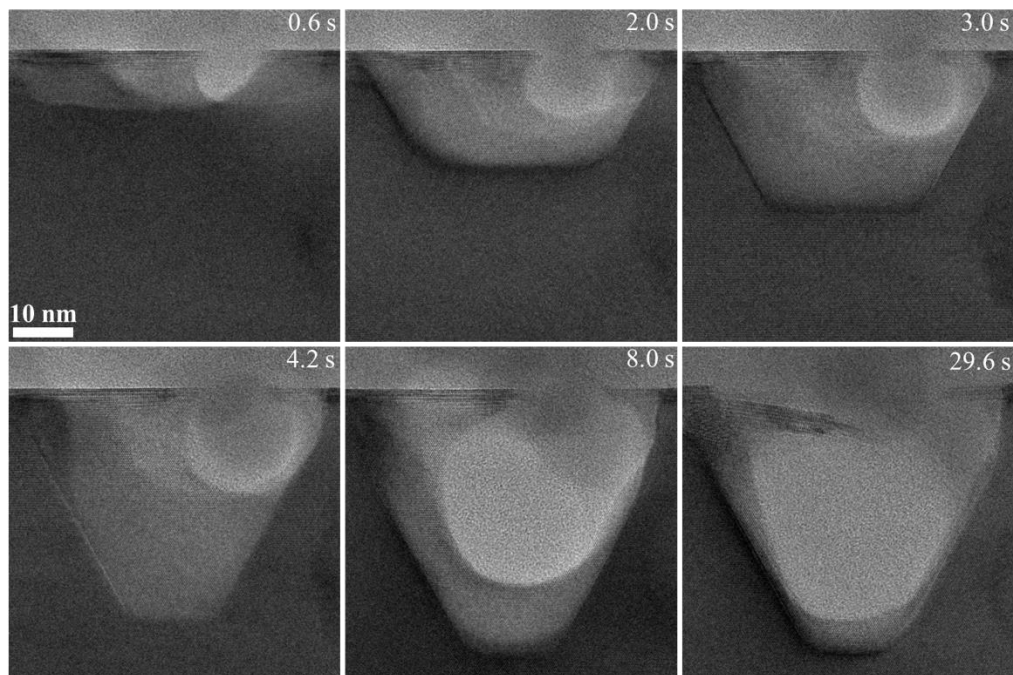


Figure 5.9 Original TEM image sequence showing pitting oxidative etching process of Sn@Ni₃Sn₄ nanocrystal in solution.

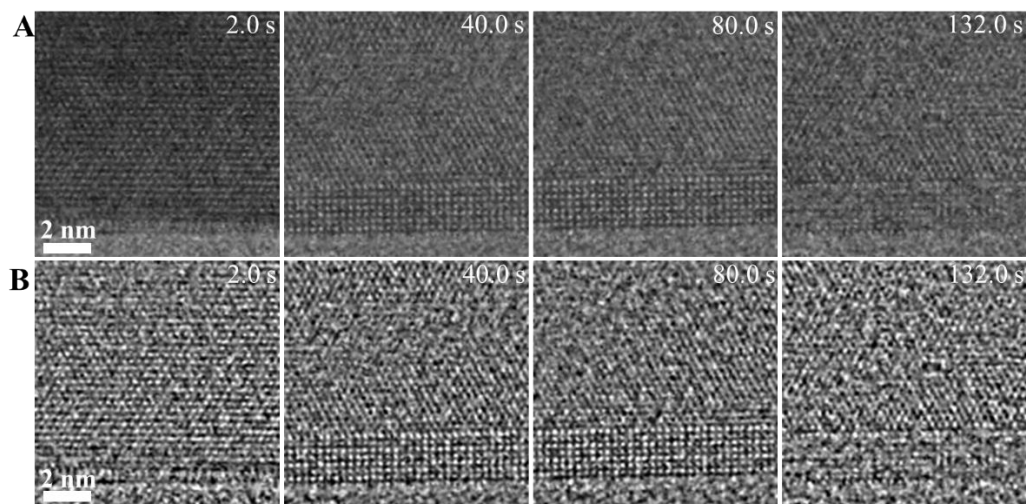


Figure 5.10 Sequential TEM images showing no corrosion reaction occurs where the protective layer is intact. (A) Selected original key frames and (B) after band-pass filter treatment.

The high-resolution TEM image in Figure 5.8C shows that the surface facets are terminated with (020), (011) and (01-1), which are indicated by the black, blue and red arrows, respectively. We measured the width and height of the hole versus the time that was created from position b, as shown in Figure 5.8D. The initial defective region without a protection

layer is about 8 nm. The width and height of the etched holes increase simultaneously from 0 s to 10 s, and then the etching rate decreases after the close-packed structure is formed on the surface. The shape contour of the etched area from position a was performed to track the facet selective etching behavior (Figure 5.8E). The facet (020) etching rate is faster than facets (011) and (01-1), which is consistent with our observation at low magnification (Figure 5.8E). It is interesting to note that the etching rate of all three facets is fast at first and then slows down at high magnification (Figure 5.8F). This could relate to the slow diffusion rate of the oxidation species that was caused by the limited pitting region. It is worthy to note that there may be no facet selective corrosion behavior of Sn@Ni₃Sn₄ crystal under the same condition (Figure 5.11), which we will discuss later. Moreover, we find that the Sn metal first dissolves into the solution, followed by the dissolution of the protective layer, as indicated by the yellow square in Figure 5.11.

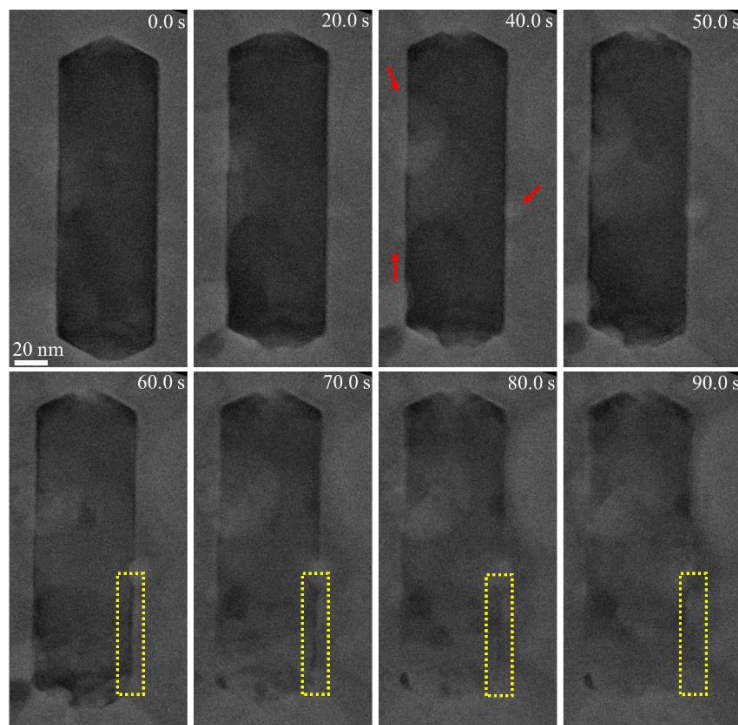


Figure 5.11 Sequential TEM images showing a galvanic corrosion process of Sn@Ni₃Sn₄ nanocrystal in aqueous solution. The Sn core first dissolves into the solution, followed by the dissolution of the alloy layer.

5.5 High-resolution real-time observation of the oxidative uniform corrosion of Sn nanocrystal

To further understand the oxidation corrosion kinetics and behaviors, we also investigate the corrosion process of metallic Sn nanocrystals in solution using LCTEM. Sn nanocrystals are synthesized using the same method as Sn@Ni₃Sn₄ nanocrystals. Besides metallic Sn nanocrystals, we also extend this method to synthesize Cu nanoparticles through the chemical reaction between Zn and Cu(NO₃)₂ solution (Figure 5.12).

Sn nanocrystals display different morphologies, and the main ones are nanorods, as shown in Figure 5.13. We first characterize the frozen metallic Sn sample in solution with a Super EDS before corrosion at liquid N₂ temperature. EDS mapping shows that there is no additional oxygen signal on the surface of Sn nanocrystal, which indicates that there is no tin oxide layer on the surface (Figure 5.13). While the Sn nanocrystals synthesized ex-situ shows an obvious oxide layer after several rounds of centrifugation and washing (Figure 5.14). The above results confirm that our synthesis method could efficiently prevent Sn nanocrystals from being oxidized.

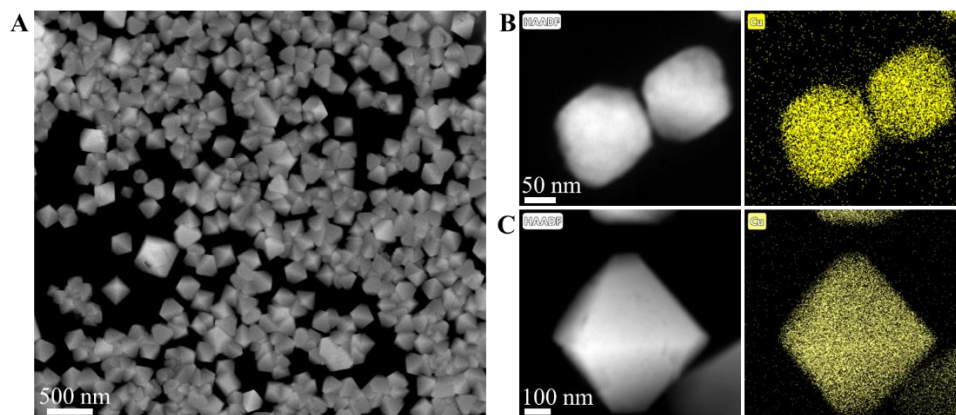


Figure 5.12 Structure characterization of Cu nanocrystals. (A) Low- and (B-C) high-magnification HAADF-STEM images and corresponding EDS mapping of Cu nanocrystals.

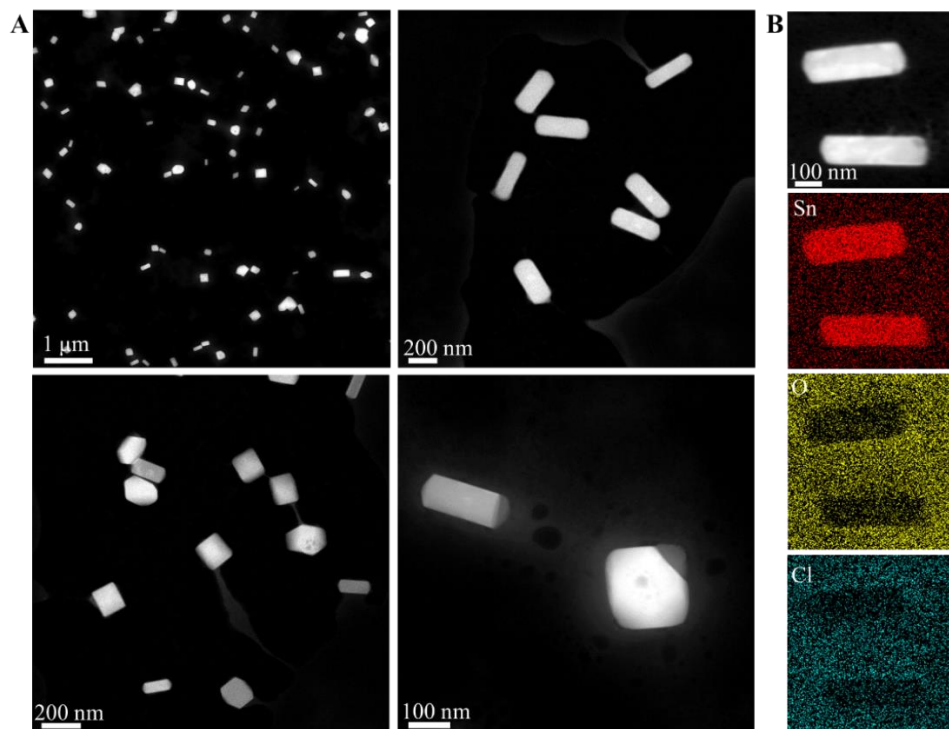


Figure 5.13 Structure characterization of Sn nanocrystal within liquid cell by cryo-EM. (A) HAADF-STEM images of Sn nanocrystal. (B) HAADF-STEM images of Sn nanocrystal and corresponding elemental mapping of Sn, O, and Cl. Different morphologies of Sn nanocrystal are observed, and no oxidation layer is detected on the surface of Sn nanocrystal.

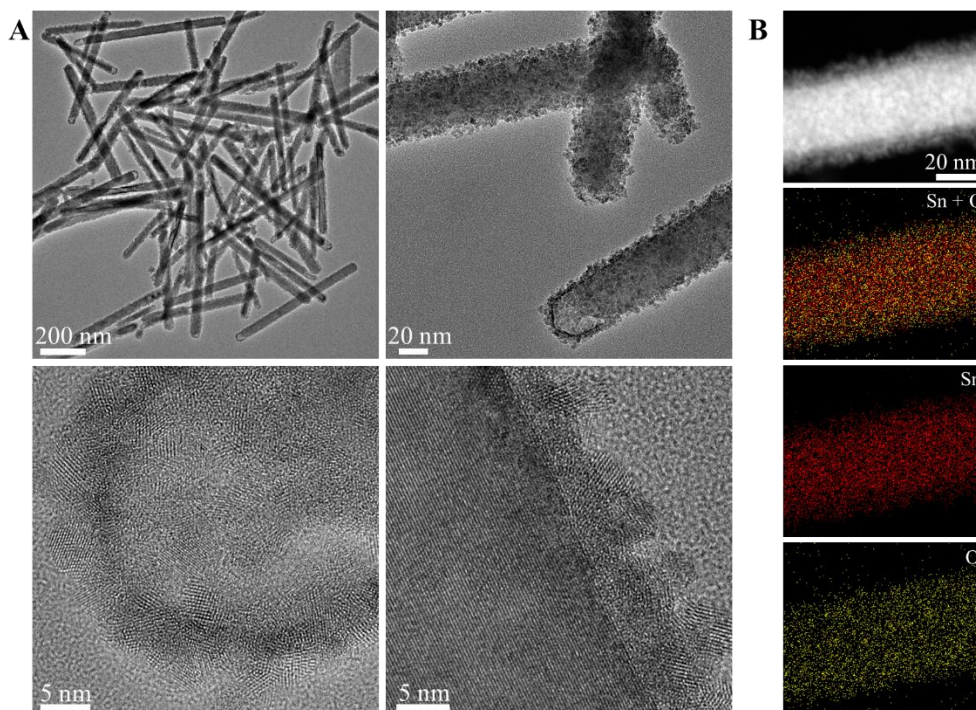


Figure 5.14 Structure characterization of Sn nanocrystal synthesized ex-situ. (A) Low- and high-magnification TEM images of Sn nanorods. The high-resolution image indicates that the polycrystalline SnO₂ layer is formed on the surface of Sn nanorod. (B) EDS elements mapping of Sn, O to confirm the existence of surface oxidation layer.

We first select a Sn nanocrystal that is adsorbed on the viewing window, and the liquid layer around this nanocrystal is thin, which can be distinguished from the contrast of the solution background. Some very interesting intermediates were found during the etching process. As can be seen from Figure 5.15A, a diffusion layer was formed on the surface of the Sn nanocrystal. We observed that the thickness of the diffusion layer increases as the Sn etching progresses until the entire viewing area is filled. The higher contrast of the diffusion layer than the background of the solution further confirms the existence of Sn-ions in the diffusion layer. Besides the diffusion layer, a “creeping-like” etching behavior (Figure 5.15B, C) was also observed due to the slow reaction kinetics in the thin liquid region and the adhesive force between the Sn nanocrystal and the membrane. Using in-situ HRTEM, we observe that Sn nanocrystals behaved like a liquid droplet but remain highly crystalline in the interior. The “creeping-like” etching behaviors start from the position with high curvature (Figure 5.15B).

We also investigate the etching behaviors of a “free” Sn nanocrystal in solution, as shown in Figure 5.15D. These free Sn nanocrystals are observed in the regions with a thick liquid layer. We notice that there is no surface diffusion layer on the surface of the Sn nanocrystal in thick liquid layer region during the etching process. The etching rate of the pure Sn metal is fast, and it takes less than 5 s to make the Sn nanocrystal dissolve into the solution. Moreover, compared with the etching behaviors of the Sn nanocrystal with a protection layer, the facet selective etching behavior for metallic Sn nanocrystals is not observed.

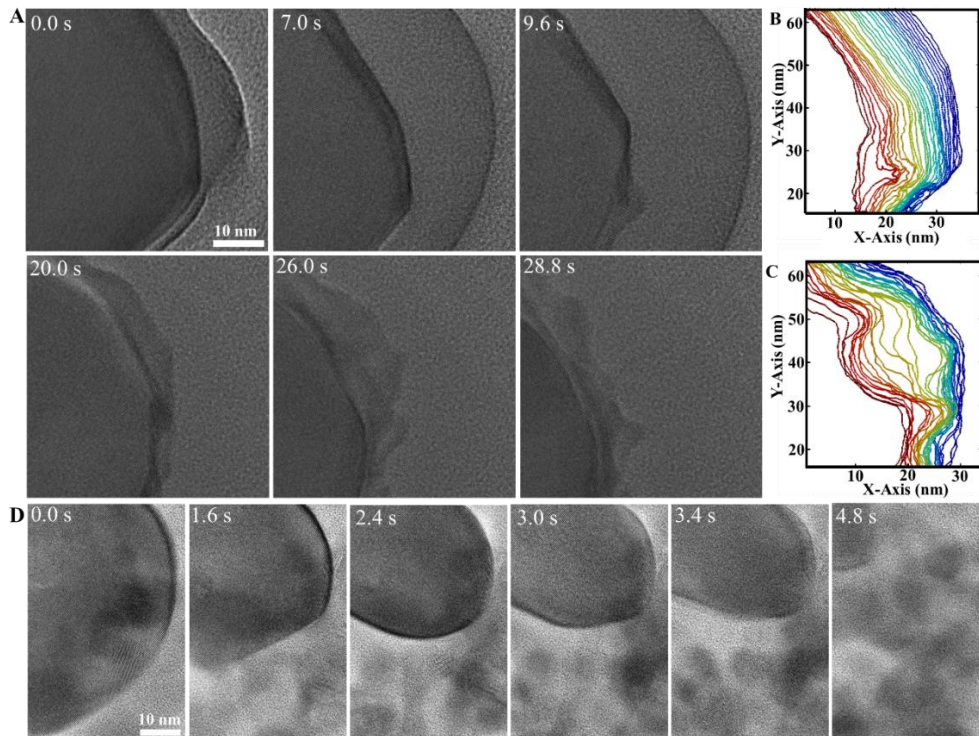
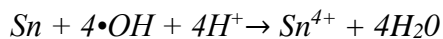


Figure 5.15 High-resolution real-time observation of the oxidative etching process of Sn nanocrystal in solution. (A) Sequential high-resolution TEM imaging showing oxidative etching process of Sn nanocrystal attached to the window in a thin region. (B) Outline of the early etching process (0.0 s – 13.8 s) and (C) late etching process (20.0 s – 33.0 s) of the Sn nanocrystal. The color shows time sequence with blue as the initial time and red as the later time. (D) Sequential TEM images showing the etching process of free Sn nanocrystal in a thick region.

5.6 Discussion on the mechanism of pitting and uniform corrosion

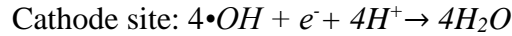
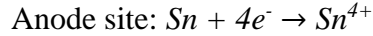
Oxidative etching is a common reaction during the corrosion process. In this work, we use LCTEM to investigate the oxidative etching behavior of core-shell Sn@Ni₃Sn₄ and metallic Sn nanocrystals in solution, which represent pitting and uniform corrosion, respectively. The oxidative etching reactions are triggered by the oxidation species generated by the electron beam irradiation. Within microsecond after irradiation, a steady state is reached with hydroxide radicals ($\bullet\text{OH}$), hydrogen peroxide (H_2O_2), hydrogen ion (H^+) etc. being the dominant species.¹³ To simplify the reaction, we use hydroxide radicals to represent the oxidation species. Therefore, the metallic Sn nanocrystals corrosion reaction can be described as follows:



For the uniform corrosion behavior in the thin liquid layer, Sn nanocrystals undergo dissolution and Sn-ions are formed and diffuse into the bulk solution. The diffusion rate of Sn-ions is slow due to the thin thickness of the surrounding liquid layer, so the surface diffusion layer was captured. The absence of a diffusion layer during the corrosion process in the thick liquid layer can be caused by the following two reasons. 1) The thickness of

the liquid layer is too thick, and the diffusion layer cannot be observed. 2) The diffusion kinetics of Sn-ions are too fast to be captured in the thick region.

The corrosion reaction of the Sn core of the Sn@Ni₃Sn₄ nanocrystal is a little different because of the existence of the alloy layer. Besides the chemical reaction with the oxidation species directly, Sn core also undergoes a galvanic corrosion process. The Sn core works as anode, and the alloy layer works as cathode. Therefore, we observed that Sn first dissolves into the solution, followed by the dissolution of the alloy layer (Figure 5.11). The Sn core corrosion reaction can be described as follows:



After Sn core is removed, the alloy layer will be oxidized into Ni-ion and Sn-ion through the chemical reaction with oxidative species in solution.

We infer that the pitting corrosion behavior is controlled by the concentration of oxidation etching species and Sn-ions within the pitting region. At the beginning of the corrosion, different crystal faces are exposed where there is no protection layer. Sn core is quickly oxidized and dissolved into the solution by adjacent irradiation oxidation species, so the concentration of oxidation species within the cavity decreases and the concentration of Sn-ions increases. Due to the small hole size of the initial pitting position, the diffusion rate of oxidation species from outside the cavity into the cavity is relatively low. The Sn-ions are also trapped into the pitting region. Both the chemical and electrochemical corrosion processes are suppressed. The reduced reaction kinetics allows the Sn nanocrystal to reach an equilibrium state during the corrosion process, which facets are terminated with low index facets. We also notice that there is no equilibrium state if many bubbles are formed near the particle region, as indicated by the red arrows in Figure 5.11. We hypothesize that these bubbles can influence the reaction kinetics through the following ways: 1) the bubble contains high concentration of oxidation species, which will react with the Sn-core; 2) the bubble pushes the flow of the thin liquid layer to increase the diffusion of oxidation species through the small hole. Above all, the local environment has a big influence on the reaction kinetics and shape evolution of the Sn nanocrystals during the corrosion process.

In summary, our in-situ liquid cell imaging in combination with other complementary electron microscopy techniques, such as, aberration-corrected high-resolution imaging, EDS mapping and cryo-EM characterization of the liquids near the solid surface provides an unprecedented level of details on corrosion. The pitting and uniform corrosion process of non-precious metals with atomic resolution is achieved in a liquid environment. Details including facet selective etching, passive layer failure, surface diffusion layer and creeping-like behaviors are revealed. Facet selective corrosion behavior of Sn@Ni₃Sn₄ caused by the slow diffusion of oxidation species during the pitting corrosion. Our results prove that LC-TEM provides for observation and microscopic understanding of transient intermediates in the etching of nanocrystals. This work provides atomistic insights into the pitting and uniform corrosion behaviors and etching dynamics of nanocrystals in solution, offering an important design principle for engineering protection layers of nanocrystals to achieve corrosion-resistant materials.

6 Future Perspectives

We consider it necessary to integrate the development of low-temperature techniques with the electrochemical liquid cell capabilities, which would enable the in-situ high-resolution study of SEI or other electron beam-sensitive materials. We designed a novel holder by adding the electric biasing capability to the current cryogenic holder. Coupled with an electrochemical liquid cell, this setup would allow for the studies of electrochemical processes with liquid electrolytes both in-situ and at various low temperatures.

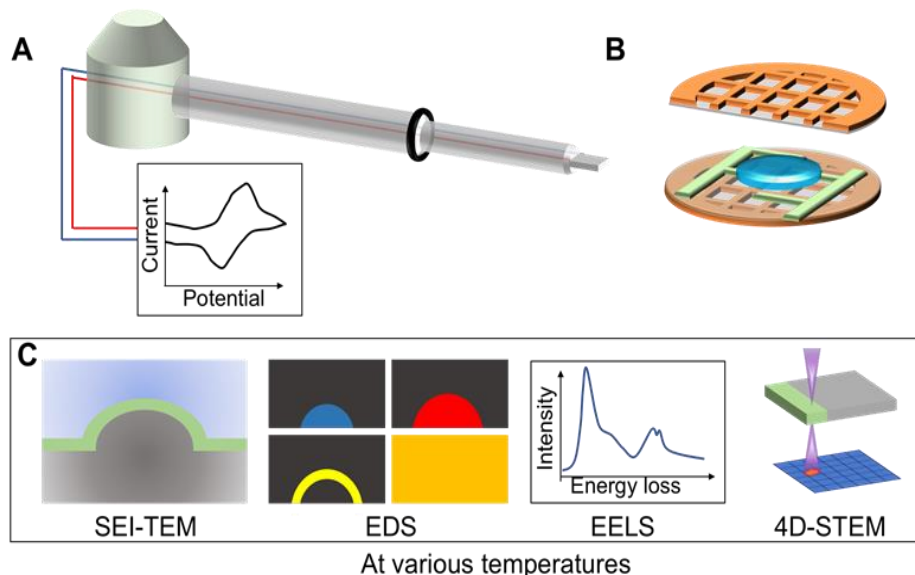


Figure 6.1 Design of novel electrochemical liquid cell setup allowing to study electrochemical processes with liquid electrolyte in-situ at various temperatures. (A-B) A schematic of the experimental setup by developing the electrochemical liquid cell with variable temperature control. (C) The capability of this setup, such as TEM imaging, EDS and EELS and 4D-STEM at various temperatures.

Polyimide is selected as the support film in consideration of its high chemical resistance, less sensitive to the electron beam, and high mechanical stability. Preliminary work shows that polyimide thin film can be successfully transferred onto the TEM grid using HF as the transferring solution. This support film is thin and uniform enough for high-resolution imaging and as the liquid cell membrane. The major steps of the process flow have been achieved, indicating the feasibility of fabricating this unique type of liquid cell.

The development of this new electrochemical liquid cell setup allowing various low temperatures has enabled the exploration of scientific phenomena that previously are unreachable. An electric bias can be applied to the sample and the nanoscale structural evolution, such as the SEI structure and composition (distribution of organic and inorganic components) during cycling, and the electrodeposition of metal or alloy nanoparticles. The growth mechanisms (e.g., growth mode, preferred growth direction) of Li dendrites in different environments (e.g., electrolyte component, temperature, current density) can also be revealed in this setup. This interesting setup would allow transferring the sample onto a

cryogenic holder for further characterization without having to open the cell. Thus, it avoids exposure of the sample to air or moisture, thus limiting damages or structural alternations of the samples.

In summary, the research and development included in this document exemplify LCTEM can be used to study materials transformations at the atomic level, which is hard to achieve with another approach. The experiments can be extended to various temperatures. The success in the design and fabrication of nanoscale devices opens many future opportunities for the investigation of nanostructure dynamics at the atomic scale as well as air-sensitive functional materials in-situ.

References

1. Reetz, M. T.; Helbig, W.; Quaiser, S. A.; Stimming, U.; Breuer, N.; Vogel, R., Visualization of surfactants on nanostructured palladium clusters by a combination of STM and high-resolution TEM. *Science* **1995**, *267* (5196), 367-369.
2. Lisiecki, I.; Filankembo, A.; Sack-Kongehl, H.; Weiss, K.; Pileni, M.-P.; Urban, J., Structural investigations of copper nanorods by high-resolution TEM. *Phys. Rev. B* **2000**, *61* (7), 4968.
3. Leng, Y., *Materials characterization: introduction to microscopic and spectroscopic methods*. John Wiley & Sons: 2009.
4. Kimoto, K.; Asaka, T.; Nagai, T.; Saito, M.; Matsui, Y.; Ishizuka, K., Element-selective imaging of atomic columns in a crystal using STEM and EELS. *Nature* **2007**, *450* (7170), 702-704.
5. Li, Y.; Li, Y.; Pei, A.; Yan, K.; Sun, Y.; Wu, C. L.; Joubert, L. M.; Chin, R.; Koh, A. L.; Yu, Y.; Perrino, J.; Butz, B.; Chu, S.; Cui, Y., Atomic structure of sensitive battery materials and interfaces revealed by cryo-electron microscopy. *Science* **2017**, *358* (6362), 506-510.
6. Abakumov, A. M.; Fedotov, S. S.; Antipov, E. V.; Tarascon, J.-M., Solid state chemistry for developing better metal-ion batteries. *Nat. Commun.* **2020**, *11* (1), 1-14.
7. Haider, M.; Uhlemann, S.; Schwan, E.; Rose, H.; Kabius, B.; Urban, K., Electron microscopy image enhanced. *Nature* **1998**, *392* (6678), 768-769.
8. Batson, P. E.; Dellby, N.; Krivanek, O. L., Sub-ångstrom resolution using aberration corrected electron optics. *Nature* **2002**, *418* (6898), 617-620.
9. Erni, R.; Rossell, M. D.; Kisielowski, C.; Dahmen, U., Atomic-resolution imaging with a sub-50-pm electron probe. *Phys. Rev. Lett.* **2009**, *102* (9), 096101.
10. Sawada, H.; Tanishiro, Y.; Ohashi, N.; Tomita, T.; Hosokawa, F.; Kaneyama, T.; Kondo, Y.; Takayanagi, K., STEM imaging of 47-pm-separated atomic columns by a spherical aberration-corrected electron microscope with a 300-kV cold field emission gun. *J. Electron. Microsc.* **2009**, *58* (6), 357-361.
11. Jiang, Y.; Chen, Z.; Han, Y.; Deb, P.; Gao, H.; Xie, S.; Purohit, P.; Tate, M. W.; Park, J.; Gruner, S. M., Electron ptychography of 2D materials to deep sub-ångström resolution. *Nature* **2018**, *559* (7714), 343-349.
12. Chen, Z.; Jiang, Y.; Shao, Y.-T.; Holtz, M. E.; Odstrčil, M.; Guizar-Sicairos, M.; Hanke, I.; Ganschow, S.; Schlom, D. G.; Muller, D. A., Electron ptychography achieves atomic-resolution limits set by lattice vibrations. *Science* **2021**, *372* (6544), 826-831.
13. Schneider, N. M.; Norton, M. M.; Mendel, B. J.; Grogan, J. M.; Ross, F. M.; Bau, H. H., Electron–Water Interactions and Implications for Liquid Cell Electron Microscopy. *The Journal of Physical Chemistry C* **2014**, *118* (38), 22373-22382.
14. Ross, F. M., Opportunities and challenges in liquid cell electron microscopy. *Science* **2015**, *350* (6267), aaa9886.
15. Liao, H.-G.; Zheng, H., Liquid cell transmission electron microscopy. *Annu. Rev. Phys. Chem.* **2016**, *67*, 719-747.
16. Schneider, N. M., Electron beam effects in liquid cell TEM and STEM. In *liquid cell electron microscopy*; Ross, F. M.; Cambridge University Press; **2016**, 140-163.
17. Donets, E. D., Historical review of electron beam ion sources. *Rev. Sci. Instrum.* **1998**, *69* (2), 614-619.
18. Zheng, H.; Meng, Y. S.; Zhu, Y., Frontiers of electron microscopy. *Mrs. Bull.* **2015**, *40* (1), 12-18.
19. Marton, L., La microscopie électronique des objets biologiques. *Bull. Acad. Roy. Med. Belg.* **1935**, *21*, 600-617.

20. Abrams, I.; McBain, J., A closed cell for electron microscopy. *J. Appl. Phys.* **1944**, *15* (8), 607-609.
21. Williamson, M. J.; Tromp, R. M.; Vereecken, P. M.; Hull, R.; Ross, F. M., Dynamic microscopy of nanoscale cluster growth at the solid-liquid interface. *Nat. Mater.* **2003**, *2* (8), 532-6.
22. Zheng, H.; Smith, R. K.; Jun, Y.-w.; Kisielowski, C.; Dahmen, U.; Alivisatos, A. P., Observation of single colloidal platinum nanocrystal growth trajectories. *Science* **2009**, *324* (5932), 1309-1312.
23. de Jonge, N.; Peckys, D. B.; Kremers, G. J.; Piston, D. W., Electron microscopy of whole cells in liquid with nanometer resolution. *Proc. Natl. Acad. Sci. USA* **2009**, *106* (7), 2159-64.
24. Huang, J. Y.; Zhong, L.; Wang, C. M.; Sullivan, J. P.; Xu, W.; Zhang, L. Q.; Mao, S. X.; Hudak, N. S.; Liu, X. H.; Subramanian, A., In situ observation of the electrochemical lithiation of a single SnO₂ nanowire electrode. *Science* **2010**, *330* (6010), 1515-1520.
25. Yuk, J. M.; Park, J.; Ercius, P.; Kim, K.; Hellebusch, D. J.; Crommie, M. F.; Lee, J. Y.; Zettl, A.; Alivisatos, A. P., High-resolution EM of colloidal nanocrystal growth using graphene liquid cells. *Science* **2012**, *336* (6077), 61-64.
26. Liao, H.-G.; Cui, L.; Whitlam, S.; Zheng, H., Real-time imaging of Pt₃Fe nanorod growth in solution. *Science* **2012**, *336* (6084), 1011-1014.
27. Li, D.; Nielsen, M. H.; Lee, J. R.; Frandsen, C.; Banfield, J. F.; De Yoreo, J. J., Direction-specific interactions control crystal growth by oriented attachment. *Science* **2012**, *336* (6084), 1014-8.
28. Nielsen, M. H.; Aloni, S.; De Yoreo, J. J., In situ TEM imaging of CaCO₃ nucleation reveals coexistence of direct and indirect pathways. *Science* **2014**, *345* (6201), 1158-1162.
29. Zeng, Z.; Zhang, X.; Bustillo, K.; Niu, K.; Gammer, C.; Xu, J.; Zheng, H., In situ study of lithiation and delithiation of MoS₂ nanosheets using electrochemical liquid cell transmission electron microscopy. *Nano Lett.* **2015**, *15* (8), 5214-5220.
30. Ye, X.; Jones, M. R.; Frechette, L. B.; Chen, Q.; Powers, A. S.; Ercius, P.; Dunn, G.; Rotskoff, G. M.; Nguyen, S. C.; Adiga, V. P., Single-particle mapping of nonequilibrium nanocrystal transformations. *Science* **2016**, *354* (6314), 874-877.
31. Ross, F. M., *Liquid Cell Electron Microscopy*. Cambridge University Press: 2016.
32. Schreiber, R. E.; Houben, L.; Wolf, S. G.; Leitus, G.; Lang, Z. L.; Carbo, J. J.; Poblet, J. M.; Neumann, R., Real-time molecular scale observation of crystal formation. *Nat. Chem.* **2017**, *9* (4), 369-373.
33. Yang, J.; Zeng, Z.; Kang, J.; Betzler, S.; Czarnik, C.; Zhang, X.; Ophus, C.; Yu, C.; Bustillo, K.; Pan, M.; Qiu, J.; Wang, L. W.; Zheng, H., Formation of two-dimensional transition metal oxide nanosheets with nanoparticles as intermediates. *Nat. Mater.* **2019**, *18* (9), 970-976.
34. Wang, Y.; Peng, X.; Abelson, A.; Xiao, P.; Qian, C.; Yu, L.; Ophus, C.; Ercius, P.; Wang, L. W.; Law, M.; Zheng, H., Dynamic deformability of individual PbSe nanocrystals during superlattice phase transitions. *Sci. Adv.* **2019**, *5* (6), eaaw5623.
35. Sutter, E.; Sutter, P.; Tkachenko, A. V.; Krahn, R.; de Graaf, J.; Arciniegas, M.; Manna, L., In situ microscopy of the self-assembly of branched nanocrystals in solution. *Nat. Commun.* **2016**, *7*, 11213.
36. Hauwiler, M. R.; Ondry, J. C.; Alivisatos, A. P., Using graphene liquid cell transmission electron microscopy to study in situ nanocrystal etching. *J. Vis. Exp.* **2018**, (135).
37. Yang, J.; Choi, M. K.; Sheng, Y.; Jung, J.; Bustillo, K.; Chen, T.; Lee, S. W.; Ercius, P.; Kim, J. H.; Warner, J. H.; Chan, E. M.; Zheng, H., MoS₂ liquid cell electron microscopy through clean and fast polymer-free MoS₂ transfer. *Nano Lett.* **2019**, *19* (3), 1788-1795.
38. Hauwiler, M. R.; Ondry, J. C.; Chan, C. M.; Khandekar, P.; Yu, J.; Alivisatos, A. P., Gold nanocrystal etching as a means of probing the dynamic chemical environment in graphene liquid cell electron microscopy. *J. Am. Chem. Soc.* **2019**, *141* (10), 4428-4437.

39. Zhu, C.; Liang, S.; Song, E.; Zhou, Y.; Wang, W.; Shan, F.; Shi, Y.; Hao, C.; Yin, K.; Zhang, T., In-situ liquid cell transmission electron microscopy investigation on oriented attachment of gold nanoparticles. *Nat. Commun.* **2018**, *9* (1), 1-7.
40. Peckys, D. B.; de Jonge, N., Visualizing gold nanoparticle uptake in live cells with liquid scanning transmission electron microscopy. *Nano Lett.* **2011**, *11* (4), 1733-1738.
41. Fu, X.; Chen, B.; Tang, J.; Hassan, M. T.; Zewail, A. H., Imaging rotational dynamics of nanoparticles in liquid by 4D electron microscopy. *Science* **2017**, *355* (6324), 494-498.
42. Liao, H.-G.; Zherebetsky, D.; Xin, H.; Czarnik, C.; Ercius, P.; Elmlund, H.; Pan, M.; Wang, L.-W.; Zheng, H., Facet development during platinum nanocube growth. *Science* **2014**, *345* (6199), 916-919.
43. Park, J.; Elmlund, H.; Ercius, P.; Yuk, J. M.; Limmer, D. T.; Chen, Q.; Kim, K.; Han, S. H.; Weitz, D. A.; Zettl, A., 3D structure of individual nanocrystals in solution by electron microscopy. *Science* **2015**, *349* (6245), 290-295.
44. Kim, B. H.; Heo, J.; Kim, S.; Reboul, C. F.; Chun, H.; Kang, D.; Bae, H.; Hyun, H.; Lim, J.; Lee, H., Critical differences in 3D atomic structure of individual ligand-protected nanocrystals in solution. *Science* **2020**, *368* (6486), 60-67.
45. Jeon, S.; Heo, T.; Hwang, S.-Y.; Ciston, J.; Bustillo, K. C.; Reed, B. W.; Ham, J.; Kang, S.; Kim, S.; Lim, J., Reversible disorder-order transitions in atomic crystal nucleation. *Science* **2021**, *371* (6528), 498-503.
46. Lu, Y.; Yin, W. J.; Peng, K. L.; Wang, K.; Hu, Q.; Selloni, A.; Chen, F. R.; Liu, L. M.; Sui, M. L., Self-hydrogenated shell promoting photocatalytic H₂ evolution on anatase TiO₂. *Nat. Commun.* **2018**, *9* (1), 2752.
47. Liu, Y.; Lin, X.-M.; Sun, Y.; Rajh, T., In situ visualization of self-assembly of charged gold nanoparticles. *J. Am. Chem. Soc.* **2013**, *135* (10), 3764-3767.
48. Ou, Z.; Wang, Z.; Luo, B.; Luijten, E.; Chen, Q., Kinetic pathways of crystallization at the nanoscale. *Nat. Mater.* **2020**, *19* (4), 450-455.
49. Alloyeau, D.; Dachraoui, W.; Javed, Y.; Belkahla, H.; Wang, G.; Lecoq, H.; Ammar, S.; Ersen, O.; Wisnet, A.; Gazeau, F.; Ricolleau, C., Unravelling kinetic and thermodynamic effects on the growth of gold nanoplates by liquid transmission electron microscopy. *Nano Lett.* **2015**, *15* (4), 2574-81.
50. Hansen, P. L.; Wagner, J. B.; Helveg, S.; Rostrup-Nielsen, J. R.; Clausen, B. S.; Topsøe, H., Atom-resolved imaging of dynamic shape changes in supported copper nanocrystals. *Science* **2002**, *295* (5562), 2053-2055.
51. Ringe, E.; Van Duyne, R. P.; Marks, L., Wulff construction for alloy nanoparticles. *Nano Lett.* **2011**, *11* (8), 3399-3403.
52. Gibbs, J. W. *The collected works of J. Willard Gibbs*; Yale Univ. Press: 1948.
53. Wulff, G., Xxv. zur frage der geschwindigkeit des wachstums und der auflösung der krystallflächen. *Z Krist-Cryst Mater* **1901**, *34* (1-6), 449-530.
54. Loh, N. D.; Sen, S.; Bosman, M.; Tan, S. F.; Zhong, J.; Nijhuis, C. A.; Kral, P.; Matsudaira, P.; Mirsaidov, U., Multistep nucleation of nanocrystals in aqueous solution. *Nat. Chem.* **2017**, *9* (1), 77-82.
55. De Yoreo, J. J.; Gilbert, P. U.; Sommerdijk, N. A.; Penn, R. L.; Whitlam, S.; Joester, D.; Zhang, H.; Rimer, J. D.; Navrotsky, A.; Banfield, J. F.; Wallace, A. F.; Michel, F. M.; Meldrum, F. C.; Colfen, H.; Dove, P. M., CRYSTAL GROWTH. Crystallization by particle attachment in synthetic, biogenic, and geologic environments. *Science* **2015**, *349* (6247), aaa6760.
56. Yang, J.; Koo, J.; Kim, S.; Jeon, S.; Choi, B. K.; Kwon, S.; Kim, J.; Kim, B. H.; Lee, W. C.; Lee, W. B.; Lee, H.; Hyeon, T.; Ercius, P.; Park, J., Amorphous-phase-mediated crystallization of Ni nanocrystals revealed by high-resolution liquid-phase electron microscopy. *J. Am. Chem. Soc.* **2019**, *141*(2), 763-768.

57. Patterson, J. P.; Abellan, P.; Denny, M. S., Jr.; Park, C.; Browning, N. D.; Cohen, S. M.; Evans, J. E.; Gianneschi, N. C., Observing the growth of metal-organic frameworks by in situ liquid cell transmission electron microscopy. *J. Am. Chem. Soc.* **2015**, *137* (23), 7322-8.
58. Jungjohann, K.; Bliznakov, S.; Sutter, P.; Stach, E.; Sutter, E., In situ liquid cell electron microscopy of the solution growth of Au–Pd core–shell nanostructures. *Nano Lett.* **2013**, *13* (6), 2964-2970.
59. Sun, M.; Tian, J.; Chen, Q., The studies on wet chemical etching via in situ liquid cell TEM. *Ultramicroscopy* **2021**, *231*, 113271.
60. Kosari, A.; Zandbergen, H.; Tichelaar, F.; Visser, P.; Terryn, H.; Mol, A., Application of in situ liquid cell transmission Electron microscopy in corrosion studies: a critical review of challenges and achievements. *Corrosion* **2020**, *76* (1), 4-17.
61. Shi, F.; Gao, W.; Shan, H.; Li, F.; Xiong, Y.; Peng, J.; Xiang, Q.; Chen, W.; Tao, P.; Song, C.; Shang, W.; Deng, T.; Zhu, H.; Zhang, H.; Yang, D.; Pan, X.; Wu, J., Strain-Induced Corrosion Kinetics at Nanoscale Are Revealed in Liquid: Enabling Control of Corrosion Dynamics of Electrocatalysis. *Chem* **2020**, *6* (9), 2257-2271.
62. Chen, L.; Leonardi, A.; Chen, J.; Cao, M.; Li, N.; Su, D.; Zhang, Q.; Engel, M.; Ye, X., Imaging the kinetics of anisotropic dissolution of bimetallic core-shell nanocubes using graphene liquid cells. *Nat. Commun.* **2020**, *11* (1), 3041.
63. Wu, J.; Gao, W.; Yang, H.; Zuo, J. M., Dissolution Kinetics of Oxidative Etching of Cubic and Icosahedral Platinum Nanoparticles Revealed by in Situ Liquid Transmission Electron Microscopy. *ACS Nano* **2017**, *11* (2), 1696-1703.
64. Jiang, Y.; Zhu, G.; Lin, F.; Zhang, H.; Jin, C.; Yuan, J.; Yang, D.; Zhang, Z., In situ study of oxidative etching of palladium nanocrystals by liquid cell electron microscopy. *Nano Lett.* **2014**, *14* (7), 3761-5.
65. Shan, H.; Gao, W.; Xiong, Y.; Shi, F.; Yan, Y.; Ma, Y.; Shang, W.; Tao, P.; Song, C.; Deng, T.; Zhang, H.; Yang, D.; Pan, X.; Wu, J., Nanoscale kinetics of asymmetrical corrosion in core-shell nanoparticles. *Nat. Commun.* **2018**, *9* (1), 1011.
66. Chee, S. W.; Tan, S. F.; Baraissov, Z.; Bosman, M.; Mirsaidov, U., Direct observation of the nanoscale Kirkendall effect during galvanic replacement reactions. *Nat. Commun.* **2017**, *8* (1), 1224.
67. Mehdi, B. L.; Qian, J.; Nasybulin, E.; Park, C.; Welch, D. A.; Faller, R.; Mehta, H.; Henderson, W. A.; Xu, W.; Wang, C. M.; Evans, J. E.; Liu, J.; Zhang, J. G.; Mueller, K. T.; Browning, N. D., Observation and quantification of nanoscale processes in lithium batteries by operando electrochemical (S)TEM. *Nano Lett.* **2015**, *15* (3), 2168-73.
68. Zeng, Z.; Liang, W.-I.; Liao, H.-G.; Xin, H. L.; Chu, Y.-H.; Zheng, H., Visualization of electrode–electrolyte interfaces in LiPF₆/EC/DEC electrolyte for lithium ion batteries via in situ TEM. *Nano Lett.* **2014**, *14* (4), 1745-1750.
69. Zeng, Z.; Barai, P.; Lee, S.-Y.; Yang, J.; Zhang, X.; Zheng, W.; Liu, Y.-S.; Bustillo, K. C.; Ercius, P.; Guo, J., Electrode roughness dependent electrodeposition of sodium at the nanoscale. *Nano Energy* **2020**, *72*, 104721.
70. Wu, Y. A.; Yin, Z.; Farmand, M.; Yu, Y.-S.; Shapiro, D. A.; Liao, H.-G.; Liang, W.-I.; Chu, Y.-H.; Zheng, H., In-situ multimodal imaging and spectroscopy of Mg electrodeposition at electrode–electrolyte interfaces. *Sci. Rep.* **2017**, *7* (1), 1-9.
71. Sun, M.; Liao, H.-G.; Niu, K.; Zheng, H., Structural and morphological evolution of lead dendrites during electrochemical migration. *Sci. Rep.* **2013**, *3* (1), 1-6.
72. Wu, F.; Yao, N., Advances in sealed liquid cells for in-situ TEM electrochemical investigation of lithium-ion battery. *Nano Energy* **2015**, *11*, 196-210.
73. Zeng, Z.; Zheng, W.; Zheng, H., Visualization of Colloidal Nanocrystal Formation and Electrode–Electrolyte Interfaces in Liquids Using TEM. *Acc. Chem. Res.* **2017**, *50* (8), 1808-1817.

74. Zhang, Q.; Ma, J.; Mei, L.; Liu, J.; Li, Z.; Li, J.; Zeng, Z., In situ TEM visualization of LiF nanosheet formation on the cathode-electrolyte interphase (CEI) in liquid-electrolyte lithium-ion batteries. *Matter* **2022**.
75. Lee, S.-Y.; Shangguan, J.; Alvarado, J.; Betzler, S.; Harris, S. J.; Doeff, M. M.; Zheng, H., Unveiling the mechanisms of lithium dendrite suppression by cationic polymer film induced solid-electrolyte interphase modification. *Energy & Environmental Science* **2020**, *13* (6), 1832-1842.
76. Rasool, H.; Dunn, G.; Fathalizadeh, A.; Zettl, A., Graphene-sealed Si/SiN cavities for high-resolution in situ electron microscopy of nano-confined solutions. *Phys. Status Solidi (b)* **2016**, *253* (12), 2351-2354.
77. Kelly, D. J.; Zhou, M.; Clark, N.; Hamer, M. J.; Lewis, E. A.; Rakowski, A. M.; Haigh, S. J.; Gorbachev, R. V., Nanometer Resolution Elemental Mapping in Graphene-Based TEM Liquid Cells. *Nano Lett.* **2018**, *18* (2), 1168-1174.
78. Sato, K.; Shikida, M.; Matsushima, Y.; Yamashiro, T.; Asaumi, K.; Iriye, Y.; Yamamoto, M., Characterization of orientation-dependent etching properties of single-crystal silicon: effects of KOH concentration. *Sensors and Actuators A: Physical* **1998**, *64* (1), 87-93.
79. Talmon, Y.; Davis, H. T.; Scriven, L.; Thomas, E. L., Cold-stage microscopy system for fast-frozen liquids. *Review of Scientific Instruments* **1979**, *50* (6), 698-704.
80. Wang, Q. H.; Kalantar-Zadeh, K.; Kis, A.; Coleman, J. N.; Strano, M. S., Electronics and optoelectronics of two-dimensional transition metal dichalcogenides. *Nat. Nanotechnol.* **2012**, *7* (11), 699-712.
81. Koppens, F.; Mueller, T.; Avouris, P.; Ferrari, A.; Vitiello, M.; Polini, M., Photodetectors based on graphene, other two-dimensional materials and hybrid systems. *Nat. Nanotechnol.* **2014**, *9* (10), 780-793.
82. Pomerantseva, E.; Gogotsi, Y., Two-dimensional heterostructures for energy storage. *Nature Energy* **2017**, *2* (7), 1-6.
83. Karunadasa, H. I.; Montalvo, E.; Sun, Y.; Majda, M.; Long, J. R.; Chang, C. J., A molecular MoS₂ edge site mimic for catalytic hydrogen generation. *Science* **2012**, *335* (6069), 698-702.
84. Chang, Y. H.; Lin, C. T.; Chen, T. Y.; Hsu, C. L.; Lee, Y. H.; Zhang, W.; Wei, K. H.; Li, L. J., Highly efficient electrocatalytic hydrogen production by MoS_x grown on graphene-protected 3D Ni foams. *Advanced materials* **2013**, *25* (5), 756-760.
85. Huang, B.; Clark, G.; Navarro-Moratalla, E.; Klein, D. R.; Cheng, R.; Seyler, K. L.; Zhong, D.; Schmidgall, E.; McGuire, M. A.; Cobden, D. H., Layer-dependent ferromagnetism in a van der Waals crystal down to the monolayer limit. *Nature* **2017**, *546* (7657), 270-273.
86. Chen, W.; Sun, Z.; Wang, Z.; Gu, L.; Xu, X.; Wu, S.; Gao, C., Direct observation of van der Waals stacking-dependent interlayer magnetism. *Science* **2019**, *366* (6468), 983-987.
87. Huang, B.; Clark, G.; Klein, D. R.; MacNeill, D.; Navarro-Moratalla, E.; Seyler, K. L.; Wilson, N.; McGuire, M. A.; Cobden, D. H.; Xiao, D., Electrical control of 2D magnetism in bilayer CrI₃. *Nat. Nanotechnol.* **2018**, *13* (7), 544-548.
88. Sivadas, N.; Okamoto, S.; Xu, X.; Fennie, C. J.; Xiao, D., Stacking-dependent magnetism in bilayer CrI₃. *Nano Lett.* **2018**, *18* (12), 7658-7664.
89. Fei, L.; Lei, S.; Zhang, W.-B.; Lu, W.; Lin, Z.; Lam, C. H.; Chai, Y.; Wang, Y., Direct TEM observations of growth mechanisms of two-dimensional MoS₂ flakes. *Nat. Commun.* **2016**, *7* (1), 1-7.
90. Hansen, L. P.; Johnson, E.; Brorson, M.; Helveg, S., Growth mechanism for single- and multi-layer MoS₂ nanocrystals. *J. Phys. Chem. C* **2014**, *118* (39), 22768-22773.
91. Yang, J.; Zeng, Z.; Kang, J.; Betzler, S.; Czarnik, C.; Zhang, X.; Ophus, C.; Yu, C.; Bustillo, K.; Pan, M., Formation of two-dimensional transition metal oxide nanosheets with nanoparticles as intermediates. *Nat. Mater.* **2019**, *18* (9), 970-976.

92. Tai, K. L.; Huang, G. M.; Huang, C. W.; Tsai, T. C.; Lee, S. K.; Lin, T. Y.; Lo, Y. C.; Wu, W. W., Observing phase transformation in CVD-grown MoS₂ via atomic resolution TEM. *Chem. Commun.* **2018**, 54 (71), 9941-9944.
93. Geim, A. K.; Grigorieva, I. V., Van der Waals heterostructures. *Nature* **2013**, 499 (7459), 419-425.
94. Novoselov, K.; Mishchenko, o. A.; Carvalho, o. A.; Neto, A. C., 2D materials and van der Waals heterostructures. *Science* **2016**, 353 (6298).
95. Ribeiro-Palau, R.; Zhang, C.; Watanabe, K.; Taniguchi, T.; Hone, J.; Dean, C. R., Twistable electronics with dynamically rotatable heterostructures. *Science* **2018**, 361 (6403), 690-693.
96. Bao, W.; Jing, L.; Velasco, J.; Lee, Y.; Liu, G.; Tran, D.; Standley, B.; Aykol, M.; Cronin, S.; Smirnov, D., Stacking-dependent band gap and quantum transport in trilayer graphene. *Nature Physics* **2011**, 7 (12), 948-952.
97. Lui, C. H.; Li, Z.; Mak, K. F.; Cappelluti, E.; Heinz, T. F., Observation of an electrically tunable band gap in trilayer graphene. *Nature Physics* **2011**, 7 (12), 944-947.
98. Jiang, T.; Liu, H.; Huang, D.; Zhang, S.; Li, Y.; Gong, X.; Shen, Y.-R.; Liu, W.-T.; Wu, S., Valley and band structure engineering of folded MoS₂ bilayers. *Nat. Nanotechnol.* **2014**, 9 (10), 825-829.
99. Shan, Y.; Li, Y.; Huang, D.; Tong, Q.; Yao, W.; Liu, W.-T.; Wu, S., Stacking symmetry governed second harmonic generation in graphene trilayers. *Sci. Adv.* **2018**, 4 (6), eaat0074.
100. Chen, J.; Zhu, E.; Liu, J.; Zhang, S.; Lin, Z.; Duan, X.; Heinz, H.; Huang, Y.; De Yoreo, J. J., Building two-dimensional materials one row at a time: Avoiding the nucleation barrier. *Science* **2018**, 362 (6419), 1135-1139.
101. McGuire, M. A.; Dixit, H.; Cooper, V. R.; Sales, B. C., Coupling of Crystal Structure and Magnetism in the Layered, Ferromagnetic Insulator CrI₃. *Chem. Mater.* **2015**, 27 (2), 612-620.
102. Fei, L.; Lei, S.; Zhang, W. B.; Lu, W.; Lin, Z.; Lam, C. H.; Chai, Y.; Wang, Y., Direct TEM observations of growth mechanisms of two-dimensional MoS₂ flakes. *Nat. Commun.* **2016**, 7, 12206.
103. Apte, A.; Kochat, V.; Rajak, P.; Krishnamoorthy, A.; Manimunda, P.; Hachtel, J. A.; Idrobo, J. C.; Syed Amanulla, S. A.; Vashishta, P.; Nakano, A.; Kalia, R. K.; Tiwary, C. S.; Ajayan, P. M., Structural phase transformation in strained monolayer MoWSe₂ Alloy. *ACS Nano* **2018**, 12 (4), 3468-3476.
104. Cho, S.; Kim, S.; Kim, J. H.; Zhao, J.; Seok, J.; Keum, D. H.; Baik, J.; Choe, D. H.; Chang, K. J.; Suenaga, K.; Kim, S. W.; Lee, Y. H.; Yang, H., Phase patterning for ohmic homojunction contact in MoTe₂. *Science* **2015**, 349 (6248), 625-628.
105. Gao, P.; Wang, L.; Zhang, Y.; Huang, Y.; Liu, K., Atomic-scale probing of the dynamics of sodium transport and intercalation-induced phase transformations in MoS₂. *ACS Nano* **2015**, 9 (11), 11296-11301.
106. Lin, Y. C.; Dumcenco, D. O.; Huang, Y. S.; Suenaga, K., Atomic mechanism of the semiconducting-to-metallic phase transition in single-layered MoS₂. *Nat. Nanotechnol.* **2014**, 9 (5), 391-6.
107. Ryu, G. H.; Chen, J.; Wen, Y.; Warner, J. H., In-Situ Atomic-Scale Dynamics of Thermally Driven Phase Transition of 2D Few-Layered 1T PtSe₂ into Ultrathin 2D Nonlayered PtSe Crystals. *Chem. Mater.* **2019**, 31 (23), 9895-9903.
108. Li, T.; Jiang, S.; Sivadas, N.; Wang, Z.; Xu, Y.; Weber, D.; Goldberger, J. E.; Watanabe, K.; Taniguchi, T.; Fennie, C. J.; Fai Mak, K.; Shan, J., Pressure-controlled interlayer magnetism in atomically thin CrI₃. *Nat. Mater.* **2019**, 18 (12), 1303-1308.

109. Cui, Y.; Zhou, Z.; Li, T.; Wang, K.; Li, J.; Wei, Z., Versatile Crystal Structures and (Opto) electronic Applications of the 2D Metal Mono-, Di-, and Tri-Chalcogenide Nanosheets. *Advanced Functional Materials* **2019**, *29* (24), 1900040.
110. Templeton, D.; Carter, G. F., The crystal structures of yttrium trichloride and similar compounds. *J. Phys. Chem.* **1954**, *58* (11), 940-944.
111. Birdja, Y. Y.; Pérez-Gallent, E.; Figueiredo, M. C.; Göttle, A. J.; Calle-Vallejo, F.; Koper, M. T., Advances and challenges in understanding the electrocatalytic conversion of carbon dioxide to fuels. *Nature Energy* **2019**, *4* (9), 732-745.
112. Choi, C.; Kwon, S.; Cheng, T.; Xu, M.; Tieu, P.; Lee, C.; Cai, J.; Lee, H. M.; Pan, X.; Duan, X., Highly active and stable stepped Cu surface for enhanced electrochemical CO₂ reduction to C₂H₄. *Nature Catalysis* **2020**, *3* (10), 804-812.
113. Kim, T.; Palmore, G. T. R., A scalable method for preparing Cu electrocatalysts that convert CO₂ into C₂₊ products. *Nat. Commun.* **2020**, *11* (1), 1-11.
114. Gattrell, M.; Gupta, N.; Co, A., A review of the aqueous electrochemical reduction of CO₂ to hydrocarbons at copper. *J. Electrochem. Soc.* **2006**, *594* (1), 1-19.
115. Li, P.-Z.; Wang, X.-J.; Liu, J.; Lim, J. S.; Zou, R.; Zhao, Y., A triazole-containing metal-organic framework as a highly effective and substrate size-dependent catalyst for CO₂ conversion. *J. Am. Chem. Soc.* **2016**, *138* (7), 2142-2145.
116. Stephens, I. E.; Bondarenko, A. S.; Grønbjerg, U.; Rossmeisl, J.; Chorkendorff, I., Understanding the electrocatalysis of oxygen reduction on platinum and its alloys. *Energy & Environmental Science* **2012**, *5* (5), 6744-6762.
117. Grosse, P.; Gao, D.; Scholten, F.; Sinev, I.; Mistry, H.; Roldan Cuenya, B., Dynamic changes in the structure, chemical state and catalytic selectivity of Cu nanocubes during CO₂ electroreduction: size and support effects. *Angewandte Chemie* **2018**, *57* (21), 6192-6197.
118. Li, Y.; Zhang, L. A.; Qin, Y.; Chu, F.; Kong, Y.; Tao, Y.; Li, Y.; Bu, Y.; Ding, D.; Liu, M., Crystallinity dependence of ruthenium nanocatalyst toward hydrogen evolution reaction. *ACS Catalysis* **2018**, *8* (7), 5714-5720.
119. De Luna, P.; Quintero-Bermudez, R.; Dinh, C.-T.; Ross, M. B.; Bushuyev, O. S.; Todorović, P.; Regier, T.; Kelley, S. O.; Yang, P.; Sargent, E. H., Catalyst electro-redeposition controls morphology and oxidation state for selective carbon dioxide reduction. *Nature Catalysis* **2018**, *1* (2), 103-110.
120. Che, Q.; Bai, N.; Li, Q.; Chen, X.; Tan, Y.; Xu, X., One-step electrodeposition of a hierarchically structured S-doped NiCo film as a highly-efficient electrocatalyst for the hydrogen evolution reaction. *Nanoscale* **2018**, *10* (32), 15238-15248.
121. Lu, X.; Zhao, C., Electrodeposition of hierarchically structured three-dimensional nickel-iron electrodes for efficient oxygen evolution at high current densities. *Nat. Commun.* **2015**, *6* (1), 1-7.
122. Day, T. M.; Unwin, P. R.; Macpherson, J. V., Factors controlling the electrodeposition of metal nanoparticles on pristine single walled carbon nanotubes. *Nano Lett.* **2007**, *7* (1), 51-57.
123. Pei, A.; Zheng, G.; Shi, F.; Li, Y.; Cui, Y., Nanoscale nucleation and growth of electrodeposited lithium metal. *Nano Lett.* **2017**, *17* (2), 1132-1139.
124. Kumar, S.; Pande, S.; Verma, P., Factor effecting electro-deposition process. *International Journal of Current Engineering and Technology* **2015**, *5* (2), 700-703.
125. Qiao, X.; Li, H.; Zhao, W.; Li, D., Effects of deposition temperature on electrodeposition of zinc-nickel alloy coatings. *Electrochimica Acta* **2013**, *89*, 771-777.
126. Yan, K.; Wang, J.; Zhao, S.; Zhou, D.; Sun, B.; Cui, Y.; Wang, G., Temperature-Dependent Nucleation and Growth of Dendrite-Free Lithium Metal Anodes. *Angewandte Chemie* **2019**, *131* (33), 11486-11490.
127. Ding, M. S.; Xu, K.; Zhang, S.; Jow, T. R., Liquid/solid phase diagrams of binary carbonates for lithium batteries part II. *J. Electrochem. Soc.* **2001**, *148* (4), A299.

128. Canetta, C.; Guo, S.; Narayanaswamy, A., Measuring thermal conductivity of polystyrene nanowires using the dual-cantilever technique. *Review of Scientific Instruments* **2014**, *85* (10), 104901.
129. Jin, M.; He, G.; Zhang, H.; Zeng, J.; Xie, Z.; Xia, Y., Shape-controlled synthesis of copper nanocrystals in an aqueous solution with glucose as a reducing agent and hexadecylamine as a capping agent. *Angewandte Chemie* **2011**, *50* (45), 10560-10564.
130. Lin, T.-Y.; Lee, S.-K.; Huang, G.-M.; Huang, C.-W.; Tai, K.-L.; Huang, C.-Y.; Lo, Y.-C.; Wu, W.-W., Electron beam irradiation-induced deoxidation and atomic flattening on the copper surface. *ACS applied materials & interfaces* **2019**, *11* (43), 40909-40915.
131. Ely, D. R.; García, R. E., Heterogeneous nucleation and growth of lithium electrodeposits on negative electrodes. *J. Electrochem. Soc.* **2013**, *160* (4), A662.
132. Sano, H.; Sakaebe, H.; Senoh, H.; Matsumoto, H., Effect of current density on morphology of lithium electrodeposited in ionic liquid-based electrolytes. *J. Electrochem. Soc.* **2014**, *161* (9), A1236.
133. Paunovic, M.; Schlesinger, M., *Fundamentals of electrochemical deposition*. John Wiley & Sons: 2006.
134. Saidin, N. U.; Ying, K. K.; Khuan, N. I., *Electrodeposition: principles, applications and methods*. **2011**.
135. Roy, Y.; Warsinger, D. M., Effect of temperature on ion transport in nanofiltration membranes: Diffusion, convection and electromigration. *Desalination* **2017**, *420*, 241-257.
136. Antczak, G.; Ehrlich, G., Jump processes in surface diffusion. *Sur. Sci. Rep.* **2007**, *62* (2), 39-61.
137. Song, Z.; Xie, Z. H., A literature review of in situ transmission electron microscopy technique in corrosion studies. *Micron* **2018**, *112*, 69-83.
138. Uhlig, H. H.; Revie, R. W., *Corrosion and corrosion control*. **1985**.
139. Stephens, I. E. L.; Rossmeisl, J.; Chorkendorff, I., Toward sustainable fuel cells. *Science* **2016**, *354* (6318), 1378-1379.
140. Liu, Y.; Liang, X.; Gu, L.; Zhang, Y.; Li, G.-D.; Zou, X.; Chen, J.-S., Corrosion engineering towards efficient oxygen evolution electrodes with stable catalytic activity for over 6000 hours. *Nat. Commun.* **2018**, *9* (1), 1-10.
141. Wu, J.; Yang, H., Platinum-based oxygen reduction electrocatalysts. *Acc. Chem. Res.* **2013**, *46* (8), 1848-1857.
142. Ndiaye, A.; Charki, A.; Kobi, A.; Kébé, C. M.; Ndiaye, P. A.; Sambou, V., Degradations of silicon photovoltaic modules: A literature review. *Sol. Energy* **2013**, *96*, 140-151.
143. Lin, D.; Liu, Y.; Li, Y.; Li, Y.; Pei, A.; Xie, J.; Huang, W.; Cui, Y., Fast galvanic lithium corrosion involving a Kirkendall-type mechanism. *Nat. Chem.* **2019**, *11* (4), 382-389.
144. Geisler, T.; Dohmen, L.; Lenting, C.; Fritzsche, M. B. K., Real-time in situ observations of reaction and transport phenomena during silicate glass corrosion by fluid-cell Raman spectroscopy. *Nat. Mater.* **2019**.
145. Badwe, N.; Chen, X.; Schreiber, D. K.; Olszta, M. J.; Overman, N. R.; Karasz, E.; Tse, A.; Bruemmer, S. M.; Sieradzki, K., Decoupling the role of stress and corrosion in the intergranular cracking of noble-metal alloys. *Nat. Mater.* **2018**, *17* (10), 887-893.
146. Scully, J. R.; Harris, W. L., Opportunities and challenges in corrosion education: review of a national research council assessment. *The Electrochemical Society Interface* **2012**, *21* (1), 67.
147. Li, X.; Zhang, D.; Liu, Z.; Li, Z.; Du, C.; Dong, C., Materials science: Share corrosion data. *Nature* **2015**, *527* (7579), 441-442.
148. Frankel, G., Pitting corrosion of metals: a review of the critical factors. *J. Electrochem. Soc.* **1998**, *145* (6), 2186.
149. Frankel, G.; Sridhar, N., Understanding localized corrosion. *Mater Today* **2008**, *11* (10), 38-44.

150. Ralston, K.; Birbilis, N., Effect of grain size on corrosion: a review. *Corrosion* **2010**, *66* (7), 075005-075005-13.
151. Renner, F.; Stierle, A.; Dosch, H.; Kolb, D.; Lee, T.-L.; Zegenhagen, J., Initial corrosion observed on the atomic scale. *Nature* **2006**, *439* (7077), 707-710.
152. Stansbury, E. E.; Buchanan, R. A., *Fundamentals of electrochemical corrosion*. ASM international: 2000.
153. Chee, S. W.; Pratt, S. H.; Hattar, K.; Duquette, D.; Ross, F. M.; Hull, R., Studying localized corrosion using liquid cell transmission electron microscopy. *Chem. Commun.* **2015**, *51* (1), 168-171.
154. Chee, S. W.; Burke, M. G., 12 Applications of Liquid Cell TEM in Corrosion Science. *Liquid Cell Electron Microscopy* **2017**, 258.
155. Hattar, K.; Unocic, R. R., Applications of Liquid Cell-TEM in Corrosion Research. *Recent Developments in Analytical Techniques for Corrosion Research* **2022**, 121-150.
156. Chee, S. W.; Duquette, D. J.; Ross, F. M.; Hull, R., Metastable structures in Al thin films before the onset of corrosion pitting as observed using liquid cell transmission electron microscopy. *Microsc. Microanal.* **2014**, *20* (2), 462-468.
157. Chen, L.; Leonardi, A.; Chen, J.; Cao, M.; Li, N.; Su, D.; Zhang, Q.; Engel, M.; Ye, X., Imaging the kinetics of anisotropic dissolution of bimetallic core-shell nanocubes using graphene liquid cells. *Nat. Commun.* **2020**, *11* (1), 1-10.
158. Shi, F.; Peng, J.; Li, F.; Qian, N.; Shan, H.; Tao, P.; Song, C.; Shang, W.; Deng, T.; Zhang, H., Design of Highly Durable Core-Shell Catalysts by Controlling Shell Distribution Guided by In-Situ Corrosion Study. *Adv. Mater.* **2021**, *33* (38), 2101511.
159. Park, J. H.; Chee, S. W.; Kodambaka, S.; Ross, F. M., In situ LC-TEM studies of corrosion of metal thin films in aqueous solutions. *Microsc. Microanal.* **2015**, *21* (S3), 1791-1792.
160. Suganuma, K., Advances in lead-free electronics soldering. *Current Opinion in Solid State and Materials Science* **2001**, *5* (1), 55-64.
161. Hill, M.; Smith, F., Calculation of initial and primary yields in the radiolysis of water. *Radiat. Phys. Chem.* **1994**, *43* (3), 265-280.
162. Jeitschko, W.; Jaberg, B., Structure refinement of Ni₃Sn₄. *Acta Crystallographica Section B: Structural Crystallography and Crystal Chemistry* **1982**, *38* (2), 598-600.